Universitat Autònoma de Barcelona

GAMMA EMISSION FROM TYPE IA SUPERNOVAE: SIMULATION, ANALYSIS AND DETECTION

Mariona Caixach

Doctoral Thesis

GAMMA EMISSION FROM TYPE IA SUPERNOVAE: SIMULATION, ANALYSIS AND DETECTION

Author:

Mariona Caixach

Supervisor:
Dr. Jordi Isern

Tutor:
Dr. Jordi Mompart

A thesis submitted for the degree of
Doctor of Philosophy in Physics

in the

UNIVERSITAT AUTÒNOMA DE BARCELONA (UAB)
Departament de Física
Programa de Doctorat en Física

April, 2022

"*Science does not aim at establishing immutable truths and eternal dogmas; its aim is to approach the truth by successive approximations, without claiming that at any stage final and complete accuracy has been achieved.*"

—Bertrand Russell

Abstract

Supernovae (SNe) are powerful stellar explosions that highlight the end of the life of some stars. Type Ia supernovae (SNe Ia) are a type of SNe originated by thermonuclear runaway in a white dwarf. This thesis is devoted to the study of SNe Ia and their gamma-ray emission with the goal to study how to improve the knowledge about this phenomenon.

In the first chapter, we make an overview of SNe, focusing in SNe Ia. We explain what we currently know about these type of SNe and which are the hypothesis that try to explain their explosion mechanism and progenitor system. We explain that gamma-rays from SNe Ia can work as diagnostic tools.

The second chapter describes the creation of a code that simulate the transport of gamma photons during the expansion phase of SN Ia in a 3D Cartesian grid. The code is based in Monte Carlo's techniques and the theory of indivisible energy packets. The goal of the code is to simulate the synthetic observables of theoretical scenarios of SNe Ia.

In the third chapter, we simulate multiple scenarios of SNe Ia with different composition and asymmetries to analyse their synthetic observables. The experiments focus on placing ^{56}Ni on different locations of the ejecta and creating asymmetries. The results show how a favourable line of sight allows to distinguish their signatures at early days until day $\sim$35. The experiments with ^{56}Ni close to the surface display emission lines at $\sim$15 days after the explosion. Moreover, the 0.158 MeV line allows us to determine if ^{56}Ni was in the surface of the model. The light curves of models with ^{56}Ni close to the surface have a rapid rise of their flux. In particular, the test with an outer plume of ^{56}Ni displays a peak around the $\sim$9th day, which agrees with the mean lifetime decay of ^{56}Ni. The tests with ^{48}Cr display lines from its daughter nucleus, ^{48}V, at day $\sim$15. Especially, 0.983 MeV and 1.312 MeV lines. The light curves of the models with ^{48}Cr display a faster rise and a faster decline than the ones without.

Finally, in the last chapter we describe a detailed analysis that studies the sensitivity of the anticoincidence system (ACS) of the spectrometer SPI on board of the INTEGRAL space observatory for detecting the early gamma-ray emission of a galactic SN Ia as a function of the explosion model, distance and pointing direction. The results suggest that the detection is possible at about 6 - 12 days after the explosion and, at the same time, we can discard missing any hidden explosion during the lifetime of the mission.

Acknowledgements

Abans de començar, cal que reservi unes paraules a totes aquelles persones que han fet possible aquesta tesis. De manera directa o indirecta, aquest treball no hauria sigut possible si no m'haguéssiu acompanyat en aquest viatge.

Aquesta tesis no hauria estat possible sense la visió i anys d'experiència del meu director Jordi Isern. Gràcies Jordi per la oportunitat d'aquests anys de recerca a l'Institut de Ciències de l'Espai, per a aquest guiatge, per obrir-me al món de la astrofísica i sobretot de les supernoves.

Als membres del grup durant la meva tesis, gràcies. A la Margarita pel suport i ensenyament que m'ha proporcionat i, no menys important, per les seves ajudes burocràtiques. A Aldo y a Nancy muchas gracias por vuestro apoyo. Vull mencionar a en Josep Guerrero, que la seva paciència i experiència informàtica m'ha ajudat quan em barallava amb el clúster de l'ICE. Molts resultats que ensenyem en aquest treball han sigut possibles gràcies a això. També he d'agrair a l'Eduardo Bravo la seva gran ajuda a la hora de resoldre dubtes i animar-me a seguir.

Special thanks to Pierre Jean. His mentorship during my stay in IRAP in Toulouse allowed to broad my career background. I learnt a lot under his mentorship and it made my stay in a new environment very welcoming. Even when the pandemic hit, he made sure I was fine and everything was moving forward.

A tots els estudiants de doctorat de l'ICE, als qui he vist acabar i els que he vist entrar, gràcies per la vostra companyia i alegria que aporteu cada dia a la feina. Gràcies a la Laura, la Núria i a la Antonia, que em van rebre amb els braços oberts al grup de recerca i que em van ajudar adaptar-me a l'ambient. Sobretot gràcies a l'Anna, l'Andrea, al David, a la Marina i a la Safoura. Hi heu sigut sempre per animar-me als dies més frustrants.

Tot i que potser les paraules d'aquesta tesis us queden més llunyanes, a les meves amigues de tota la vida, que per sort en cara en sou moltes per poder-vos llistar a totes, gràcies. En sigueu conscients o no, heu ajudat en aquesta tesis. També a tu Eloi, que m'has acompanyat, anima't, dóna't força i molta motivació. Gràcies a la Taiga i a la Ona pel seu escalf felí. Finalment, vull agrair a la meva família tot el que han fet per mi. Per donar-me la oportunitat de realitzar el meu objectiu d'aprendre Física i fer recerca. Per la seva confiança incondicional en les meves capacitats. Gràcies Ariadna per tot el teu suport i ajuda. A la meva mare Emília, gràcies per alegrar-te casi més que jo de que hagi assolit aquesta etapa. I al meu pare Josep, el quals estic molt contenta que sigui present en aquesta etapa tan important per mi, moltíssimes gràcies per ensenyar-me des de ben petita que l'univers és ple de misteris per aprendre i que l'esforç que hem de fer per coneixe'ls val la pena.

Contents

List of Figures

List of Tables

Introduction

Type Ia supernovae (SNe Ia) are the results of the thermonuclear explosion of a C/O white dwarf (WD) that accretes mass from a companion in a close binary system (Hoyle and Fowler, 1960). These types of supernova (SN) are identified by the lack of H lines and for having strong Si lines in the early spectra (Filippenko, 1997). They are of great importance in astronomy and cosmology. They mark an ending step in the stellar evolution. Their explosion enrich the element composition of galaxies and impact the new generation of stars. Their optical brightness and homogeneity in their light curve makes them ideal candidates to perform as standard candles. Their use as distance indicators has influenced in the discovery of the acceleration of the expansion of the universe. These past years, the number of discoveries of this type of supernova has increased and in consequence it has been found that there are many SN Ia subtypes. This challenges the initial view of the homogeneous nature of SNe Ia. The existence of these many subtypes suggests that SNe Ia may have more than one kind of progenitor scenarios and explosion mechanisms.

The light curve and spectra of these events provide information about the progenitor scenario and explosion mechanism. They are powered by the decay chain ^{56}Ni $\rightarrow^{56}$Co $\rightarrow^{56}$Fe (Colgate and McKee, 1969). The detection of gamma-ray lines from this decay can give clues about the kinematics and morphology of the explosion. Most observables from SNe Ia come from the optical and infrared energy range, observations made in gamma-ray range are scarce. However, the gamma-ray energy range provides a precise and direct interpretation of the event due to the simplicity of its physical processes (Burrows and The, 1990; Gomez-Gomar et al., 1998; Milne et al., 2004; Sim and Mazzali, 2008; Isern et al., 2008). In this work we aim to explore the importance of gamma emission as diagnostic tool. In an effort to study these events despite the lack of observations, theoretical simulations of the explosion aim to forecast SNe Ia observables. For this end, we build a 3-dimensional gamma-ray radiative transfer code with the goal to show the importance of gamma emission as diagnostic tool. The 3D approach allows to simulate geometries with asymmetries in the models, and we aim to study the dependence of the synthetic observables on the angle of view. We focus on the gamma emission of early stages of the explosion, as this has proved to carry valuable information about the explosion mechanism.

Given the importance of an early detection of gamma-ray emission of a SN Ia, we have extended our study into finding a way to be able to detect these events more easily. Observation of the very early gamma-ray spectra of a SN Ia has not yet been possible due to the low luminosity expected during that period and the large distances to that kind of supernova. If the detection of SNe Ia

is dependant of its observations in the optical band, we may have missed the first days of the explosion, as SNe Ia light curve peaks around day 20 after the explosion. In this scope, a SN Ia explosion occurring in our Galaxy is an ideal scenario to allow a significant measurement of its gamma-ray spectrum few days after the explosion. However, it has to be detected as soon as possible in order to quickly trigger its observation by gamma-ray spectrometers. If we rely on optical detection in a Galactic SN, that could lead to missing the early stages of the explosion because the optical flux could be attenuated by interstellar extinction. But, a quick detection can be achieved in gamma-ray because they are transparent to the Galactic plane. This is why we have made an study of the sensitivity to detect the very early gamma-ray emission of a galactic SN Ia with the anticoincidence system (ACS) of SPI on board of the INTEGRAL space observatory.

In terms of structure, the thesis has been organized as follows. In Chapter 1 we make an overview of supernovae, type Ia supernovae and the gamma emission from them. We proceed to explain how we built a 3D gamma transfer code in Chapter 2. In this same chapter we run some tests in order to verify a correct operation of the code. In Chapter 3 we have applied the code to simulate different explosion scenarios of SN Ia. We have focused in models that have ^{56}Ni placed in different locations. We have also introduced ^{48}Cr as a radioactive material in order to explore the synthetic observables this isotope makes. Chapter 4 shows our study of the sensitivity of ACS/SPI to detect a galactic supernova.

Chapter 1

Type Ia supernovae and their gamma-radiation

1.1 Supernovae

Supernovae (plural of supernova; abbreviated as SNe) are powerful stellar explosions whose luminosity can even outshine that of the galaxy in which they originate. These events are the outcome of the gravitational collapse of a massive star (Zwicky, 1938) or the thermonuclear runaway in white dwarfs (Hoyle and Fowler, 1960).

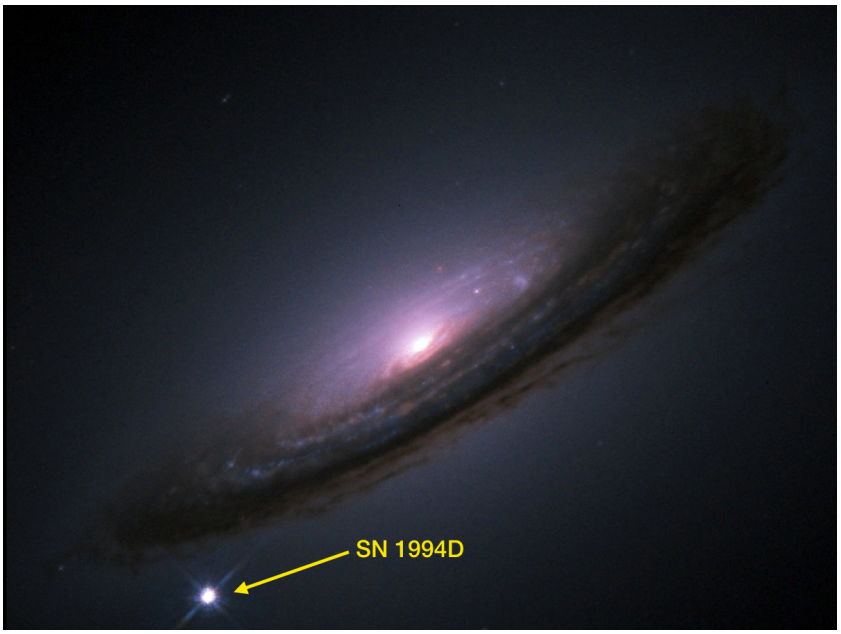

FIGURE 1.1: Hubble Space Telescope image of SN 1994D (bottom left) in galaxy NGC 4526.

The term 'supernova' was coined by Baade and Zwicky in 1934 as a way to distinguish these events from common novae (Baade and Zwicky, 1934). Historically, a new star appearing in the night sky was called a nova ('new' in Latin). When observational techniques improved, observers realized that some of those novae were different. These different novae were found in further nebulae, and

they were brighter than regular ones, hence the term 'super' in supernovae. Nowadays, we can make a clear distinction between them. Novae are stellar eruptions that increase the brightness of the star temporarily, ejecting stellar material during their eruptions. On the other hand, a supernova is a cataclysm at the end of the life of some stars. The explosion expels multiple solar masses at velocities close to the speed of light. The progenitor star of a supernova event will never go back to its previous state as it will turn into a black hole, a neutron star or leave no remains.

Supernovae are of great importance in astrophysics and cosmology. They are the main contributors to heavy elements in the universe (Arnett and Chevalier, 1996) since the explosion expels the many elements synthesised during the star life or the explosion. They also play a role in stellar evolution, influencing, for example, the creation of new generations of stars. Their remnants are thought to be the main accelerators of cosmic rays in the universe (Koyama et al., 1995). Moreover, they are used as cosmological distance indicators.

1.1.1 Classification of supernovae

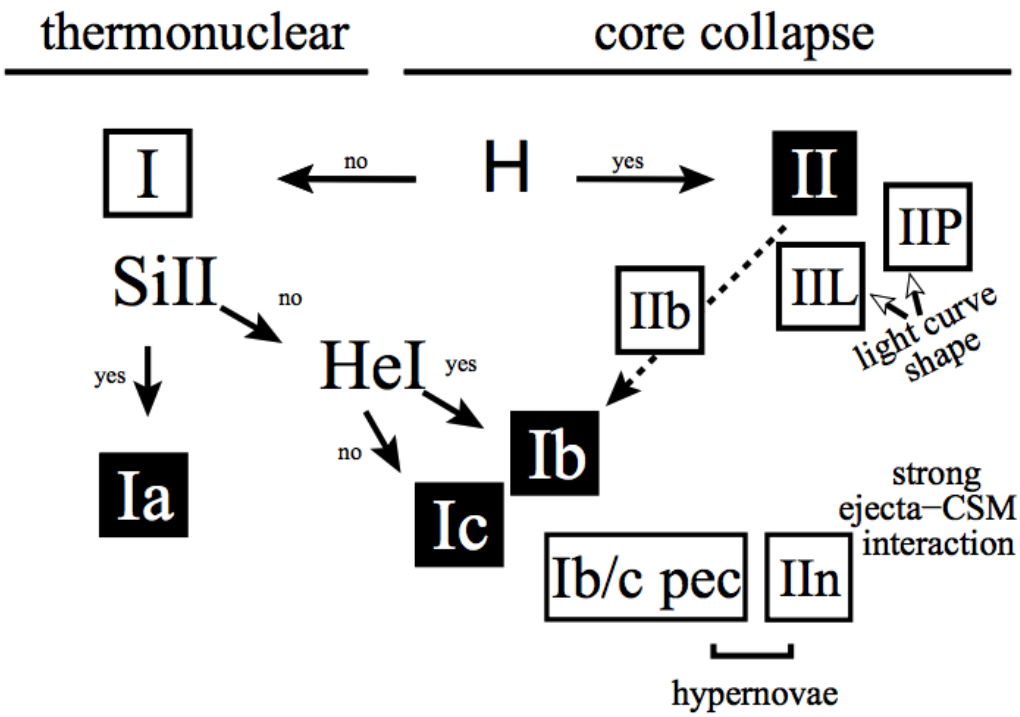

FIGURE 1.2: Supernovae classification. Source: Turatto (2003).

The taxonomy of SNe is made by their optical spectra at the maximum luminosity and, to some extent, their optical light curve. They were first classified in two main categories, Type I and Type II, by Minkowski (1941). The classification was made by the presence of hydrogen lines in the spectra. Type I do not display H lines in the spectra, but Type II do. When astronomers observed more supernovae, these main two types required to be divided into more

categories (see Filippenko, 1997). Type I SNe have three categories: type Ia, Ib and Ic. Type Ia have Si in the spectra meanwhile, type Ib and Ic do not. Between Ib and Ic, the first display He lines but the second has lack them. Type II have four sub-categories: IIb, IIn , II-L and II-P. The early spectra of type IIb display lines of H, still the late-time spectra are similar to type Ib/c. The spectra of type IIn display narrow lines of H due to the interaction between the ejecta and a dense circumstellar medium (Chugai and Danziger, 1994). Figure 1.3 shows a comparison of optical spectra of different SN types. Finally, both type II-L and type II-P show broad H lines. However, their optical light curves are different (see Barbon et al., 1979): type II-L shows a linear decline after the peak brightness, while type II-P shows a plateau. Figure 1.3 shows a comparison of optical spectra of different SN types, and a sample of the typical light curves is shown in Figure 1.4.

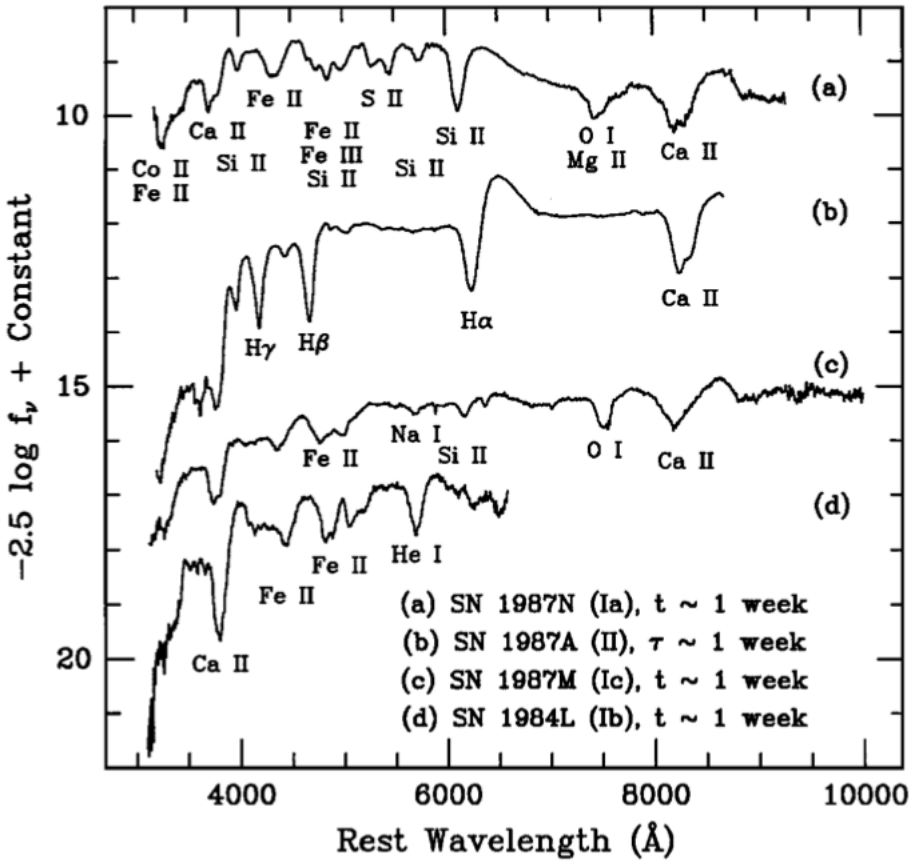

FIGURE 1.3: Spectra comparison of different SNe types. Source: Filippenko (1997).

Nevertheless, this taxonomy of SNe does not take into account the mechanism that triggers the explosion. Type Ia, for example, are the outcome of a white dwarf that suffers thermonuclear burning, as is explained in the following sections. As for all the other types of SNe, it is believed they are triggered by the core collapse of their progenitor star. Stars suffer gravitational compression when they no longer generate fusion reactions at the end of their lives. This will trigger an explosion of massive stars ($M_{star} > 8\ M_\odot$). Consequently, the star

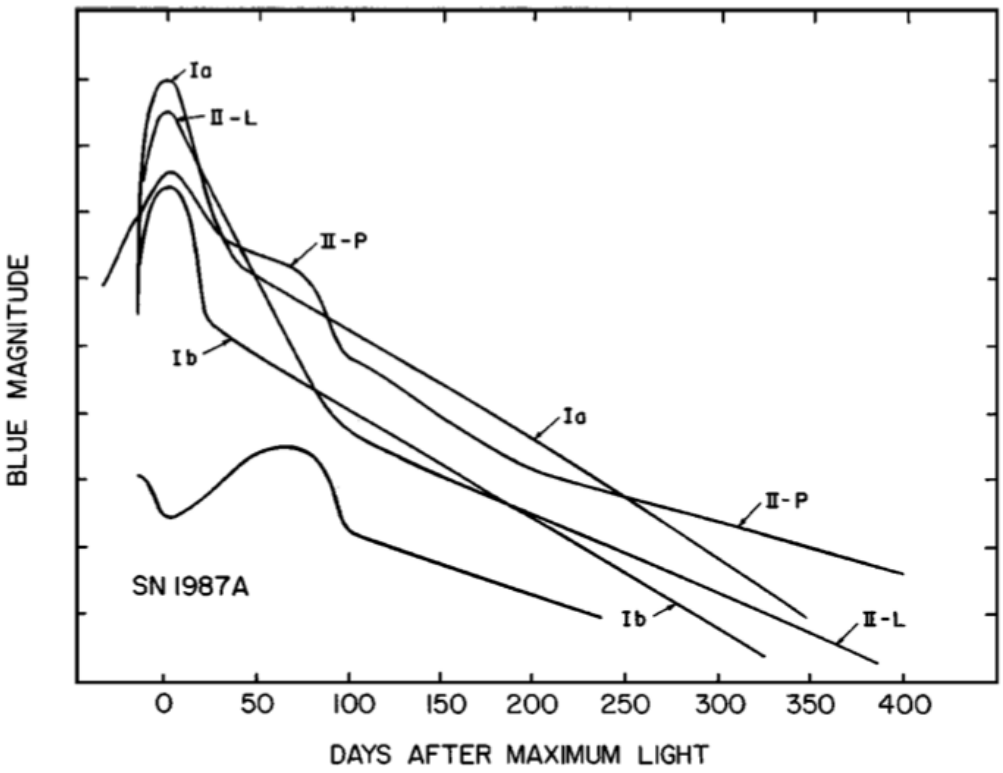

FIGURE 1.4: Light curve comparison of different SNe types. Source: Filippenko (1997).

expels several solar masses of material and compresses the core into a neutron star or black hole.

1.2 Type Ia Supernovae

Supernovae Ia (SNe Ia) have optical spectra that show no signs of H or He. At early times (∼1 week after maximum optical light), they display lines of intermediate-mass elements such as Si, Ca, C, O, Mg or S. At early stages there is a small contribution of iron-peak elements such as Fe and Co. When the photosphere recedes, the contribution of iron-peak elements increases (see Filippenko, 1997). The lines of intermediate-mass elements appear kinematically broadened around the peak of maximum light by velocities of $\sim 10^3$ - 10^4 km s^{-1}. SNe Ia reach large optical luminosities ($\sim 10^{43}$ erg s^{-1}) around their maximum light (Maoz et al., 2014). Their optical luminosities are powered by the decay chain $^{56}Ni \rightarrow {}^{56}Co \rightarrow {}^{56}Fe$. This decay fuels the explosion by releasing high energy gamma-ray photons that heat the debris and power the optical and infrared light curves of the event (see Colgate and McKee, 1969).

Their peak luminosity is proportional to the mass of ^{56}Ni ejected (Arnett, 1982). Moreover, they were proposed as distance indicators due to the homogeneity of their light curves. However, they started to present some variations in their luminosity peak when more observations were made. Phillips (1993) drew a

relation between their peak luminosity and light curve width. This relation allowed to account for their luminosity variability and be used as standard candles. Their use as standard candles played a major role in the discovery of the acceleration of the cosmic expansion.

The progenitor stars of type Ia have never directly been observed, thought they are believed to be the result of the thermonuclear runaway in white dwarfs (WDs). Hoyle and Fowler (1960) showed that the thermonuclear burning in an electron degenerate stellar core can lead to an explosion that shatters the star. Observations suggest that SNe Ia are found in old and young galaxies. Thus, massive stars are not fitted to be progenitors, as they are short-lived and occur in young galaxies. This suggest low mass stars ($M_{star} < 8\ M_{\odot}$) are most likely the progenitors of type Ia SNe. These stars will end their life as WDs, which previously would have expelled the H and He layers in the giant phase of the star evolution.

The rapid evolution of SNe Ia light curves is also an indicator of a compact object as their progenitor. The thermonuclear burning of a C/O core synthesises intermediate-mass elements and tenths of ^{56}Ni that are ejected in the explosion. There is a good agreement between the spectra created by such progenitor model and the spectra of observed SNe Ia. See the examples of SN 2011fe (Nugent et al., 2011; Bloom et al., 2012) and SN 2014J (Churazov et al., 2014; Diehl et al., 2014; Isern et al., 2014; Churazov et al., 2015; Isern et al., 2016).

An isolated WD is a stable environment if it does not exceed the Chandrasekhar limit of $\sim 1.36\ M_{\odot}$ (for a non-rotating C/O WD). The only way a thermonuclear runaway can be triggered in a stable WD is by interacting with another star in a binary system. Several binary scenarios have been theorized as progenitor systems of SNe Ia (see Section 1.2.1). However, it is still under debate which one is behind this type of explosions. Moreover, the progenitor question has an added uncertainty. We also need to determine the onset mechanism of the thermonuclear burning. Different mechanisms of burning impact the synthesis of intermediate-mass elements and iron-peak elements in the first seconds of the explosion.

The greater interest in SNe Ia these past years has given rise to many of their detections. They have large optical luminosities at maximum light compared to other supernova types (see Figure 1.4). There is an interest to use them as distance indicators. Because of both reasons, they are the most discovered supernova type. We could expect that, in consequence, the enigma of their progenitor scenario would have been narrowed down. On the contrary, the increment of SNe Ia has turned out in the discovery of a considerable amount of peculiar types (Taubenberger, 2017) that differ from the 'normal' SNe Ia type (Branch et al., 1993; Branch, 1998).

1.2.1 Progenitor scenario

The progenitor of SNe Ia is believed to be a C/O white dwarf (WD) that suffers a thermonuclear explosion. The thermonuclear runaway is due to mass accretion from a companion in a close binary system (Hoyle and Fowler, 1960). The WD needs to be in a binary system in which the interaction with its companion triggers the inert state of the WD. However, the nature of its companion is still under debate. In this section we explain the basic binary configurations that can lead to thermonuclear runaway of the WD.

First, a remark regarding the WD itself. There can be different kind of WD compositions: pure He WDs, C/O WDs and O/Ne WDs. Observations support the C/O as progenitors of SN Ia. The other two kind are also a compact objects that happen in old and young environments and provide rapid light curves. However, He are discarded as possible progenitors. They synthesises just iron-group elements when experience thermonuclear burning and this does not agree with SN Ia spectra (Woosley et al., 1986). On the other hand, O/Ne is expected to collapse to a neutron star when it increases its mass to the Chandrasekhar limit. However, if a thermonuclear ignition occurs at a particular density under favourable conditions (see Isern et al., 2021 for a detailed review) the WD can experience thermonuclear runaway. Some studies suggest that this scenario could contribute to a 3% up to a 10% of SNe Ia progenitors (Marquardt et al., 2015).

The possible progenitor scenarios are single degenerate (Whelan and Iben, 1973; Nomoto, 1982) or double degenerate (Iben and Tutukov, 1984; Webbink, 1984). The paths in which these two scenarios lead to a SN Ia are shown in Figure 1.5.

A single degenerate (SD) scenario is made of a WD and a main sequence star or red giant star. If the mass of the WD is close to the Chandrasekhar limit ($\sim$1.38 $M_\odot$) the accretion of mass from its companion can lead to a thermonuclear runaway. As the WD is increasing in mass, the temperature and density of the core rises. As for the WD's nature, it is not dependent on its temperature and the star does not expand. The rise of temperature ignites the carbon fusion and then leads to a runaway nuclear fusion that disrupts the star. The accretion of mass happens through Roche-lobe overflow from the non degenerate star to the C/O WD. This path is illustrated in Figure 1.5. First, the more massive star in the binary system loses its H envelope when it fills its Roche-lobe and mass transfer occurs in an unstable way. This results in a common envelope that shrinks the stars orbital separation. The more massive star will have evolved into a C/O WD and its companion still on the main sequence. When the companion reaches a stage in which fills its Roche-lobe, the WD will accrete mass from the companion. The WD will reach the Chandrasekhar limit and experience a thermonuclear runaway resulting in a SN Ia (Hillebrandt et al., 2013; Isern et al., 2021). The accretion rate needs to be in a specific range for the WD to become a SN Ia. Another case in the SD scenario is possible for a WD whose mass is way below the Chandrasekhar mass, a sub-Chandrasekhar WD. In this context, the explosion mechanism differs from the close to Chandrasekhar limit WD. These explosion mechanism are explained in section 1.2.2.

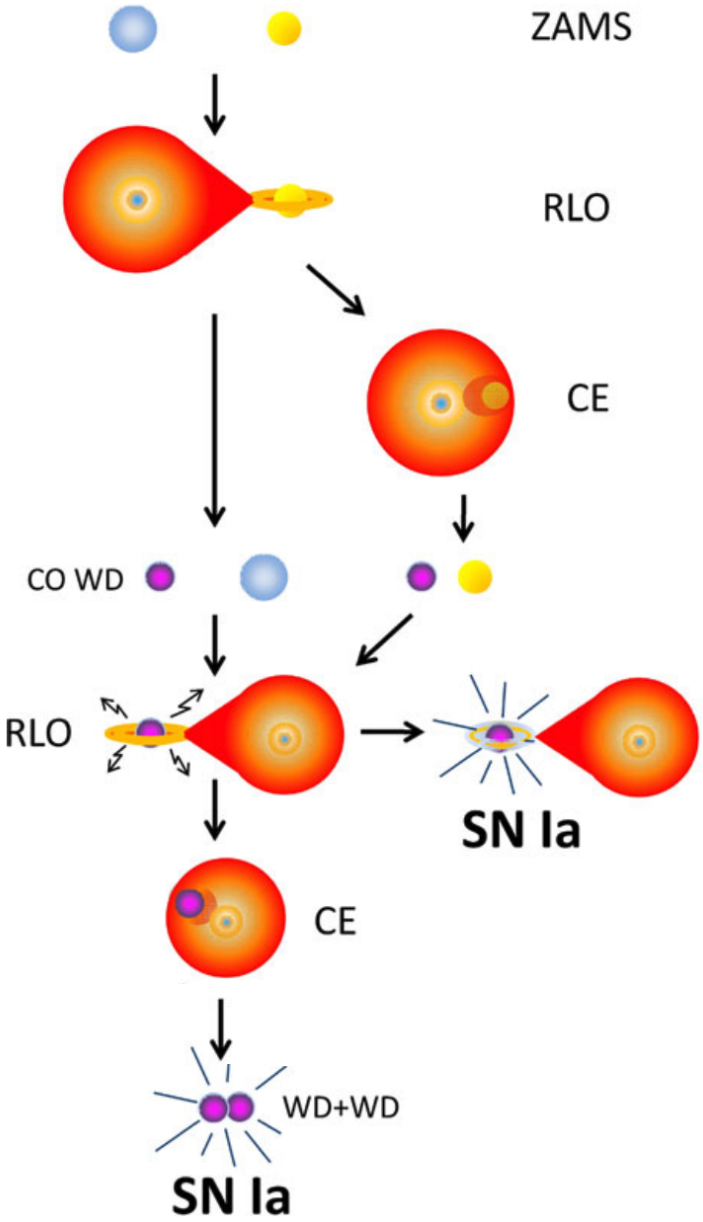

FIGURE 1.5: Multiple channel scenarios to SN Ia. Abbreviations: ZAMS – zero age main sequence, RLO – Roche-lobe overflow, CE – common envelope, CO WD – carbon-oxygen white dwarf, SN Ia – supernova Ia. Source: Edited from Ivanova et al. (2013)

A double degenerate (DD) scenario has two WD in its binary system. The path to reach the scenario is similar to the SD one but with a second common envelope. The common envelope is created when the second star fills the Roche-lobe and mass transfer occurs in an unstable way. This results later in two WDs that can merge in the Hubble time due to the orbital angular momentum loss via gravitational wave radiation. There is another possible DD scenario, but it does not derive from a binary system. It is a two WDs collision scenario. The collision of the two WDs ignites them and triggers the SN Ia. It is suggested

that these collision can happen in a highly dense environment, like a globular cluster or the center of a galaxy (see Raskin et al., 2009; Rosswog et al., 2009; Isern et al., 2021).

1.2.2 Explosion mechanism

Many theoretical models exist that try to explain the burning front of the thermonuclear runaway in the C/O WD. There were initially two main approaches to the thermonuclear burning. It could proceed as a shock-driven supersonic detonation or as a subsonic deflagration.

The pure detonation model was proposed by Arnett (1969). It proposes an ignition of the carbon in the center of the WD. The burning propagates supersonically and incinerates the entire WD. The rapid burning in the high density environment of a WD results in the synthesis of only iron-peak elements. The presence in the spectra of just iron-peak elements and lack of intermediate-mass elements does not agree with the observations and this model was excluded.

The ignition mechanism of the deflagration model is a flame mediated by heat conduction. The burning front propagates subsonically and the star has time to expand. This decreases the burning efficiency and reduces the synthesis of iron-peak elements. Some of these models fail to reproduce the brightness of 'normal' SN Ia (Röpke et al., 2006), but W7 model of Nomoto et al. (1984) has been successful in reproducing them.

In an attempt to combine the best of the two later models of thermonuclear burning, a delayed detonation model was proposed (Khokhlov, 1991). This model involves an initial phase of deflagration in which the flame propagates subsonically until it reaches a density of $\rho \sim 10^6$ - 10^7 g cm^{-3}. Then the burning flame turns into a detonation. This model has been successful in reproducing the parameters of normal SN Ia with a Chandrasekhar mass C/O WD as progenitor (Röpke and Niemeyer, 2007; Mazzali et al., 2007; Seitenzahl et al., 2013).

If the progenitor is a sub-Chandrasekhar WD then the latter models do not apply because the thermal runaway is not ignited by reaching the Chandrasekhar limit. In this scenario a double detonation model is proposed (Iben and Webbink, 1987; Fink et al., 2007). This model presumes that the sub-Chandrasekhar WD accretes He from its binary donor. When the right conditions are met the He accumulated in the outer layers of the WD can detonate and this triggers a second detonation in the inner WD (see Isern et al., 2021 for a detailed explanation).

1.2.3 Subtypes

These past years many SNe Ia have been discovered that differ from the definition of 'normal' SN Ia (Branch et al., 1993) and that do not follow the relation

of light curve vs. width (Phillips, 1993). These subtypes of SNe Ia may account for the ∼30% of the total of SNe Ia observed, as suggested by Li et al. (2011). This high percentage of peculiar SNe Ia could condition their use as cosmological distance indicators.

We summarize in this section the properties of these peculiar SNe. These subtypes can be divided by similarities in their spectra, brightness or light curve. In Figure 1.6 we show a plot from Taubenberger (2017). The plot displays areas of different SN Ia subtype families and which peculiar SNe Ia belong in them. The figure shows their blue magnitude at maximum and the decline of the blue light curve 15 days after maximum in comparison to the 'normal' SN Ia type (displayed as a black line).

The subtype family of SNe Iax has low luminosity for its light-curve shape (Foley et al., 2013). The mixing in the ejecta and its low expansion velocity suggest that they are triggered by deflagration, instead of delayed detonation often used in 'normal' types (Magee et al., 2016). The presence of He lines in some of their members suggests that they may be products of a double detonation scenario (Wang et al., 2013). Other sub-luminous subtypes are the ones classified as Ca-rich. These have low ejecta mass and high abundance of Ca in the ejecta at late times (Perets et al., 2010). These subtypes have similar properties to type Ib SNe. Yet, they are found in old environments. This suggests they are triggered by thermonuclear runaway instead of core collapse. The family of 91bg-like are fast decliners and sub-luminous (Taubenberger et al., 2008). Their spectra resembles the 'normal' type but with an earlier transition from intermediate-mass elements to Fe and Co lines. Another sub-luminous family but slow decliners are the 02es-like. These are similar to 91bg-like but they display higher amounts of ^{56}Ni. In the high luminous subtypes we find SNe Ia-CSM, 91T-like SNe and Super-Chandrasekhar. Some SNe Ia show evidence of interaction with a dense circumstellar material (CSM) during the first year post-explosion. These types named as SNe Ia-CSM are found in dense environments. This suggests that their progenitor system is a single degenerate scenario with an evolved secondary star (Hamuy et al., 2003). The Super-Chandrasekhar types have a total amount of ejecta higher than the Chandrasekhar mass limit. This may be explained by a WDs merger, a fast rotating WD, an off-center ignition or an explosion synthetises other radioactive nuclei than just ^{56}Ni. Finally, 91T-like SNe have high luminosities and broad light curve that can fit the Phillips relation. However, their spectra at optical pre-maximum display iron-peak elements. They have high amounts of ^{56}Ni (∼0.8 $M_\odot$) that may be produced in outer layers or placed there because of outward mixing. For a deep review on subtypes see Taubenberger (2017).

The existence of these peculiar SNe Ia challenges the common concept of SNe Ia being an homogeneous SNe type. It endorses the hypothesis that they are attained by different scenarios and explosion mechanism instead of just one.

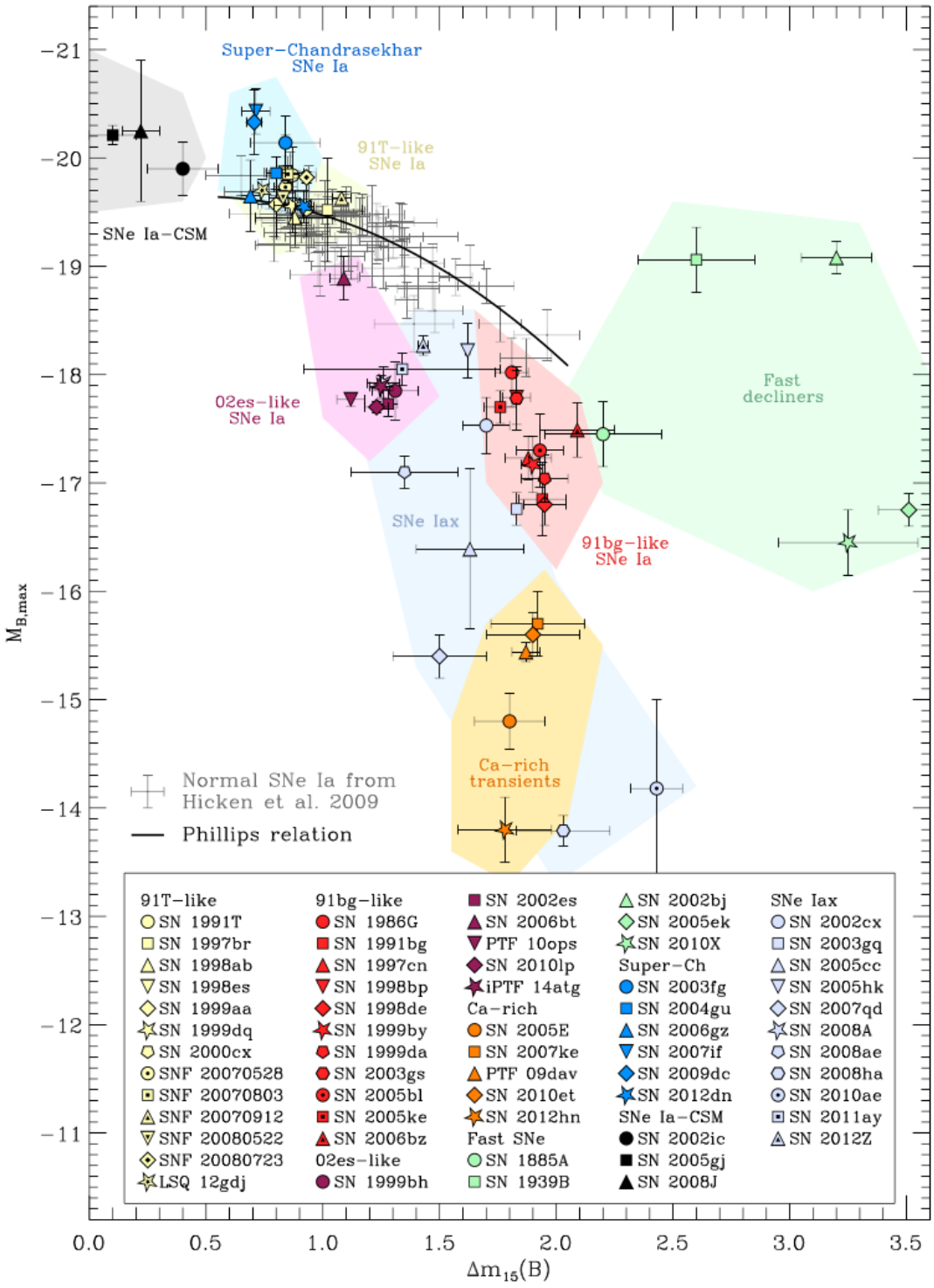

FIGURE 1.6: SN Ia subtypes as in Taubenberger (2017). The black line represents the Phillips relation of light curve vs. width which 'normal' SNe Ia follow. SNe Ia that do not follow the relation are listed and divided in families by type of observed features.

1.3 Gamma rays from SN Ia

The energy emitted by SNe Ia is predominantly originated by the radioactive decay: ^{56}Ni $\rightarrow$ ^{56}Co $\rightarrow$ ^{56}Fe. ^{56}Ni is the dominant product of neutron-poor explosive burning conditions (Truran et al., 2012). The thermonuclear burning of a C/O WD is an ideal environment for the nucleosynthesis of this isotope. It requires a composition of Z=N elements (like ^{12}C, ^{16}O or ^{28}Si) and densities high enough to reach a peak temperature of T $>$ 4×10^9 - 5×10^9 K. These conditions allow an explosive burning of carbon and oxygen which happens in a faster timescale (fractions of a second) than the timescale needed for weak force to convert proton to neutrons. This favours the formation of proton enriched nuclei like ^{56}Ni.

The ^{56}Ni synthesised during the explosion is unstable and decays into the daughter nucleus of ^{56}Co. The decay takes place via electron-capture with a half-life time of t_{Ni}=6.10 days. The total energy of this decay is E_{Ni} = 1.728 MeV. ^{56}Co is also an unstable nucleus that decays into stable ^{56}Fe. It has a half life time of t_{Co}=77 days and it decays via electron-capture (80%) or β^+ decay (20%). The total energy of this decay is E_{Co} = 3.566 MeV. A scheme of the radioactive decay is shown in Figure 1.7.

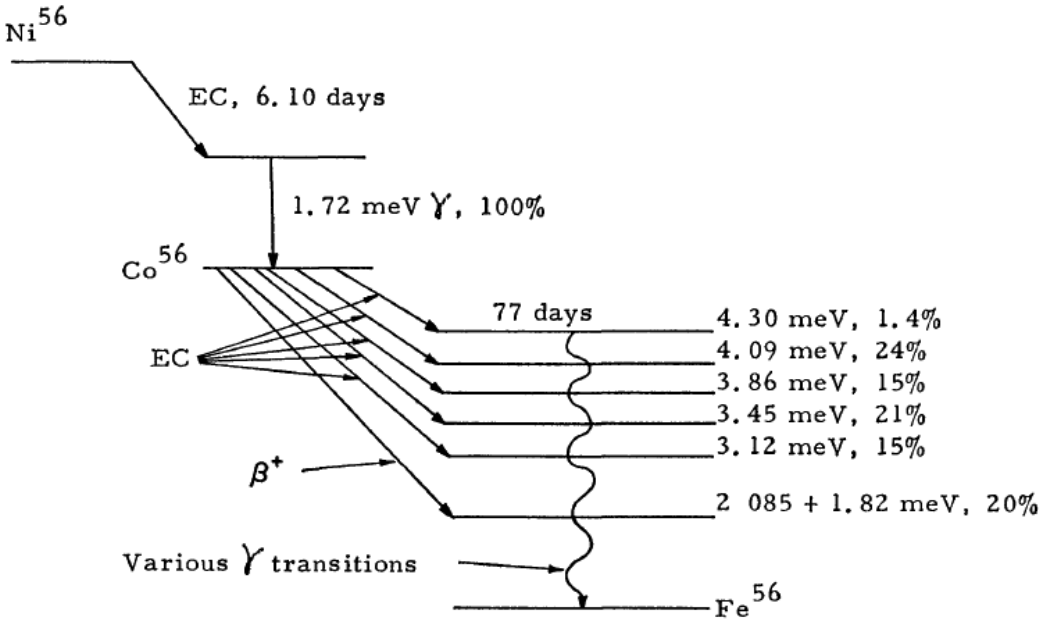

FIGURE 1.7: Radioactive decay: ^{56}Ni $\rightarrow$ ^{56}Co $\rightarrow$ ^{56}Fe. ^{56}Ni decays to ^{56}Co via electron-capture (EC) and ^{56}Co decays to ^{56}Fe via EC (80%) or β^+ decay (20%). Figure from Lederer et al. (1967).

The radioactive decay of ^{56}Ni $\rightarrow$ ^{56}Co $\rightarrow$ ^{56}Fe is a source of gamma-ray photons that interact with the ejecta by photoelectric absorption, Compton scattering or pair production (a further explanation of these processes is made in Chapter

2). On a thick SN Ia ejecta, with high opacity, the gamma-ray photons will be thermalized to ultraviolet, optical or infrared photons. Once the ejecta is thin enough, due to its expansion, the gamma-ray photons can escape without being thermalized and they can be detected. Most of the studies or observations on SNe Ia are made on the optical and infrared energy range. However, they are subject to many uncertainties due to their heavy dependence in the characteristics of the ejecta. Gamma-ray photons from SNe Ia provide a more precise and direct interpretation due to the simplicity of the physic processes they experience (Burrows and The, 1990; Gomez-Gomar et al., 1998; Milne et al., 2004; Sim and Mazzali, 2008; Isern et al., 2008).

The detection of gamma-ray photons from SNe Ia allows to obtain multiple features that can be useful diagnostic tools. A wide time period observation of a gamma-ray light curve allows us to measure the synthetised ^{56}Ni quantities. If detected at early stages, the gamma-ray light curve is sensitive to the distribution of ^{56}Ni in the ejecta. The detection of gamma-ray lines from this decay gives clues about the kinematics and morphology of the explosion. This information can be obtained by measuring their intensity, broadening and the time they emerge. The most prominent lines from ^{56}Ni decay are 158, 480, 750, and 812 keV and from ^{56}Co decay are 847 and 1238 keV. The detection of ^{56}Ni lines can be complicated because the mean lifetime of the ^{56}Ni decay is $\sim$8.8 days. At this time the ejecta is not thin enough if the ^{56}Ni is found in the inner layers of ejecta. Its gamma-ray photons will not be able to escape without being thermalized. However, if there is ^{56}Ni in the outer layers the gamma-ray photons from the decay could be detected. Their detection could inform us about explosive burning in the outer layers of the SN. The lines from ^{56}Co decay can be detected right after the maximum of the optical light curve and the following months. This is because the ejecta is thin enough in that stage of the explosion. Another way to use gamma-ray spectra for diagnostic tools is to measure the line ratio between ^{56}Ni and ^{56}Co lines (Gomez-Gomar et al., 1998; Sim and Mazzali, 2008). Even if there is a low sensitivity, we still could measure the hardness ratio. The ratio could be done between a hard energy range of the spectra (a line dominated region) and a soft energy range (a continuum dominated region). These listed diagnostic tools show the usefulness of gamma-ray lines detection. It can provide a precise knowledge of the nucleosynthesis of SNe Ia and a deeper understanding of their progenitor system and explosion mechanism.

1.3.1 Models

Some studies aim to forecast SNe Ia observables by creating models that simulate the explosion. The depiction of the whole explosion can be decoupled in two phases. The first phase describes the hydrodynamics of the explosion. The second describes the free expansion of the ejecta. It starts few seconds after the ignition when the relative positions of the fluid elements do not change any more (Röpke, 2005).

The first simulations are known as hydrodynamic models. They simulate the ignition of the thermonuclear flame for different progenitor scenarios. Their outcome is a set of parameters that represent the geometry, kinematics and composition before the free expansion of the ejecta. The second phase aims to model the homologous expansion of the ejecta and the processes of the radiation on it. These models are know as radiative transfer models. Their outcome allows to model the synthetic observables of the explosion like the spectra or light curve. A deeper understanding of gamma-ray transfer models can be found in Chapter 2. The outcome parameters from hydrodynamic models are used as input parameters to compute the radiative-transfer models. Hydrodynamic models are complex to design because they aim to represent accurately the different explosion models. Sometimes, instead of using an input of parameters from these types of models, studies use a simplified version based on some physically motivated assumption.

The modelling of SN Ia started by making one-dimensional radiative transfer codes. These codes tried to test different configurations of explosive mechanism (as in Section 1.2.2). A scenario that 1D models have simulated and seems to agree with many observations is a delayed detonation in a Chandrasekhar mass WD.

Due to the computing-demanding nature of these codes, 1D codes allowed to simplify the problem. However, to reproduce more realistic events, three-dimensional codes were built. These 3D codes allowed to simulate asymmetries produced by the hydrodynamic phase of the explosion. With the introduction of 3D codes synthetic observables were dependent of the viewing angle. These asymmetric models could explain better the diversity of SNe Ia. The dependence of the viewing angle was mostly at early times meanwhile at later times the observables were similar to the ones from 1D models. Therefore, theoretical models support the idea that gamma-ray detection before the optical peak can provide a window of new information about the nature of these events.

Some of these 1D and 3D codes just focus on the radiative transfer of UVOIR radiation by estimating the energy deposition of gamma-ray photons (Lucy, 1999b; Kerzendorf and Sim, 2014). However, some codes introduced the treatment of gamma-ray transfer explicitly to reproduce the whole radiation transfer in the ejecta (Lucy, 2005; Kasen et al., 2006; Kromer and Sim, 2009). Some codes have focused only in reproducing the gamma-ray transfer and its observables (Ambwani and Sutherland, 1988; Gomez-Gomar et al., 1998; Sim and Mazzali, 2008; Isern et al., 2008). For a comparison of multiple 1D gamma-ray transfer codes see Milne et al. (2004).

1.3.2 Observations

Observations of type Ia SNe in gamma-ray are scarce compared to the detection of them in the optical band. Past and current gamma-ray missions have had poor sensitivity in the ∼0.1-10 MeV range, or also commonly known as the '1 MeV gap' (see colored area in Figure 1.8). This area is where gamma emission

from SNe Ia peaks (their gamma nuclear lines are formed around 0.1 MeV-3.5 MeV). Therefore, it has complicated the detection of such event. SNe Ia that have been detected with gamma-ray instruments are: SN 1991T, 1998bu , SN 2011fe and SN 2014J.

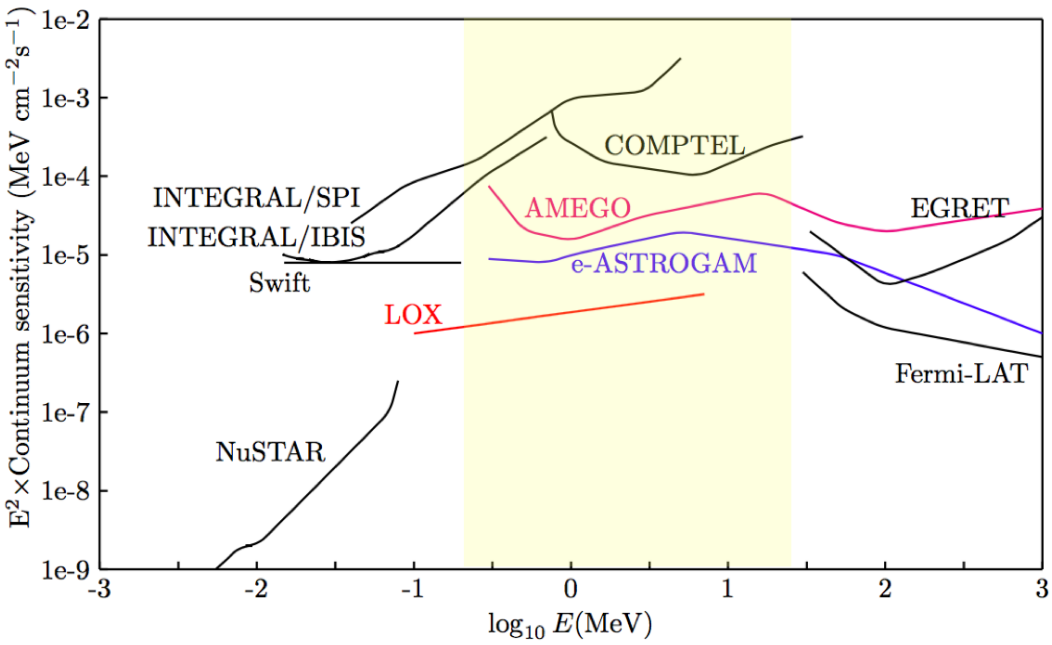

FIGURE 1.8: Approximate point source continuum sensitivities of different instruments. The colored yellow area shows the energy range in which past and current gamma missions have had a poor sensitivity, know as the '1 MeV gap'. In black we show past and current missions. Colored lines display proposed future missions. Source: edited from Isern et al. (2021).

The Compton Gamma-ray observatory (CGRO) detected SN 1991T (Lichti et al., 1994) and 1998bu (Georgii et al., 2002). CGRO was a mission launched in 1991 that ended in 2000. It covered an energy range from 30 keV to 20 GeV (Gehrels et al., 1993). The flux from these two SNe Ia was too weak to be able to compare them to theoretical models.

The INTErnational Gamma-Ray Astrophysics Laboratory (INTEGRAL) detected SN 2011fe and SN 2014J (Isern et al., 2021). The mission was launched in 2002 and it is still working. A deeper explanation about INTEGRAL is found in Chapter 4. SN 2011fe was detected at the early days after the explosion at a distance of 6.4 Mpc. The gamma-ray detection made by SPI and IBIS/ISGRI (on board of INTEGRAL) only could provide limits to the expected emission of ^{56}Ni. Isern et al. (2013) favoured a Chandrasekhar mass WD scenario as progenitor system and proposed a delayed detonation as explosion mechanism responsible to synthesize $\sim$0.55 $M_\odot$ of ^{56}Ni, although the study suggested other mechanism could be possible. SN 2014J was detected at 3.5 Mpc and INTEGRAL was able to observe it 16.5 days after the explosion. The distance in which it was detected made it the closest SN Ia since SN1604 (Kepler's SN).

An excess ^{56}Ni in the early stages of the observation was detected, which implies the presence of radioactive material in the outer layers (Isern et al., 2016), suggesting a non spherical structure.

As for future observations, a Galactic supernova would be ideal for more detailed studies, specially if detected during the rising epoch of the light curve. An study of the sensitivity of INTEGRAL to detect these possible events is found in Chapter 4. Future gamma-ray missions could improve the detection of these events and narrow down the unresolved questions about the nature of SNe Ia. In Figure 1.8 we see proposed future missions: LOX, AMEGO and e-ASTROGAM. Another future mission that was proposed and already accepted is the Compton Spectrometer and Imager (COSI). The new space telescope COSI will observe the gamma-ray sky in the 200 keV - 5 MeV range (Tomsick and COSI Collaboration, 2022). The mission is expected to be launched in 2025. COSI will be able to monitor the entire sky within a day due to its pointing strategy and having a large field of view. The new mission is expected to have a better sensitivity than SPI and COMPTEL (from INTEGRAL and CGRO respectively), see Figure 1.9.

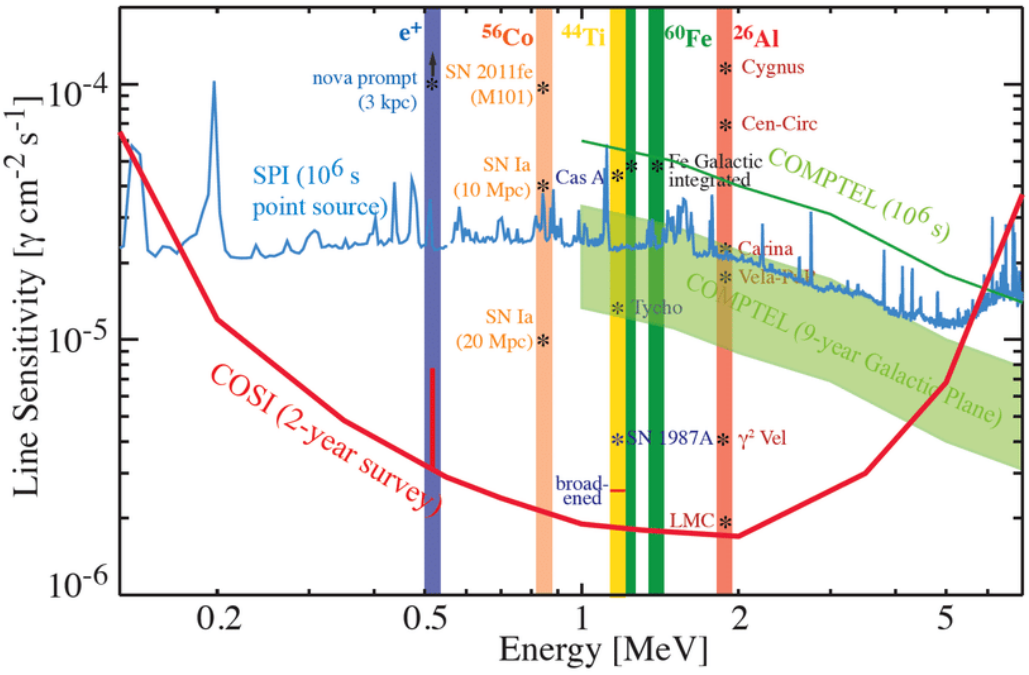

FIGURE 1.9: The COSI narrow line sensitivity for point sources (3 σ) compared with COMPTEL and INTEGRAL/SPI. Source: Tomsick and COSI Collaboration (2022).

Chapter 2

Gamma-ray radiative transfer model

This chapter aims to describe the 3-dimensional code built to simulate the gamma radiation transfer of SN Ia. We present an overview of the essential theory on which it is based in section 2.1. An explanation of how the code operates is in section 2.2. Finally, we proceed to test the code in section 2.3.

2.1 Overview of the code

The study of electromagnetic radiation in astrophysics needs an understanding of the creation and propagation of particles in environments that are simply unreachable for us the observers. To compensate for that, the study of radiative transfer has aimed to describe the physics of electromagnetic radiation in many astrophysical scenarios. Due to the complexity of solving analytically these radiation processes, simulations of probabilistic fashion that reproduce the radiation quanta allow to solve the challenge in a simpler manner. Monte Carlo's method offers an accurate approach to the radiative transfer problem. This method has been extensively used in previous studies that simulate the radiative transfer on different expanding astrophysical environments, such like stellar winds (Abbott and Lucy, 1985; Sim, 2005; Vink et al., 2011), star formation (Harries, 2015; Harries et al., 2017) or supernovae (Hoeflich et al., 1992; Gomez-Gomar et al., 1998; Hungerford et al., 2003; Kasen et al., 2006; Sim, 2007; Kerzendorf and Sim, 2014), some of them focusing only on gamma radiation which is our case.

We have applied Monte Carlo's method to reproduce the propagation of gamma-ray photons inside the expanding ejecta of SN Ia in a stochastic manner by creating a Python code. We have build a 3D system of Cartesian coordinates that mimic the real geometry and kinematics of a supernova model in homologous expansion. The Cartesian grid is made up of cubic cells that represent the discretization of the supernova's domain. Each cell has physical parameters that describe the initial composition of the ejecta and numerical parameters to ease the computation. The gamma photons will be emitted by the radioactive decay of nucleosynthesis products from the initial composition of the cells. The photons are not simulated one by one, instead we use the term of indivisible energy

packets to ease the simulation. Indivisible energy packets represent a bundle of photons instead of one itself (for further understanding see section 2.1.2). The gamma-packets paths are traced through the domain following the probabilistic interaction laws we have sampled using Monte Carlo's method approach (see 2.1.1). The interactions that the gamma-packets experience can be of physical nature or numerical nature. Physical nature interactions that gamma photons can experiment in our code are photoelectric absorption, Compton scattering or pair production. These interactions will change the energy and direction of the gamma-packets or will end their propagation by being absorbed or converted to electrons. The numerical interactions are due to the design of the experiment and the proper calculation of the simulation, such like the stop of the propagation due to reaching the time step in which the simulation is discretized or due to crossing the cells in the grid. The packets are followed until they escape the domain. The escaping gamma-packets parameters are saved and used to construct the spectra and light curve of the simulated model. The 3-dimensional approach allows to build spectra from various points of view to see the change on the line profiles that asymmetric geometries create. This gives us a realistic outlook of the simulated models in a similar way the observation of supernovae would be made by real instruments.

The statistical nature of the simulation, due to the use of Monte Carlo's method, makes the output results subject to statistical noise. This can be improved by sampling a bigger size of gamma-packets, but it causes highly demanding computational jobs. However, the method allows parallelization of the simulation, due to the bosonic character of the simulated photons, which means that the bundle of photons the gamma-packets represent do not interact with each other. This allows to treat a subset of multiple gamma-packets from the same experiment on different processors and speed up the computation (see section 2.3.3).

2.1.1 Monte Carlo fundamental principle

The basis of Monte Carlo method relies on the so-called Fundamental Principle. It allows to construct the solution of a mathematical or physical process by generating random numbers that are used to sample a function that describes the process in a probabilistic fashion (House and Avery, 1968).

If the probability distribution function of a physical process is defined as $f(x)$, we desire to sample a sequence of random numbers r that yields x values distributed accordingly to $f(x)$. That is to say we need a relation $x(r)$ that allows $f(x(r))$. We define r as a sequence of uniform values from 0 to 1 that follows a probability distribution function $g(r)$. Where $g(r)$ can be defined as:

$$g(r) = \begin{cases} 1 & 0 < r < 1 \\ 0 & \text{otherwise} \end{cases} \tag{2.1}$$

The probability to get a certain r value inside the interval $[r,\, r + dr]$ is $g(r)dr$. This should be equal to the probability of finding a certain x value inside the

interval $[x(r),\ x(r) + dx(r)]$, or also defined as $f(x)dx$. In order for the relation $x(r)$ to be correct the following relation must be achieved $F[x(r)] = G(r)$. Where $F[x(r)]$ and $G(r)$ are the cumulative distribution functions of the probability functions $f(x)$ and $g(r)$. If $x(r)$ is certain we can also state that the probability of $r < r'$ is the same as $x < x(r')$. Inspecting equation 2.46 we see that the cumulative distribution $G(r) = r$. Therefore, $F(x)$ can be defined as:

$$F[x(r)] = \int_{-\infty}^{x(r)} f(x')dx' = \int_{-\infty}^{r} g(r')dr' = r \tag{2.2}$$

and so the cumulative distribution function $F(x)$ of the probability distribution $f(x)$ is uniformly distributed from 0 to 1. Therefore, solving $\int_{-\infty}^{x(r)} f(x')dx' = r$ and isolating x allows to find a relation $x(r)$ where x values r that are subject to random values from 0 to 1. For further detail on Monte Carlo method we suggest to examine Carter and Cashwell (1975) and Cowan (1998).

2.1.2 Indivisible energy gamma-packets

In the experiments where Monte Carlo's techniques are used to simulate radiative transfer in a volume, the radiation is discretized into test particles that mimic the propagation of real photons. Past studies used to discretize the radiation in the so-called photon-packets (Avery and House, 1968; Pozdnyakov et al., 1983; Ambwani and Sutherland, 1988). Each photon-packet was a bundle of photons that behaved like one photon. As the photon-packet experimented physical interactions the energy would change, as a real photon. As a consequence, the weight of the photon-packet in the simulation would change too. This created problems in the total energy conservation of the simulation. It also complicated the tracking of each test particle because new photons were created in some interactions. To improve this issue, L. Lucy came up with a new approach to the discretization of the energy on Monte Carlo's radiative transfer simulations. He proposed to discretize the radiation in packets of the same amount of energy in Abbott and Lucy (1985), and in later works he further developed the concept (Lucy, 1999a; Lucy, 1999b; Lucy, 2002; Lucy, 2003). Having packets of the same amount of energy implies that the weight of each test particle is the same. Also this weight remains constant along all the simulation, from creation to escape from the domain, due to its indivisibility. The energy-packet approach has multiple advantages regarding the photon-packet one. It enables an easy way to maintain energy conservation. It avoids the need to process packets that have very low energy and burden the simulation. It also allows to follow the created packets one by one without having to follow multiple packets that may be created along the way.

In our code we use the energy-packet approach applied just to gamma radiation, and therefore we call them gamma-packets. The introduction of gamma-packets in these kind of studies was made in Lucy (2005), and so we base our work on it. The gamma-packet energy will be defined by the total amount of initial

energy coming from the radioactive decay chains that fuel the supernova and the amount of test particles we desire to simulate:

$$E_{packet} = \frac{M_{rad}}{N_p} \tag{2.3}$$

where M_{rad} is the amount of radioactive mass in the model and N_p is the number of packets in the experiment. Each gamma-packet has an amount of photons related to the energy the photons $E_{photons}$ on the packet have:

$$N_{photons} = \frac{E_{packet}}{E_{photons}} \tag{2.4}$$

The $E_{photons}$ changes the same way the energy of a single photon would when interacting with matter. However, the E_{packet} remains the same. In consequence, the amount of photons in the packet will change. That is to say when $E_{photons}$ decreases the $N_{photons}$ in the gamma-packet will increase. For example, if initially we have a gamma-packet with E_{packet}=1 MeV and $E_{photons}$=0.1 MeV, the packet have an initial amount of $N_{photons}$=10. If the gamma-packet experiences an interaction and now $E_{photons}$=0.01 MeV, to keep E_{packet} constant the gamma-packet will have now $N_{photons}$=100.

2.2 Outline of the code

In this section we are going to explain in detail the modus operandi of the code. A summary of the main operations is illustrated in Figure 2.1, which shows a flow chart of the code.

2.2.1 Building of the domain

The domain of the experiment will be enclosed in a 3D Cartesian grid. For the creation of the grid a set of coordinates $x_1, x_2, y_1, y_2, z_1, z_2$ will be set to define the vertices of multiple cubic cells that will create a big cube in which the domain will be enclosed (see blue grid in Figure 2.2). The volume of each cell is set as 1^3, and its coordinates are saved. Generally, each model will be based on a sphere and in some cases asymmetries will be added. To define the domain of the model to the shape of a sphere we first define the middle point of each cell as:

$$r = \sqrt{\left(\frac{x_1 + x_2}{2}\right)^2 + \left(\frac{y_1 + y_2}{2}\right)^2 + \left(\frac{z_1 + z_2}{2}\right)^2} \tag{2.5}$$

Then a simple condition as:

$$r < R_{sph} \tag{2.6}$$

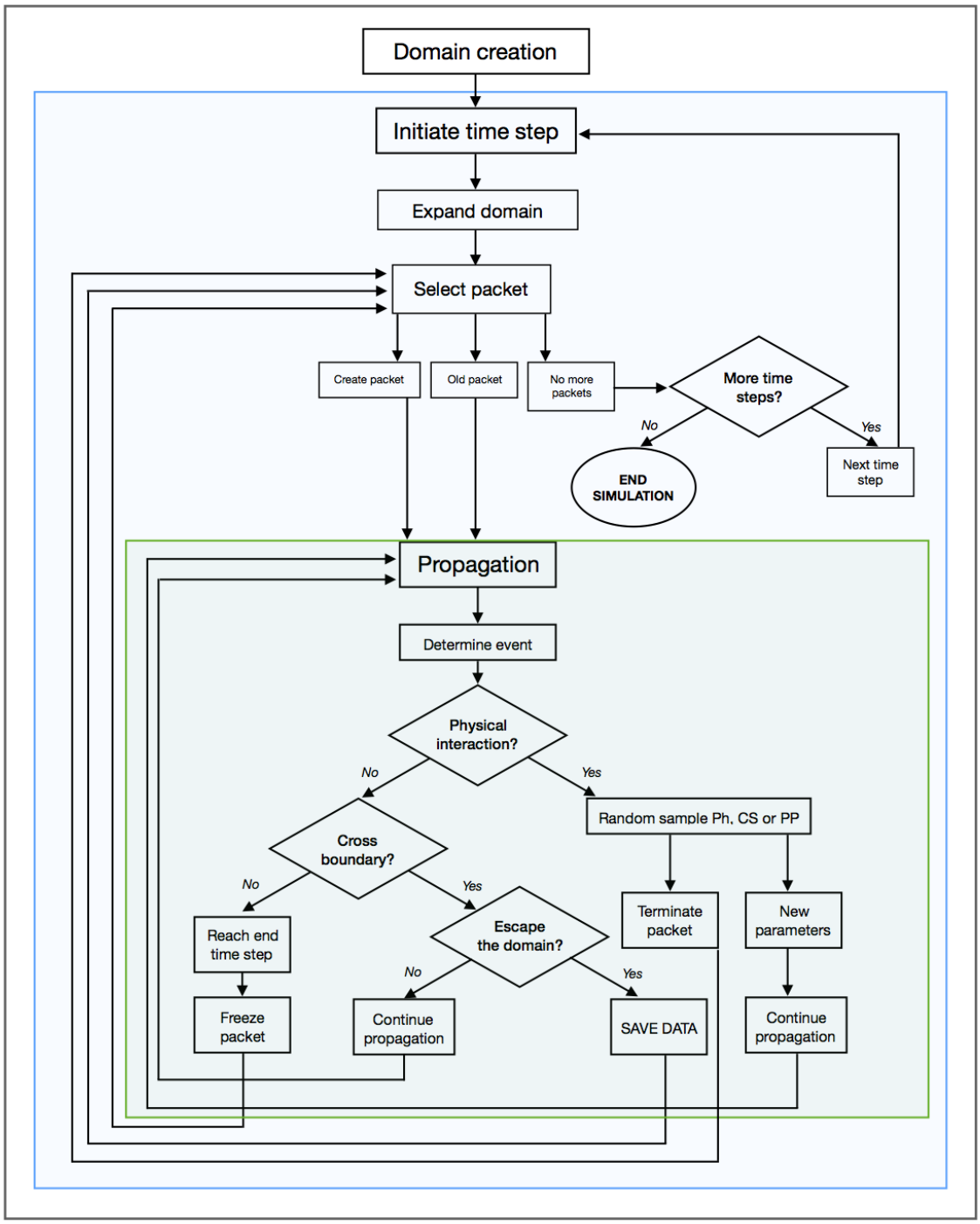

FIGURE 2.1: Flow chart showing the main operations of the Python code simulating a 3D SN Ia explosion in homologous expansion.

allows to keep the cells inside the radius of a sphere, R_{sph}. This process is illustrated in Figure 2.2, where a sphere geometry is appreciable even for a low number of cells. The number of cells is higher for more realistic models in order to have more accuracy on the geometry.

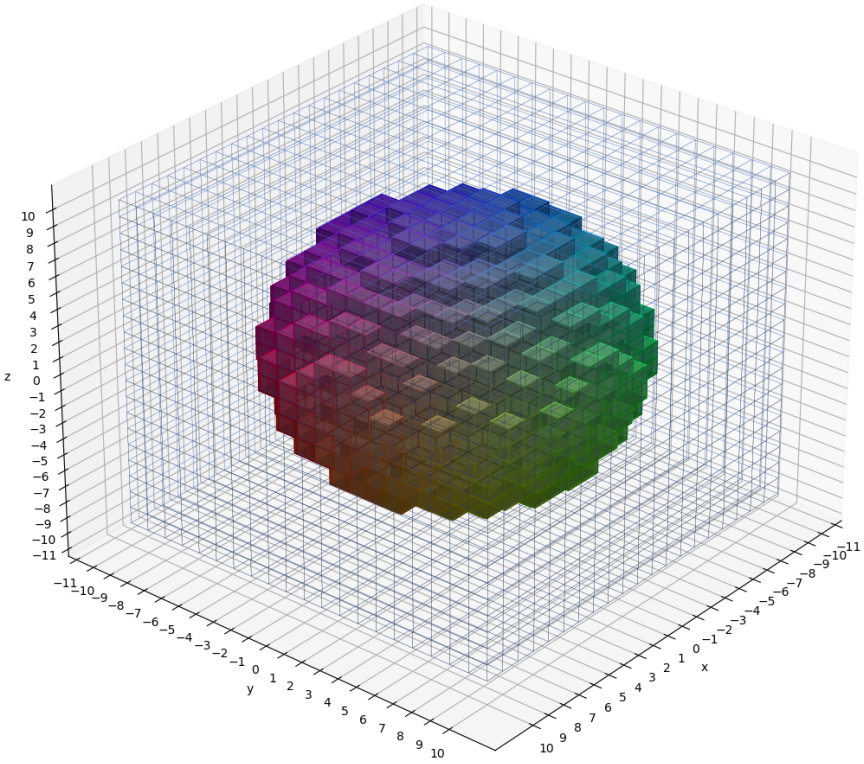

FIGURE 2.2: Example of a sphere as the domain of the simulation. We show a big cube made of multiple small cubes in blue. The cubes that follow the condition of eq. 2.6 are coloured and define the sphere.

More complex geometries need extra conditions. For example, a cone attached to a sphere is a geometry that will be used at Chapter 3. The cells that will define the cone need to fill these two conditions:

$$R_{sph} < r < R_{cone} \tag{2.7}$$

and

$$\alpha < cos^{-1}\left[\frac{\frac{z_1+z_2}{2R}}{\sqrt{\left(\frac{x_1+x_2}{2R}\right)^2+\left(\frac{y_1+y_2}{2R}\right)^2+\left(\frac{z_1+z_2}{2R}\right)^2}}\right] < \beta \tag{2.8}$$

where R_{cone} is the radius of the cone, α and β are the angles in which the cone will be enclosed. An example of this geometry is shown in Figure 2.3.

Several subdomains are defined from the main one in order to define regions in which the SN Ia composition is discretized. The most common geometry set up is a sphere with multiple spherical layers of different thickness. Every cell in each layer has the same density and composition of elements, therefore all the cells that form the subdomain will share the same parameters. A layer is defined by the cells that their central point is found between the domain of two

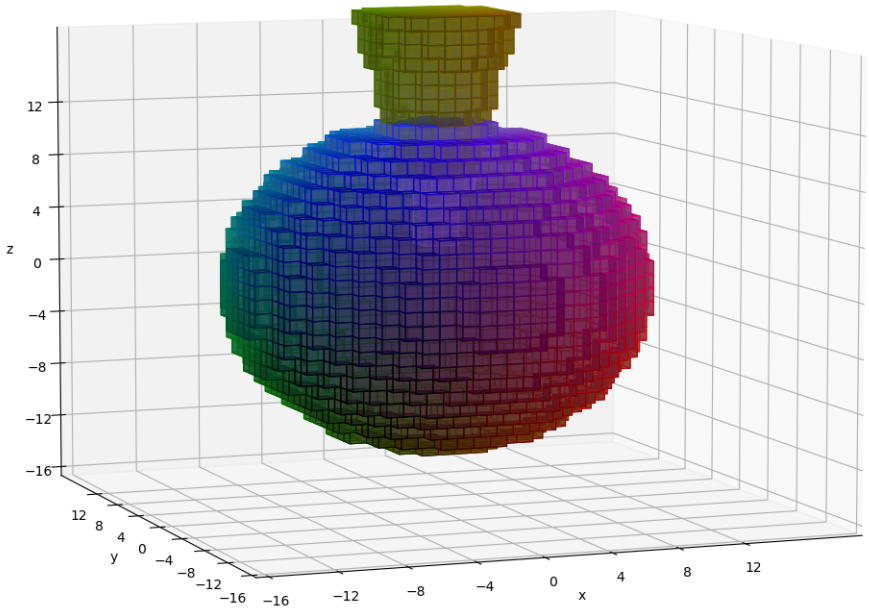

FIGURE 2.3: Assymetric domain made of a sphere with an attached cone on top.

radii distances, $R_1 < r < R_2$. A simple example for illustration of multiple layers with the same thickness is shown on Figure 2.4.

Each cell will have stored parameters that define the physical and chemical composition of the SN explosion at the beginning of its homologous expansion. For the purpose of the simulation, there are also initial parameters aimed to simplify the computation. These parameters are: **position**, **volume**, **mass**, **density**, **velocity**, **fraction of elements**, **number of radioactive decays** and **decay time**.

The **position** of each cell is given by the coordinates of the vertices normalized with respect to the real model dimension. Given the value x_1, the real physical position is computed as:

$$p_{x_1} = \frac{R_{SN}}{R_n} \cdot x_1 \tag{2.9}$$

where R_{SN} is the radius of the SN at the beginning of the simulation and R_n is the total radius in units of cubic cells. The same is applied to the other values of coordinates x_2, y_1, y_2, z_1, z_2. Using the same reasoning, the **volume** of each cell at the beginning of the simulation is computed as:

$$V = \left(\frac{R_{SN}}{R_n} \cdot (x_2 - x_1) \right)^3 \tag{2.10}$$

Either the **mass** or **density** are arbitrarily selected in order to reproduce the desired distribution. If the mass value is determined then the density will be computed as $\rho = M/V$. If we prefer to define the density in the beginning then the mass is computed as $M = \rho \cdot V$.

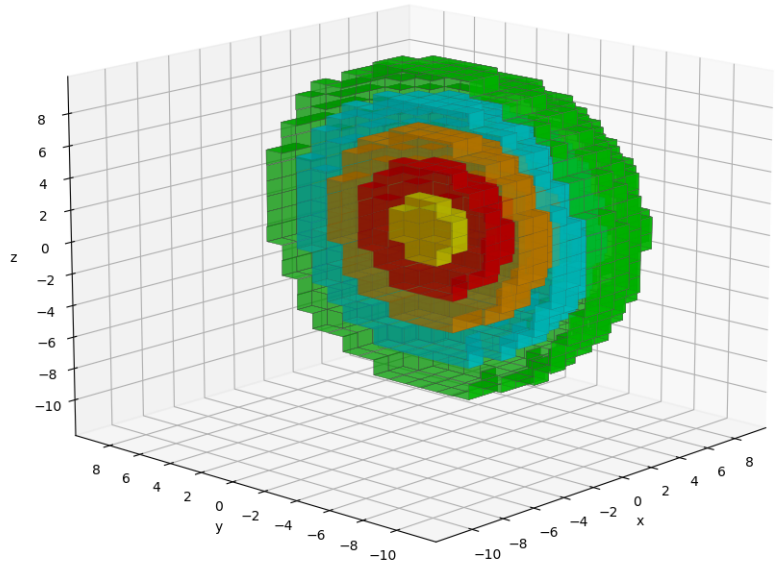

FIGURE 2.4: Sphere cut in half to show the definition of sub-domains. Each color represents the cells that have the same composition parameters.

Each element has a determined **fraction** defined in each cell. The fraction of each element, X_{el} is:

$$X_{el} = \frac{M_{el}}{M_{cell}} \tag{2.11}$$

where M_{el} is the mass of the element in the cell and M_{cell} is the total mass of the cell. If the total fraction of element in a cell is set to 1, it must hold:

$$\sum_{el} X_{el} = 1 \tag{2.12}$$

The elements can be non-radioactive or radioactive. $X_{non\,rad}$ represents the fraction of non radioactive elements and X_{rad} the radioactive ones. The X_{rad} and the mass of each cell will determine the amount of radioactive decays that take place on each cell. We set a fixed amount of **number of decays** or 'pellets' that will take place in the supernova, following the theory of gamma-packets seen on section 2.1.2. A pellet represents one indivisible packet of radioactive material before decaying into a gamma-packet. Once the number of pellets is set for each cell we will compute the **time of decay** of each of them. The time of decay will be stored to be used later on the simulation, when the gamma-packets are created right before being propagated. The time of the decay is sampled using MC techniques (see Lucy, 2005). The probability distribution function of an exponential decay is:

$$f_d(t) = \frac{1}{\tau} e^{\frac{-t}{\tau}} \tag{2.13}$$

where τ is the mean lifetime of the decay. Using the Fundamental Principle, see section 2.1.1, the cumulative distribution function of this probability is:

$$e^{\frac{-t}{\tau}} = z \tag{2.14}$$

where z is a uniform random number from (0,1]. Isolating the decay time we are left with the expression:

$$t = -\tau \cdot ln(z) \tag{2.15}$$

The decay chain ^{56}Ni $\rightarrow^{56}$Co $\rightarrow^{56}$Fe is the main source of energy in the supernova and its pellets are the main source of gamma-packets in our code. If the mean lifetime (or e-folding value) of the decay is related to the half-life time ($t_{1/2}$) as :

$$t_{1/2} = \tau \cdot ln(2) \tag{2.16}$$

The sampled decay times for the chain are:

$$t_{Ni} = -8.8 \cdot ln(z_{Ni}) \tag{2.17}$$

$$t_{Co} = t_{Ni} - 111.7 \cdot ln(z_{Co}) \tag{2.18}$$

where z_{Ni} and z_{Co} are different random numbers.

The amount of pellets is fixed at the beginning of the simulation. The selection of ^{56}Ni or ^{56}Co pellets is done by sampling the ratio of their total decay energies. A fraction of $E_{Ni}/(E_{Ni} + E_{Co})$ will be ^{56}Ni pellets and the other ^{56}Co pellets.

The sampling of the time decay of this chain is shown on Figure 2.5 to test the method.

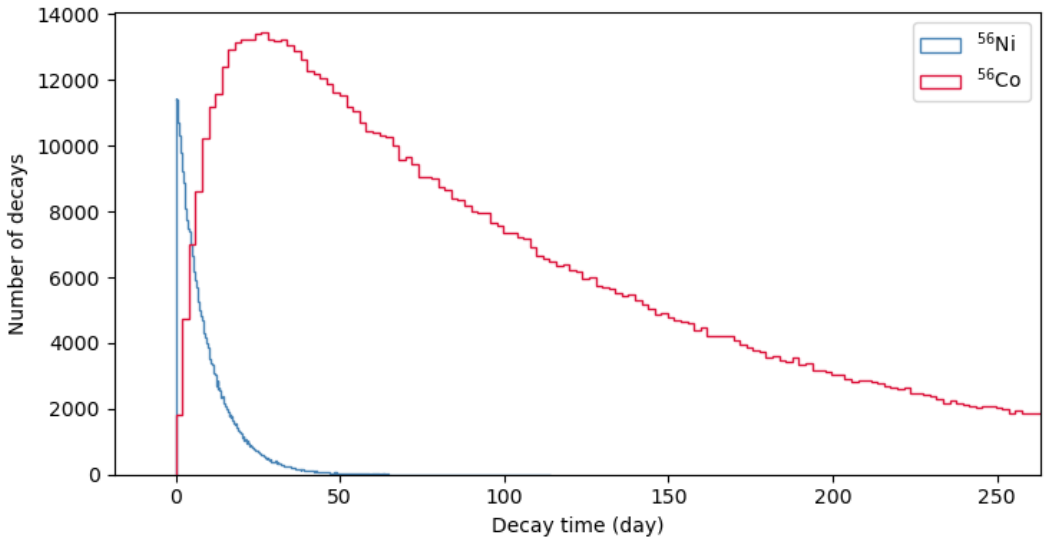

FIGURE 2.5: Sampled time profiles of $1.4 \cdot 10^6$ decays using equations 2.17 and 2.18. We show the distribution of number of decays along the time of the simulation. ^{56}Ni in blue and ^{56}Co in red.

Finally, the **velocity** of each cell is defined by the velocity vector as $\boldsymbol{v} = (v_x, v_y, v_z)$, where v_x, v_y and v_z are the velocity of each external wall of the cell.

2.2.2 Discretization of the expansion

We can consider that SN Ia experiences an **homologous expansion** right after a few seconds after the ignition (Röpke, 2005). The kinetic energy of the ejecta in an homologous expansion becomes dominant because of its free expansion. In this scenario the relative position of the elements in the ejecta does not change. Its position r can be described with a very simple relation:

$$r = v \cdot t \tag{2.19}$$

where v is the velocity of the fluid and t the time since the beginning of the expansion. The velocity vector of each cell comes defined by their relative position in the domain.

In order to simulate the expansion in our code, we discretize it in S steps. The steps have a length of 1 day of explosion. For each step the grid will be expanded in function of the growth that each cell will undergo. During the expansion the parameters of each cell remain constant except for the new position of the walls and the density. As the mass (M) of the cell remains constant but the volume does not due to the change of dimension of the cell, the density (ρ) drops proportionally to t^{-3}.

2.2.3 Gamma-packet creation

At the beginning of each time step ($\Delta t = 1$ day), we create a gamma-packet for each of the radioactive decays happening on that day. Each cell has an amount of radioactive pellets with an associated decay time. If the time of decay of the pellet is between the date of the step, t_S to t_{S+1}, then a gamma-packet is created with a random position inside that cell. This process is made for all the cells.

Each gamma-packet is defined by the following parameters: **time**, **energy of the packet**, **energy of the photons** inside the packet, **position**, **direction** and **cell number** where the packet is at the current moment. This parameters allow to track down the transport of the gamma-packets and the physical processes they experience.

The **time** at the initialisation of the gamma-packet is defined by the decay time. Then the time will continue increasing once the gamma-packet starts its transport along the grid.

The initial **position** of the gamma-packet is chosen by sampling a number between the x coordinates, y coordinates and z coordinates of the boundaries of the cell, defining a random position to the gamma-packet inside the cell in which the decay had taken place. Each gamma-packet has a **direction** assigned to start its propagation. The direction consists of a vector $\boldsymbol{n} = (n_x, n_y, n_z)$, its components are defined as:

$$\begin{aligned} n_x &= sin(\theta) \cdot cos(\varphi) \\ n_y &= sin(\theta) \cdot sin(\varphi) \\ n_z &= cos(\theta) \end{aligned} \tag{2.20}$$

where φ is the azimuth angle and it is sampled from 0 to 2π. θ is the theta angle and is sampled from 0 to π. The relation of these angles with the cartesian coordinates is shown on Figure 2.6.

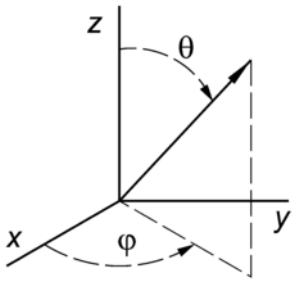

FIGURE 2.6: Representation of azimuth angle φ and theta angle θ in relation to 3D cartesian coordinates. These angles define the direction of a gamma-packet

The **energy of the packet** is defined by the number of gamma-packets (N_p) the total energy is divided by (see section 2.1.2):

$$E_{gpacket} = \frac{E_{total}}{N_p} \tag{2.21}$$

where E_{total} is the total amount of radioactive energy in the simulation. For a simulation where the ^{56}Ni decay chain is the only radioactive element, the E_{total} is calculated as:

$$E_{total} = \frac{(E_{Ni} + E_{Co}) \cdot M_{rad}}{m_{Ni}} \tag{2.22}$$

where E_{Ni}= 1.728 MeV, E_{Co}= 3.566 MeV (see 1.3) and they are the total energy emitted per decay. M_{rad} is the total mass of ^{56}Ni and ^{56}Co in the ejecta (defined in the initial cell parameters and remaining constant along the explosion) and m_{Ni} is the nuclear mass of ^{56}Ni. The total energy emitted by the decay is the sum of the energy of each decay line E_l multiplied by its probability to happen: $\sum E_l \cdot f_l$. This probability f_l allows to sample the initial **energy of the photons** ($E_{photons}$) that the gamma-packet will have. The f_l for each line in the decay chain ^{56}Ni $\rightarrow^{56}$Co $\rightarrow^{56}$Fe is shown in the table 2.2.3 (as seen in Ambwani and Sutherland, 1988). The initial value of $E_{photons}$ is sampled from these probabilities. The decay chain of 48Cr is also used in this work in 3.3, its main parameters are in Appendix A.1.

A different approach can be made for the line of 0.511 MeV. This line is created during the decay of ^{56}Co. It is made by the annihilation of electrons with the positrons created in the $\beta+$ decay processes. The annihilation releases the rest energy of the particles (two photons of 0.511 MeV). However, in some cases a bound state with an electron and a positron can be made. This is called positronium. The positronium is unstable and it decays into three gamma photons (orthopositronium) with energies below 0.511 MeV. Orthopositronium is further explored in Appendix A.2.

Gamma-ray line and probabilities list			
Energy (MeV)	f_l	Energy (MeV)	f_l
0.158	1.00	1.238	0.6758
0.270	0.36	1.360	0.0428
0.480	0.36	1.443	0.0020
0.750	0.50	1.772	0.1600
0.812	0.87	1.811	0.0048
1.562	0.14	1.964	0.0072
		2.015	0.0309
0.511	0.3800	2.035	0.0795
0.734	0.0021	2.213	0.0063
0.788	0.0030	2.598	0.1672
0.847	0.9998	3.010	0.0100
0.978	0.0144	3.202	0.0303
1.038	0.1408	3.254	0.0743
1.140	0.0015	3.273	0.0176
1.175	0.0224	3.452	0.0086

TABLE 2.1: Decay energies and its probabilities for ^{56}Ni (six first entries) and ^{56}Co (rest of entries). Source: Ambwani and Sutherland (1988).

2.2.4 Change of reference frame

The velocity of the ejecta in SN Ia reaches values of tenths of the speed of light. Therefore, we need to take into account the relativistic effects in the simulation. A Doppler shift effect will be experienced by the energy of the gamma-packets and the photons within, in the reference frame (RF). The RF is considered to be the Cartesian-grid domain centred at the point (0,0,0). The initial parameters assigned to the gamma-packets are in the co-moving frame (CMF). Once a gamma-packet is created its parameters need to be converted from the CMF to the RF to be propagated through the grid. Every time a gamma-packet experiences a physical event we will convert their parameters back to the CMF to compute them. Then, the new ones will be converted again to the RF to continue its propagation. The energy shift experienced by the gamma-packets (E_{packet}) and the photons within ($E_{photons}$), when translated from the CMF to the RF can be defined as:

$$E_{rf} = E_{cmf}\ \gamma(1 + \boldsymbol{n_{cmf}} \cdot\ \boldsymbol{v}/c) \tag{2.23}$$

As seen in Mihalas and Mihalas (1984). On it, γ is the Lorentz factor, defined as:

$$\gamma = \frac{1}{\sqrt{1 + \frac{v^2}{c^2}}} \tag{2.24}$$

and $\boldsymbol{n_{cmf}}$ is the direction of propagation of the packet in the CMF. The direction $\mathbf{n}_{cmf}$ experiments an aberration in the RF:

$$n_{rf} = \frac{E_{cmf}}{E_{rf}}\Big(\boldsymbol{n_{cmf}} + \gamma(v/c)[1 + (\gamma\ \boldsymbol{n_{cmf}} \cdot\ \boldsymbol{v}/c)/(\gamma + 1)]\Big) \tag{2.25}$$

The opacity of the medium seen by the gamma-packet during its propagation in the RF will also be altered:

$$\chi_{rf} = \frac{E_{cmf}}{E_{rf}}\chi_{cmf} \tag{2.26}$$

To go back to CMF from RF we apply the following formulas:

$$E_{cmf} = E_{rf}\gamma(1 - \boldsymbol{n_{cmf}} \cdot\ \boldsymbol{v}/c) \tag{2.27}$$

$$n_{cmf} = \frac{E_{cmf}}{E_{rf}}\Big(\boldsymbol{n_{cmf}} - \gamma(v/c)[1 - (\gamma\ \boldsymbol{n_{cmf}} \cdot\ \boldsymbol{v}/c)/(\gamma + 1)]\Big) \tag{2.28}$$

$$\chi_{cmf} = \frac{E_{rf}}{E_{cmf}}\chi_{rf} \tag{2.29}$$

2.2.5 Propagation of the gamma-packets

Once a gamma-packet is created and its CMF changed to RF we start its propagation. The propagation can encounter three different events: physical interaction, cell boundary encounter or end of time step. The propagation will end once the gamma-packet is absorbed or escapes the domain. This process is done each time step for the created gamma-packets and the gamma-packets that still remain on the domain (old gamma-packets, initialized on past days, can be still on the domain because they have not escaped or been absorbed yet). The propagation of the gamma-packets is done one by one. The gamma-packet will move on a straight line unless an interaction changes its direction. Therefore, a simple way to know which interaction will happen before any other is to compute the distance to the three possible events: distance to termination of time step (d_{time}), distance to cell boundary (d_{bound}) and distance to next physical interaction (d_{int}) (for a visual representation see Figure 2.7). Then we proceed with the one with shorter distance. The distance is computed at the beginning of each propagation step for each gamma-packet.

The d_{time} is easily computed by assuming the gamma-packet is moving at the speed of light c. We can compute d_{time} if we know the time at the end of the

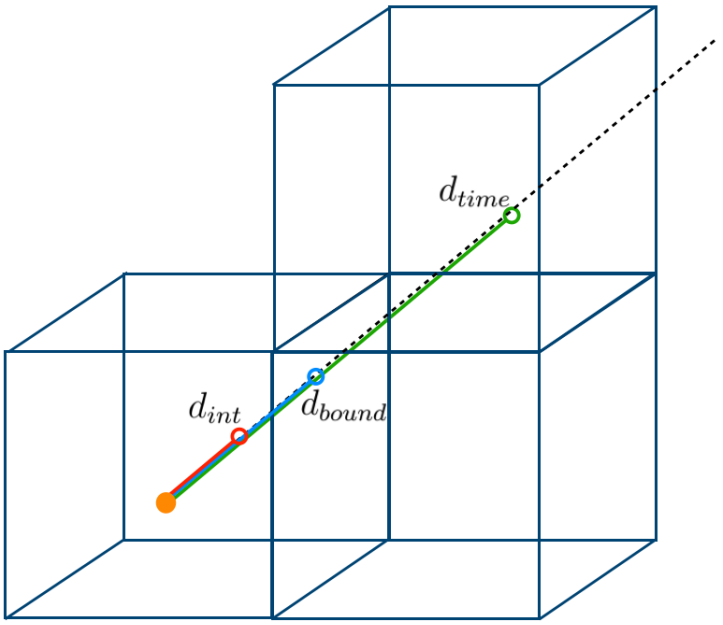

FIGURE 2.7: Three cells from the domain are shown where the gamma-packet is moving through. In this example scheme we show a case where the gamma-packet nearest event is a physical interaction.

time step, t_{S+1}, and the time of the gamma-packet, $t_{gpacket}$, as:

$$d_{time} = c \cdot (t_{S+1} - t_{gpacket}) \tag{2.30}$$

The d_{bound} is not as simple to compute, given the 3D symmetry of the simulation. Each cubic cell has 6 possible walls that the packet can cross. Two walls are the two planes perpendicular to the z-axis, we will call them 'top' and 'bottom'. Another two walls are the two planes perpendicular to y-axis, we will call them 'right' and 'left'. The other two walls are the two planes perpendicular to x-axis, we will call them 'front' and 'back'. See Figure 2.8 for a scheme of these walls. Given the direction in which the gamma-packet is travelling, we can discard 3 walls in which the gamma-packet will not cross. For the 3 selected walls, we compute the distance to each of them ($boundary_x$, $boundary_y$ and $boundary_z$) to know which one the gamma-packet will encounter first. The 3 boundaries are chosen taking in to account the value of the propagation angles θ an φ. The θ tell us if we select the 'top' or 'bottom' wall. For $0 < \theta < \pi/2$ the 'top' wall is chosen, for $-\pi/2 < \theta < 0$ the 'bottom' wall is chosen. The φ allow us to chose a combination of 'right' or 'left' and 'front' or back'. In the example in Figure 2.8, where $0 < \theta < \pi/2$, the top wall is chosen. Then as $\pi/2 < \varphi < \pi$, the 'right' wall and 'back' wall are chosen. Once the three possible boundary walls are selected, we compute the distance to each of them:

$$d_x = \frac{boundary_x - x}{cos\theta sin\phi} \tag{2.31}$$

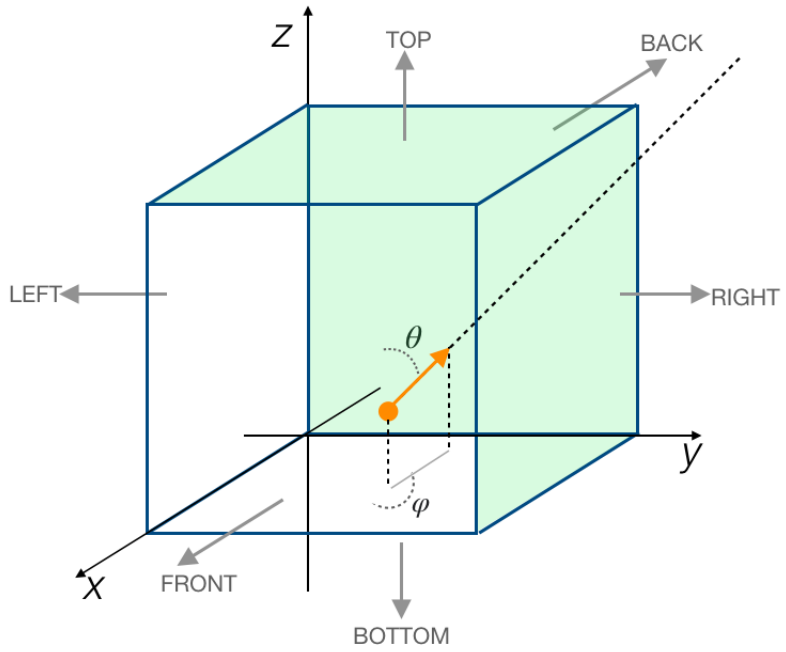

FIGURE 2.8: One cell is shown to visualize the method to compute the cell wall a gamma-packet will encounter first. In the example figure we show a case where $0 < \theta < \pi/2$ and $\pi/2 < \varphi < \pi$, therefore the three possible walls the gamma-packet will encounter are coloured in green. The distance to each of this walls is computed and the smallest is set as d_{bound}.

$$d_y = \frac{boundary_y - y}{sin\theta sin\phi} \tag{2.32}$$

$$d_z = \frac{boundary_z - z}{cos\theta} \tag{2.33}$$

where x, y, z are the position of the gamma-packet inside the cell. Then we select the smallest one as d_{bound}.

The distance of the packet to the next physical event, d_{int}, can be calculated from the optical depth of the medium, τ:

$$\tau = \int_0^s \chi ds \tag{2.34}$$

Where s is the mean free path or the distance to the next physical interaction, d_{int}, and χ is the opacity of the medium. The probability that a photon travels an amount of optical depth without interacting is $e^{-\tau}$. Monte Carlo techniques allow to express τ as a function of a random number z in the following way:

$$\tau = -lnz \tag{2.35}$$

And therefore, we find a probabilistic expression for the distance to the next physical interaction, d_{int} for the gamma-packet:

$$d_{int} = \frac{-lnz}{\chi_{total}} \tag{2.36}$$

The total opacity, χ_{total}, is defined by the sum of the opacities of the possible physical interactions as $\chi_{total} = \chi_{CS} + \chi_{PH} + \chi_{PP}$. Where χ_{CS} is the Compton scattering opacity and is computed as equation 2.42. χ_{PH} is the photoelectric absorption opacity and is computed as equation 2.39. χ_{PP} is the pair production opacity and is computed as equation 2.47.

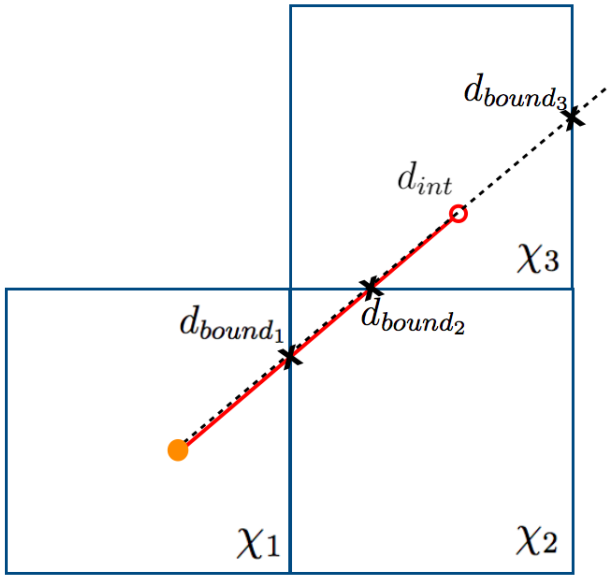

FIGURE 2.9: Scheme of d_{int} when a gamma-packet cross several cells with different opacities (χ) before having a physical interaction.

We can not compute directly d_{int} as in eq. 2.36 if the gamma-packet leaves the cell before having a physical interaction (d_{bound}<d_{int}) in situations in which the opacity of the first cell is different than the opacity of the new cell ($\chi_1 \neq \chi_2$). In this case we compute d_{int} in the following manner. We sample z to compute $-ln(z)$ from eq. 2.36. Then we compute the distance to the boundary in the first cell, d_{bound_1}. If $d_{bound_1} \cdot \chi_1 > -ln(z)$, it means the gamma-packet will suffer a physical interaction before crossing the cell and we can compute d_{int} as in eq. 2.36. In case $d_{bound_1} \cdot \chi_1 < -ln(z)$, it means the gamma-packet will cross the boundary before suffering a physical interaction. Therefore, we need to take into account the opacity of the next cell, χ_2. If we get the condition $d_{bound_1} \cdot \chi_1 + d_{bound_2} \cdot \chi_2 < -ln(z)$, the gamma-packet will cross again the boundary of the second cell before interacting. Now we consider the opacity of the third cell, χ_3. If in the third cell we get the condition $d_{bound_1} \cdot \chi_1 + d_{bound_2} \cdot \chi_2 + d_{bound_3} \cdot \chi_3 > -ln(z)$, it means the physical interaction will take place in the third cell before crossing its boundary. This process is illustrated in Figure 2.9.

2.2.6 Gamma-packet physical interactions

There are three main physical interactions that a gamma photon can encounter: photoelectric absorption, Compton scattering or pair production. These interactions change the characteristics of the gamma photon. They can get thermalized or get scattered to a new direction. The relative dominance of these interactions, see Figure 2.10, depend on the material these photons are travelling into and the energy they carry.

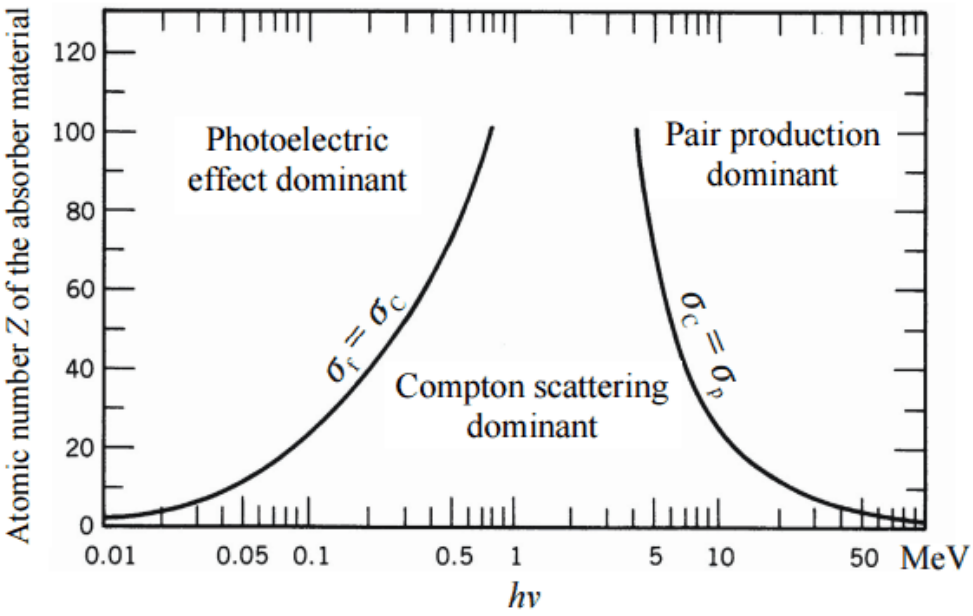

FIGURE 2.10: Dominance regions for the three main gamma-ray interaction processes. Source: The Atomic Nucleus by R. D. Evans 1955.

In our simulation, the probability of each interaction varies with the photon energy ($E_{photons}$) that the gamma-packet carries and the material composition of the cell. To chose which event of the three will happen of the three, we sample the probability ratios of each interaction given their opacities. For example, if we sample a random number z from 0 to 1 and the condition $z < \chi_{CS}/(\chi_{tot})$ is fulfilled then the gamma-packet experiences Compton scattering. If $z < \chi_{PP}/(\chi_{tot})$ it experiences pair production and if $z < \chi_{PH}/(\chi_{tot})$ it experiences photoelectric absorption.

Photoelectric absorption

A photon experiences photoelectric absorption, or bound free absorption, when it hits an electron bound into a shell of an atom that absorbs its energy. Then, if the energy of the photon is big enough for the bound state to be broken, the electron will be ejected from the material, which becomes ionized. The kinetic energy that the electron will carry after the absorption is:

$$E = h/\lambda - E_b \tag{2.37}$$

where h/λ is the energy of the incident photon and E_b is the binding energy of the electron to the atom.

Photoelectric effect is more probable in materials with high atomic number (Z), as they have higher density of electrons, and for gamma-ray photons with low energies (see Figure 2.10). The photoelectric opacity is dependent on the photon energy approximately as:

$$\chi_{ph} \simeq E^{-3} \tag{2.38}$$

In our code, we need to take into account the contribution of each element in the composition of the cell. We define the photoelectric opacity of the gamma-packet in the cell as:

$$\chi_{ph}(E) = \sum_{el} k_{el} \cdot \left(\frac{E}{100keV}\right)^{-\alpha} \cdot \frac{\rho_{cell}}{m_{el}} X_{el} \tag{2.39}$$

where E is the energy of the photons in the gamma-packet at CMF. k_{el} is the cross section value at 100keV as seen on Veigele (1973), α is ~ 3. The exact value of α for each element is computed by fitting the best α to the cross section values of Veigele (1973). The density of the cell from which we are computing the opacity is ρ_{cell}, m_{el} is the atomic mass of the element and X_{el} is the fraction of this element on the cell.

To determine if the gamma-packet experiences a photoelectric absorption we will sample a random number z from 0 to 1. If the following condition is fulfilled: $z < \chi_{ph}/\chi_{tot}$ then the packet experiences photoelectric absorption. In this situation the propagation of the packet is terminated, and the parameters of the packet are not longer saved, emulating the loss of the photon energy to an electron. We acknowledge that in a simulation where the optical spectra was simulated, the information of the packet would still be relevant. However, in an only gamma-ray simulation, as ours, the thermalized packet is no longer relevant.

Compton scattering

Compton scattering is an inelastic collision where a photon is scattered when it collides with an electron. The scattering produces a deflection angle θ to the trajectory of the photon, see Figure 2.11. The energy of the photon decreases as it transfers part of its energy to the electron:

$$E_f = \frac{E_i}{1 + \frac{E_i}{m_e c^2}(1 - cos(\theta))} \tag{2.40}$$

where E_i is the energy of the photon in the CMF before the scattering and $m_e c^2$ the energy of the electron at rest.

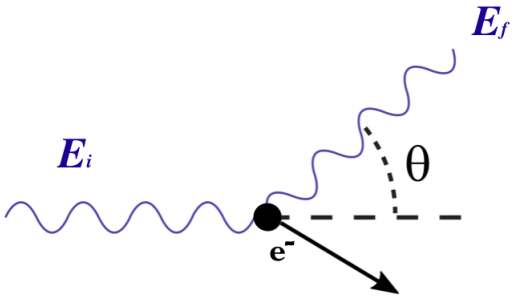

FIGURE 2.11: Sketch of Compton scattering process.

The differential cross section of Compton scattering is defined by the Klein-Nishina formula:

$$\frac{d\sigma}{d\Omega} = \frac{1}{2} r_e^2 \frac{E_f^2}{E_i^2} \left(\frac{E_i}{E_f} + \frac{E_f}{E_i} - sin^2(\theta) \right) \tag{2.41}$$

where r_e^2 is the electron radius. The opacity of Compton scattering is:

$$\chi_{cs} = \sigma_{KN} n_{e^-} \tag{2.42}$$

where n_{e^-} is the electron density of the cell and σ_{KN} is the total cross-section. The σ_{KN} is obtained by integrating equation 2.41 over the spatial angle Ω:

$$\sigma_{KN} = \frac{3}{4}\sigma_{Th} \left[\frac{1+x}{x^3} \left(\frac{2x(1+x)}{1+2x} - ln(1+2x) \right) + \right. \\ \left. + \frac{1}{2x} ln(1+2x) - \frac{1+3x}{(1+2x)^2} \right] \tag{2.43}$$

where σ_T is the Thomson cross section, $\sigma_T = (8\pi/3) r_0^2$, and $x = E/(m_{e^-} c^2)$.

The indivisible energy approach needs to compensate the energy that would be given to an electron in a real physical interaction. To do so, some gamma-packets will be converted to electron-packets which will terminate their propagation after the event, the other will continue as gamma-packets with reduced energy and a new trajectory due to the scattering angle. If we define the loss of energy as $f = E_i/E_f$, then from equation 2.40 we can express it as:

$$f = 1 + \frac{E_i}{m_e c^2} (1 - cos(\theta)) \tag{2.44}$$

Therefore, the energy is divided in the ratio (1 - f) (as seen in Lucy, 2005) and we can draw the condition to sample the gamma-packets that continue the propagation with $z < f$ and the ones that do not with $z > f$.

A challenging aspect of the computation of the final energy is the calculation of the scattering angle θ. For each incident energy there are multiple possible output angles. The area of probability varies with the incident energy. As seen in Figure 2.12, a high incident energy will lead to lower probability of possible scattering angle and for low incident energy the scattering angle value

spreads. To sample the values of θ given an incident energy, we need to obtain the cumulative distribution function $cdf_c(\theta)$ which is obtained integrating 2.41 over θ:

$$cdf_c(\theta) = \frac{r_0^2}{4x^2}\left[2\theta - \frac{2Barctan(-\sqrt{1+2x}tan(\theta/2}{\sqrt{(1+2x)^5}}\right] + \\ + \frac{r_0^2}{4x^2}\left[\frac{x^3 sin(\theta)}{(1+2x)(1+x(1-cos\theta))^2}\right] + \left[\frac{x(3x^3+11x^2+8x+2)sin(\theta)}{(1+2x)^2(1+x(1-cos\theta))}\right] \quad (2.45)$$

where $B = 11x^4 + 4x^3 - 12x^2 - 10x - 2$ and $x{=}E/(m_{e^-}c^2)$, as seen in Adámek and Bursa (2014).

As $cdf_c(\theta)$ will take values from 0 to 1, we can sample a random number z and get the value of θ for a photon energy E_i. Equation 2.45 needs to be solved numerically and we use bisection method to draw the results. A test of this method is seen in Figure 2.12 that shows sampled θ results for $E_i{=}$ 0.01, 0.05 , 0.2, 0.5, 1 and 3 MeV.

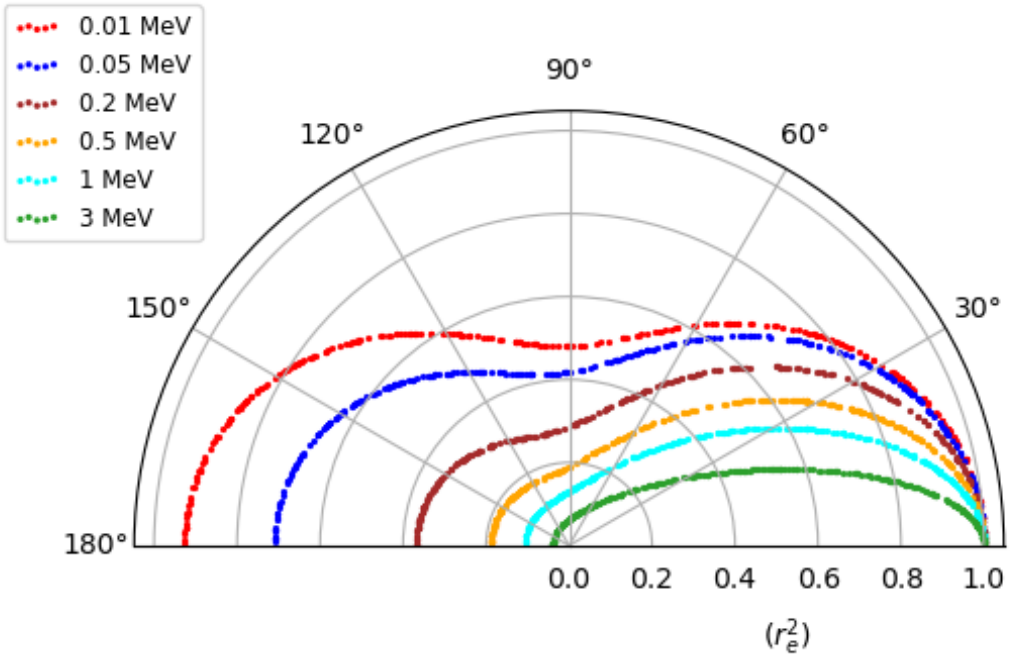

FIGURE 2.12: Polar plot that shows 500 realizations scattering angles θ for each different incident photon energies: 0.01, 0.05, 0.2, 0.5, 1 and 3 MeV. The results have been computed by solving numerically equation 2.45. The σ_{KN} values are in units of r_e^2 and have been computed by using equation 2.43.

Once the scattering angle is found, the new direction angles (θ, φ) of the gamma-packet are $\boldsymbol{n_i} \cdot \boldsymbol{n_f} = \cos(\theta)$ and φ is randomly sampled from 0 to 2π.

Finally, once the final parameters of the gamma-packet in the CMF are computed, to end the Compton scattering step, we will convert the packet parameters to the RF and continue its propagation.

Pair production

When a photon with high energy travels through matter it can experience pair production. Pair production is a phenomenon in which the photon is converted into an electron and, its antiparticle, positron. This can only be possible under two conditions. First, the energy of the photon is larger than the rest energy of the two particles. Second, the photon travels through matter. The first condition, $E_\gamma \geq 1.022$ MeV, needs to be fulfilled in order to accomplish energy conservation. If the energy of the incident photon is higher than this threshold, the remaining energy will be converted into kinetic energy for the pair of particles. The second condition aims for momentum conservation. The momentum of the photon is given to the atom in whose its electric field the photon is travelling. Pair production cannot happen into empty space or it would violate momentum conservation.

This phenomenon is dominant at high energies (see Figure 2.10) and for domains with high heavy (high Z) atoms. We define the pair production opacity from the cross section defined in Ambwani and Sutherland (1988):

$$\sigma = \begin{cases} 0.10063(E - 1.022)Z^2 \cdot 10^{-27}\text{cm}^2 & 1.022 < E < 1.5\text{MeV} \\ [0.0481 + 0.301(E - 1.5)]Z^2 \cdot 10^{-27}\text{cm}^2 & E > 1.5\text{MeV} \end{cases} \tag{2.46}$$

where Z is the atomic number of each element and E the energy of the photon in the CMF. The factor 0.10063 is presented as 1.0063 in Ambwani and Sutherland (1988) and later corrected in Swartz et al. (1995). From the cross section we can define the opacity as:

$$\chi_{pp} = \sum \sigma \cdot \left(\frac{\rho_{cell} \cdot X_{el}}{m_{el}} \right) \tag{2.47}$$

where ρ_{cell} is density of the cell in which we are computing the density, m_{el} is the atomic mass of element and X_{el} its mass fraction in the cell.

We need to consider that for some pair production events in situ annihilation will occur. This creates two photons with an energy of 0.511 MeV emitted isotropically. Therefore, the gamma-packets that experience pair production have two fates. First, elimination due to pair production. Second, continue their propagation with a new energy on its photons (equal to 0.511 MeV) and with a new random sampled direction. The probability of in situ annihilation is defined as $z < 2 \cdot 0.511/E$, if not, the gamma-packet continues its propagation.

2.2.7 Escaping packets

When a gamma-packet crosses a boundary of a cell into another cell that does not belong to the domain (see Figure 2.2 where there are domain cells and no domain cells), we consider the gamma-packet has escaped the ejecta. When this happens, we store its parameters and end its propagation. At the end of the time step we save a file with the gamma-packets that have exited the domain during that period. With the parameters of the gamma-packets we compute the amount of photons each gamma-packet has. Then we build the spectra with the number of photons in each energy bin of 1 keV. From the number of photons (γ) we can compute the Flux as:

$$Flux = \frac{\gamma}{\Omega \cdot \Delta t \cdot \Delta E} \tag{2.48}$$

with units of $\gamma\ cm^{-2}\ s^{-1}\ keV^{-1}$, where Ω is the solid angle, Δt is the length of the time step and ΔE is the energy bin of 1 keV. If we want to compute the Flux created by the photons that exit the domain from all directions, then the solid angle is $\Omega = 4\pi d^2$, where d is the distance to the simulated supernova.

2.3 Testing the code

We have explained how the code operates in Section 2.2 and the theory behind it in Section 2.1. Now we proceed to make some tests to verify its performance. In past sections we have already tested small particular operations of the code. Such like the grid creation, the radioactive decay or other features (see Section 2.2). This Section aims to show the operation of the code on its totality to prove its able to simulate the physical features of a SN Ia explosion correctly.

2.3.1 Formation of lines

The first two tests we show are to study the creation of gamma-packets but without experiencing any physical interaction. The goal is to see the formation and behaviour of the lines in a static sphere first and, later, in a sphere with homologous expansion. The domain for both experiments is a sphere of constant density with a radius of 10^6 km that is made of $1M_\odot$ of pure ^{56}Ni. For both experiments we show the spectrum for the 15th day and 70th day of the simulation. The 15th day is chosen to show the spectrum at early days before the optical maximum of the explosion. The 70th day is chosen to observe the good functioning of the code for later time steps.

In the first test (T1) the domain remains static, it does not experience any expansion of any kind. We show the spectrum for the 15th day of simulation and the 70th day on Figure 2.13a and 2.13b, respectively. In Figure 2.13a we can see that the most prominents lines are 0.158 MeV, 0.270 MeV, 0.480 MeV, 0.750 MeV, 0.812 MeV and 1.562 MeV. These lines are created from the decay

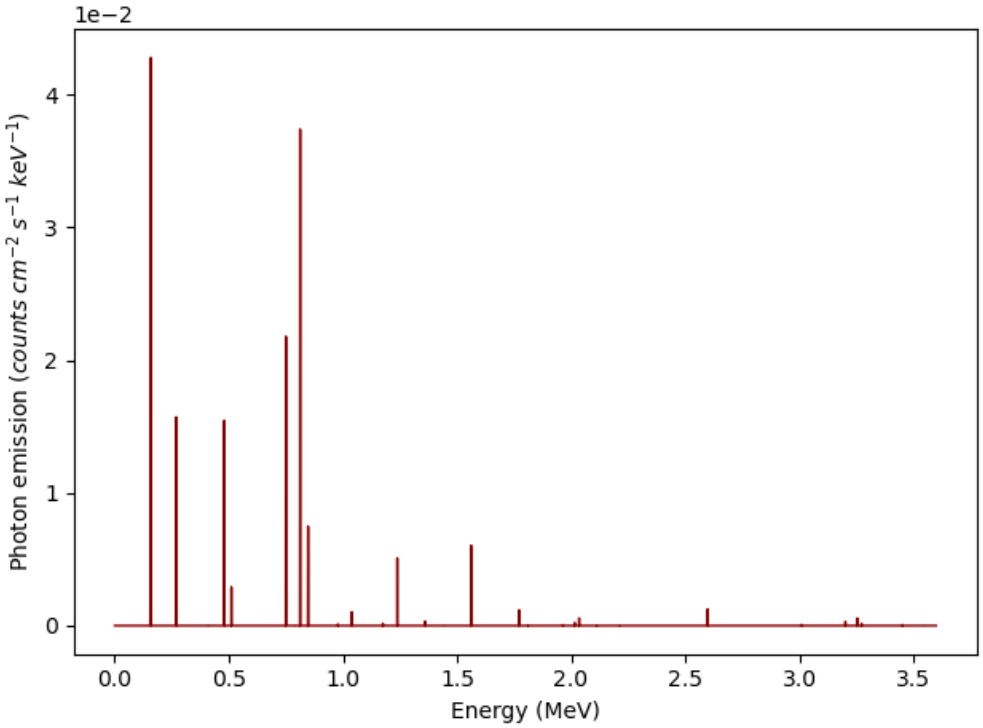

(A)

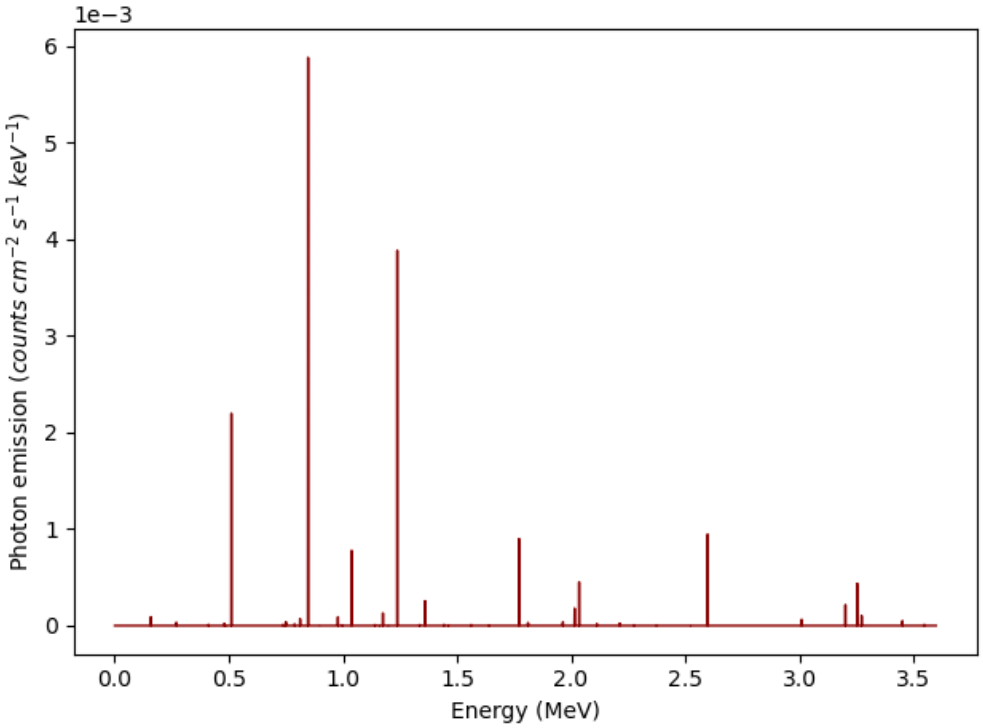

(B)

FIGURE 2.13: (A) Spectrum from day 15 of T1. Represent model without expansion of a sphere of constant density with a radius of 10^6 km that is made of 1 $M_\odot$ of pure ^{56}Ni. (B) As for (A) but at day 70.

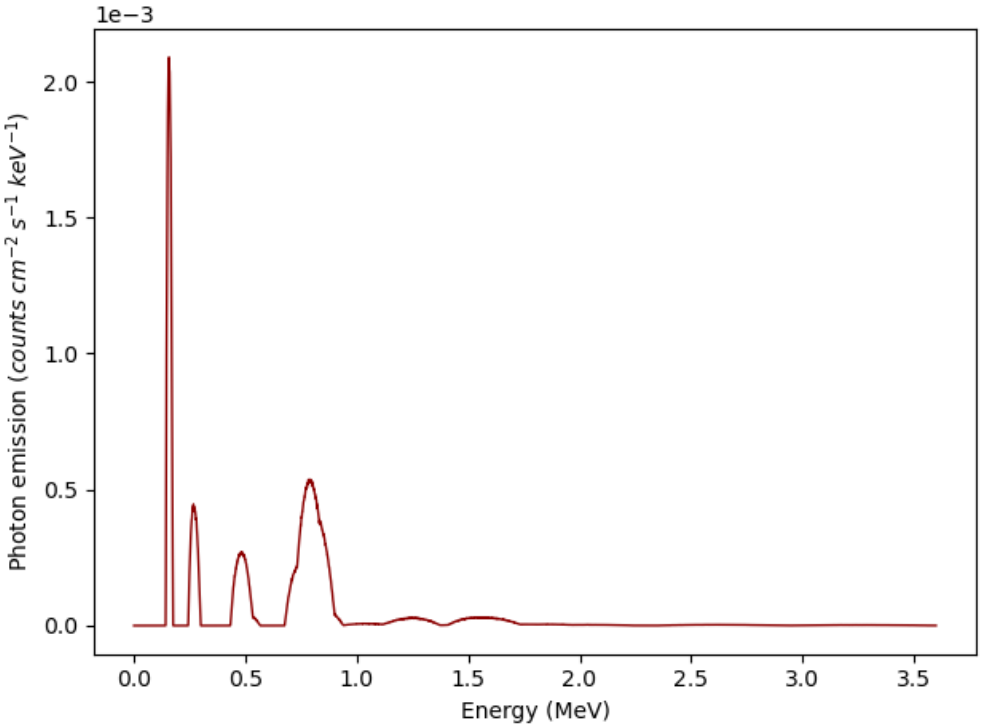

(A)

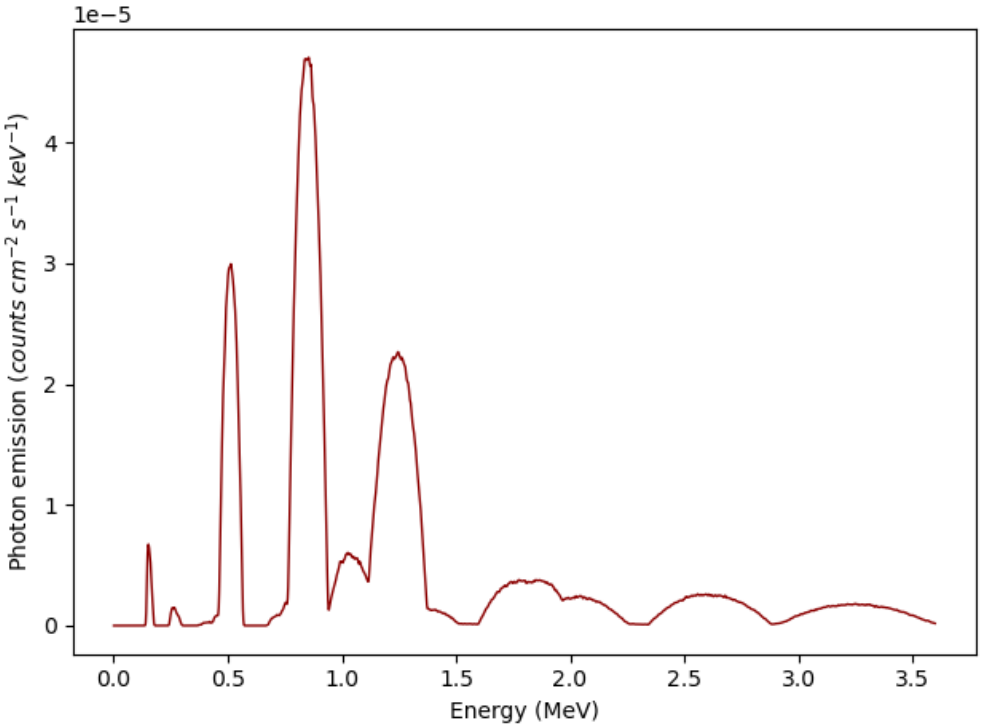

(B)

FIGURE 2.14: (A) Spectrum from day 15 of T2. Represents an homologous expansion of a sphere with initial constant density, initial radius of 10^6 km that is made of 1 $M_\odot$ of pure ^{56}Ni. (B) As for (A) but at day 70.

of ^{56}Ni pellets, which dominates at 15th day of the simulation. The ratios of the lines are consistent with the probabilities shown on table 2.2.3. We also see the rising of ^{56}Co lines. Although the mean decay lifetime of ^{56}Co is 111.7 days, there are already some early decays that may happen around day 15, see Figure 2.5. On Figure 2.13b there is a visible decrease of flux due to the lower decay rate on later days of the explosion. In comparison to 15th day, now the spectra is dominated by ^{56}Co lines such as 0.847 MeV, 1.238 MeV or 2.598 MeV. The 0.511 MeV is shown without the positronium effect. We notice a modest contribution of residual ^{56}Ni lines that are due to the later decays, see Figure 2.5.

The second test (T2) simulates a sphere that experiences homologous expansion. It has an initial radius of 10^6 km that is made of 1 $M_\odot$ of pure ^{56}Ni (homogeneously distributed). The last layer is expanding at $0.1c$ (with c as speed of light). The goal of T2 is to see the behaviour of T1 under relativistic conditions. For day 15 and day 70 the broadening of the lines due to Doppler effect is visible because of the expansion of the ejecta at relativistic velocities. At 15th day the main lines of ^{56}Ni are dominant and broadened, this caused the merging of line 0.750 MeV and 0.812 MeV in a broad asymmetric pike. We can observe larger broadening for higher energies. T2 displays lower flux than T1 because the rate of photons is dispersed around the line value. The lower flux is both seen at day 15 and 70. The spectra of the 70th day is, as expected, dominated by ^{56}Co decays. In it the merging of lines is even more noticeable, not allowing to differentiate the higher energy lines in the spectra.

2.3.2 Comparison with 1D code

We proceed to simulate two test models (T3 and T4) that will experience in its totality the physical features described in Section 2.2.6. Both consist of a sphere with a total mass of 1 $M_\odot$ (homogeneously distributed) and initial radius of 10^6 km. The most external layer expands at $0.1c$. T3 is made solely of ^{56}Ni, since is the main radioactive element that fuels SNe Ia. T4 is made of 0.42 $M_\odot$ of ^{56}Ni, 0.29 $M_\odot$ of C (Z=6) and Si (Z=14). The ^{56}Ni is placed at the core of sphere until a 3/4 of its total radius. The Si and C are mixed in an external layer that goes from the 3/4 of the radius to the total. We aim to see the features in the spectra due to different opacities. The mix of C and Si are selected to represent typical not-burned and semi-burned elements from the explosion.

In order to verify the code, we have compared the output spectra of these two test with a 1-dimensional code that synthesizes the gamma-ray transfer in SN Ia described in Gomez-Gomar et al. (1998), Milne et al. (2004) and Isern et al. (2008). This 1D code is also based on Monte Carlo techniques and it is based in the work of Pozdnyakov et al. (1983) and Ambwani and Sutherland (1988). The treatment of the test particles in this code is based on the photon packet approach, instead on the indivisible energy packet approach that we have adopted from Lucy (2005). The comparison of this 1D code with our 3D can be done when we build symmetric models as the ones we proceed to test.

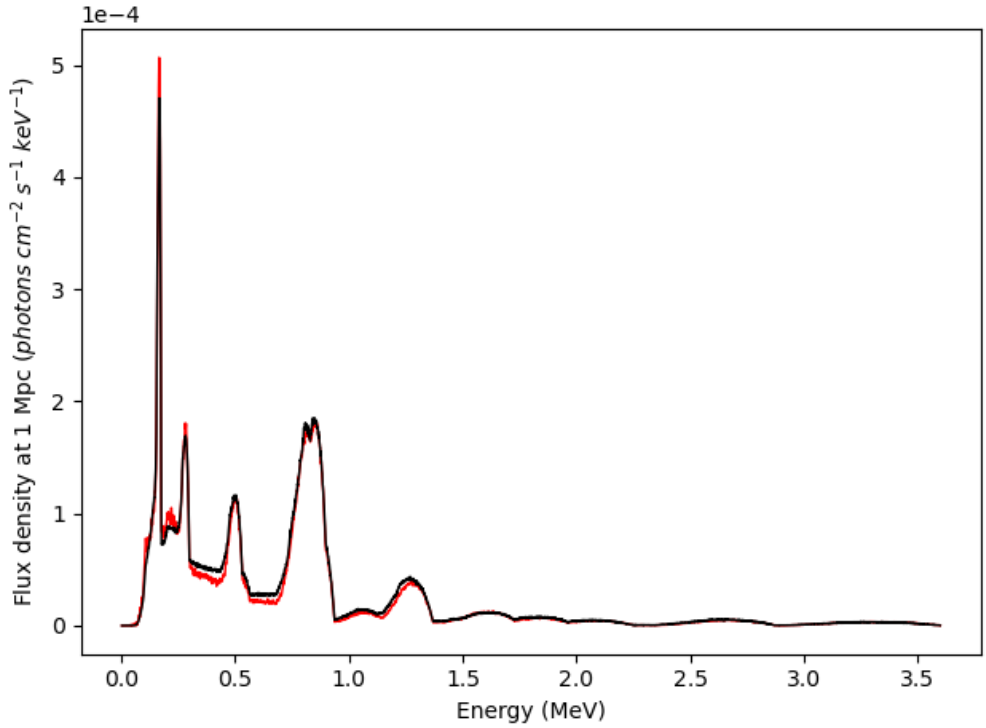

(A)

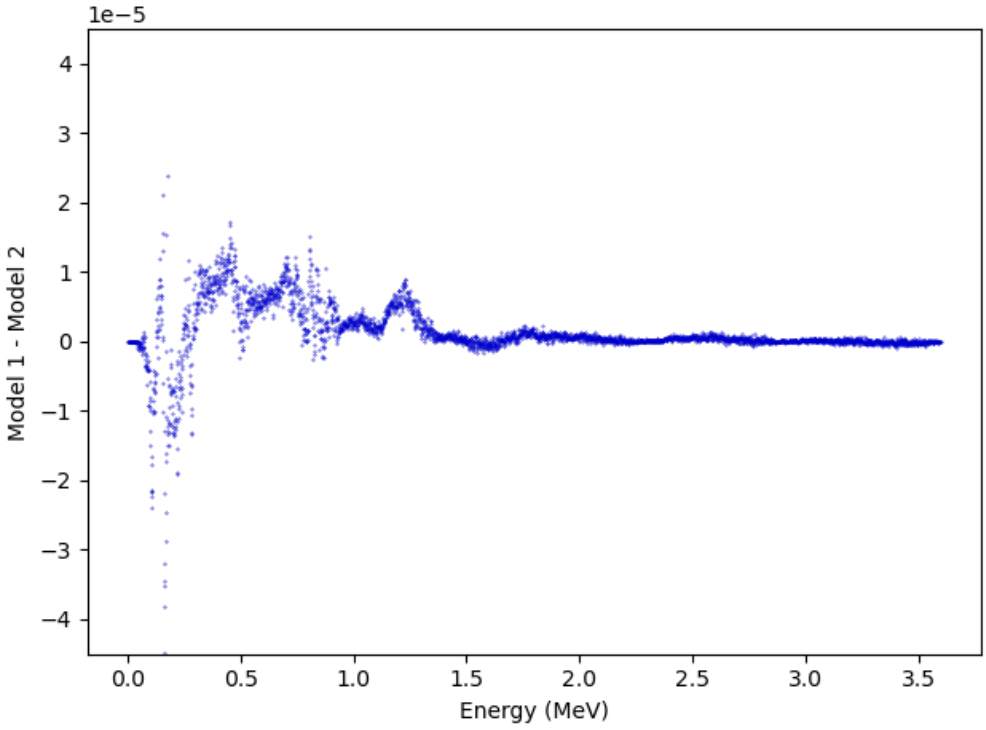

(B)

FIGURE 2.15: (A) Spectrum from day 20 of T3. In red we show the spectrum made with our 3D simulation and in black the spectrum made with 1D simulation by Gomez-Gomar et al. (1998) (B) Subtraction of red spectrum (Model 2) to black spectrum (Model 1).

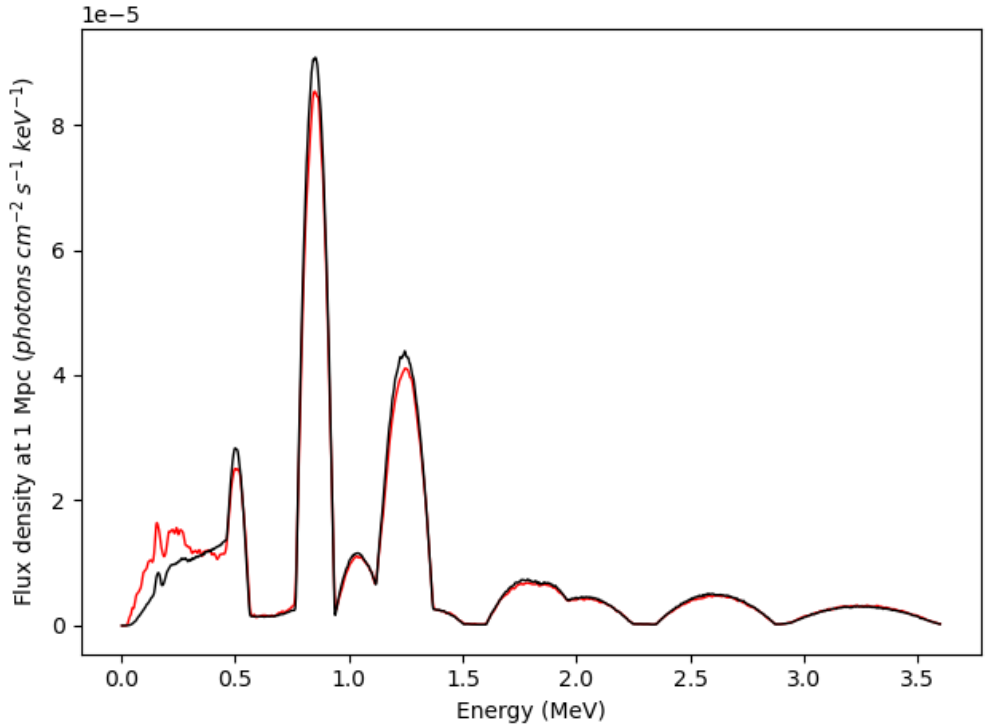

(A)

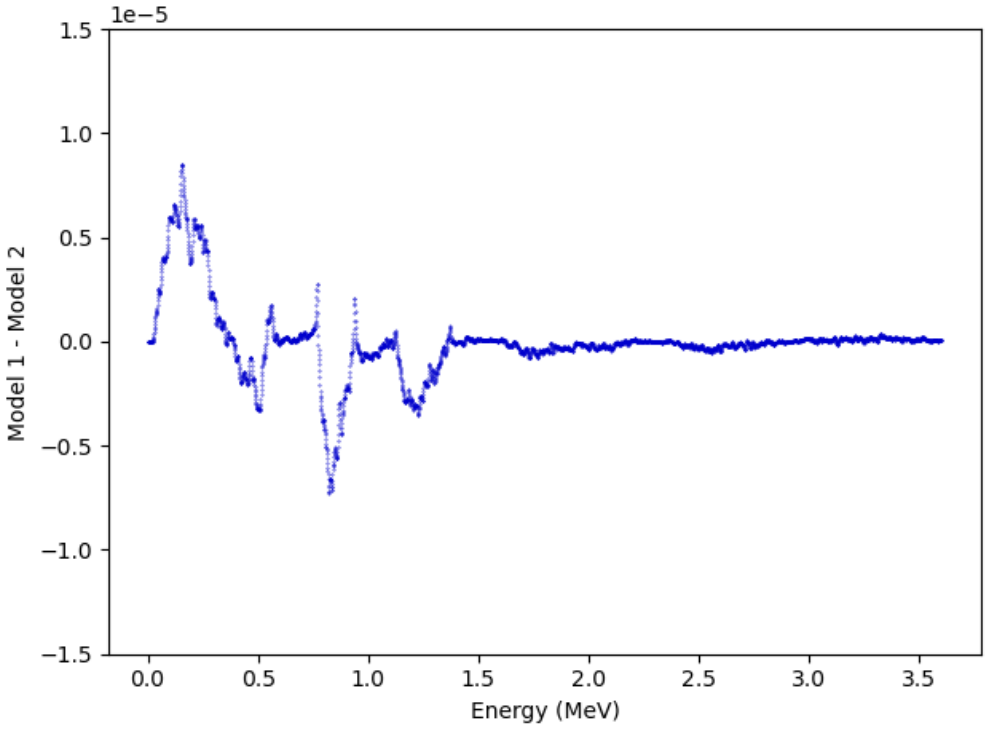

(B)

FIGURE 2.16: (A) Spectrum from day 70 of T3. In red we show the spectrum made with our 3D simulation and in black the spectrum made with 1D simulation by Gomez-Gomar et al. (1998) (B) Subtraction of red spectrum (Model 2) to black spectrum (Model 1).

For T3, where a pure ^{56}Ni sphere is modelled, we show the output spectrum of the 20th and 70th day. In Figure 2.15a, in red, we show the spectra from our 3D code for the 20th day and, in black, the spectrum from the 1D code. In the spectrum we observe the effect of physical interactions that the gamma-packets experience. Besides the broadening due to Doppler effect, we can see that Compton scattering broads the lines towards the left from the center of them. This is due to energy loss of the photons inside the gamma-packets. The energy loss creates a continuum in the spectrum that can be easily seen for lower energies than ∼1 MeV. Photoelectric absorption effect is also identified in the spectra below ∼0.1 MeV, where the continuum from the scattered photons suddenly drops. This is because photoelectric absorption becomes dominant at such energy ranges. Both codes seem to perform almost identical. In order to prove the similarity we have subtracted the 3D model to the 1D model (Model 1 and 2 respectively as seen on Figure 2.15b). The subtraction mean value is $1.38{\cdot}10^{-6}$ $\gamma\ cm^{-2}\ s^{-1}\ keV^{-1}$, with an standard deviation of $4.00{\cdot}10^{-6}$, confirming the similarity of both models. The spectrum of the 70th day is shown in Figure 2.16a and the substraction of both models on Figure 2.16b. The spectrum shows that Compton scattering is no longer observable. This is because the density of the domain has dropped, due to its expansion, and the opacity is too low for the scattering to take place. As the 1D code considered the formation of positronium from 0.511 MeV line, we have adapted our code to the formation too to be able to compare them. As we can see, the formation of positronium creates a continuum for energies lower than 0.511 MeV. Overall, the two models are very similar. The subtraction of them have a mean value of $-1.65{\cdot}10^{-8}$ $\gamma\ cm^{-2}\ s^{-1}\ keV^{-1}$ and a standard deviation of $1.79{\cdot}10^{-6}$. The slightly differences observed on the flux of some lines are due to using different mean lifetime values. The version of 1D code used in this test defines the mean lifetime of ^{56}Ni as 8.5 days and ^{56}Co as 113.7 days (as in Browne et al., 1986). Our 3D sets the mean lifetime of ^{56}Ni as 8.8 days and ^{56}Co as 111.7 days (as in Lederer and Shirley, 1978). When these mean lifetimes are set the same the lines do not show any flux change. We show this test to acknowledge the differences that can be seen at late times when values from different literature are selected.

For T4, where a sphere with ^{56}Ni core is surrounded by a C/Si layer, we show the output spectrum of the 20th and 70th day. In Figure 2.17a, in red, we show the spectrum from our 3D code for the 20th day and, in black, the spectrum from the 1D code. Same for Figure 2.18a but for the 70th day. T4 has lower flux compared to T3 because it has lower quantities of ^{56} Ni. T4 displays a continuum in the 20th day due to Compton scattering, as in T3. The external layer of T4 has a lower opacity than T3 because C and Si have lower Z than ^{56}Ni. Due to that the continuum below ∼0.1 MeV reaches lower energies in the spectrum. The continuum effect in T4, as for T3, disappear at the 70th day due to very low opacity of the ejecta. Both spectra have very similar values to the 1D code ones, see Figure 2.17a and Figure 2.18a. For the 20th day the mean subtraction value is $7.21{\cdot}10^{-7}$ with standard deviation of $3.10{\cdot}10^{-6}$. For the 70th day the mean subtraction value is $6.79{\cdot}10^{-8}$ with standard deviation of $8.84{\cdot}10^{-7}$.

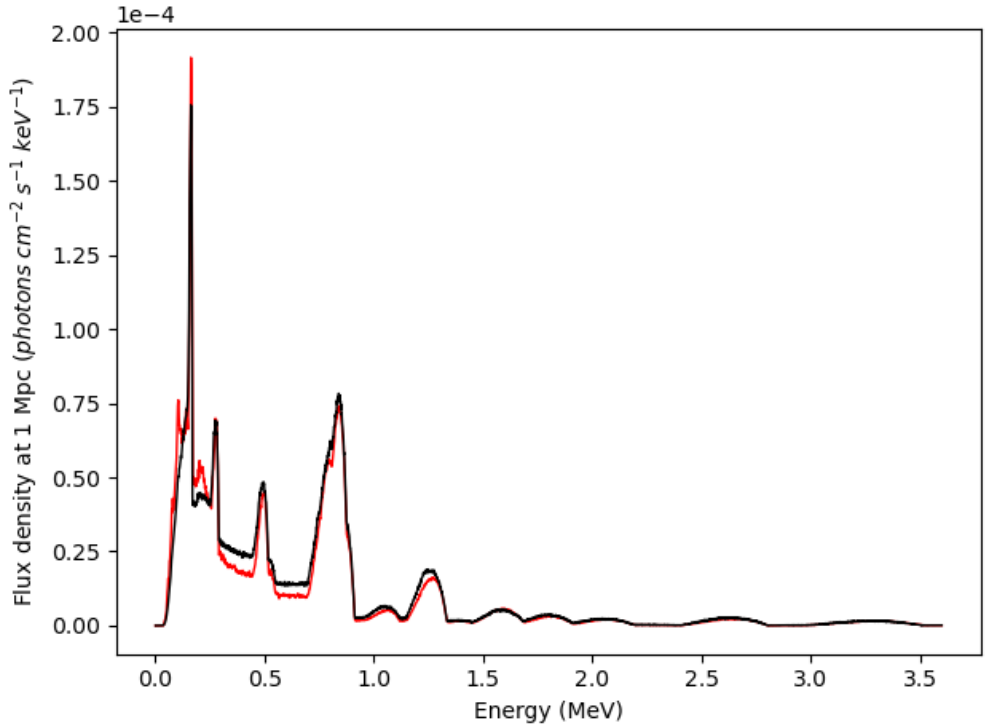

(A)

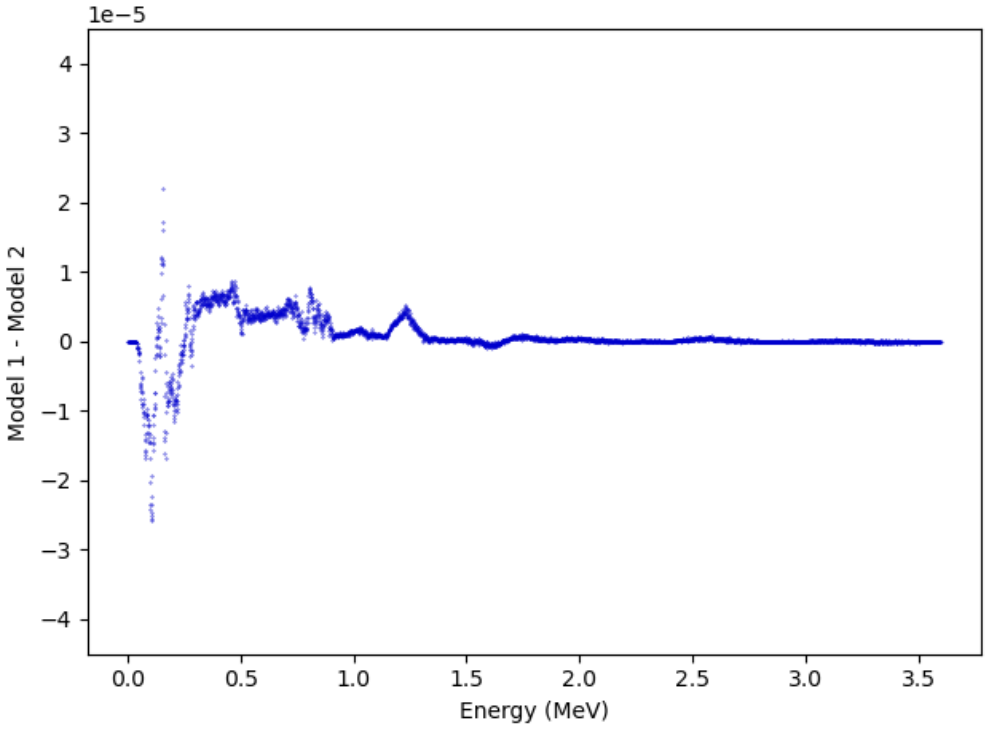

(B)

FIGURE 2.17: (A) Spectrum from day 20 of T4. In red we show the spectrum made with our 3D simulation and in black the spectrum made with 1D simulation by Gomez-Gomar et al. (1998) (B) Subtraction of red spectrum (Model 2) to black spectrum (Model 1).

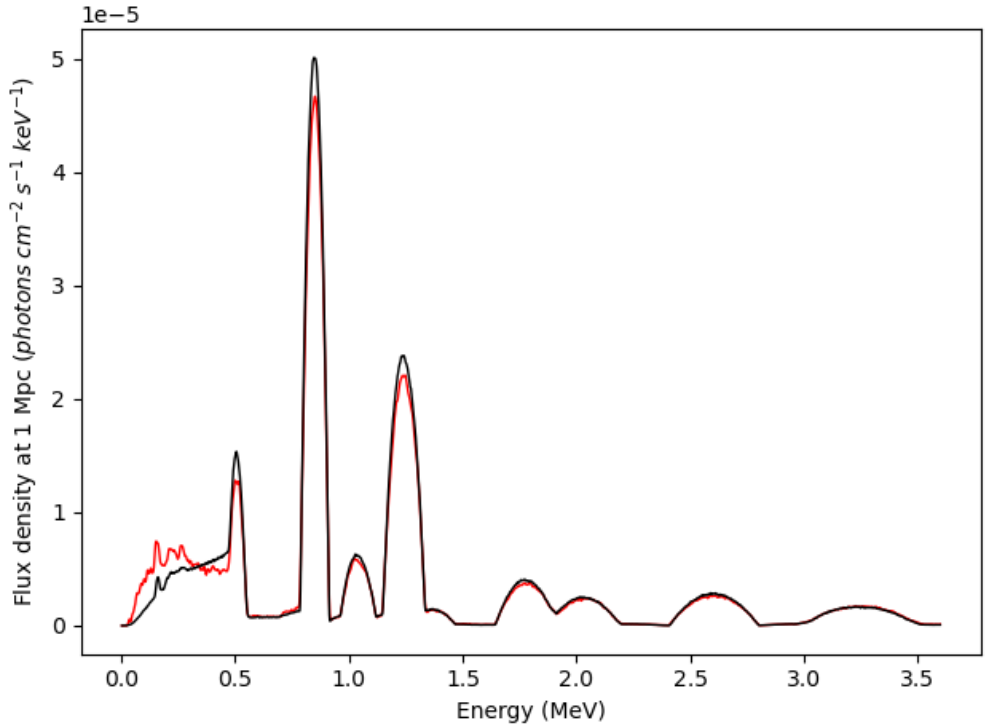

(A)

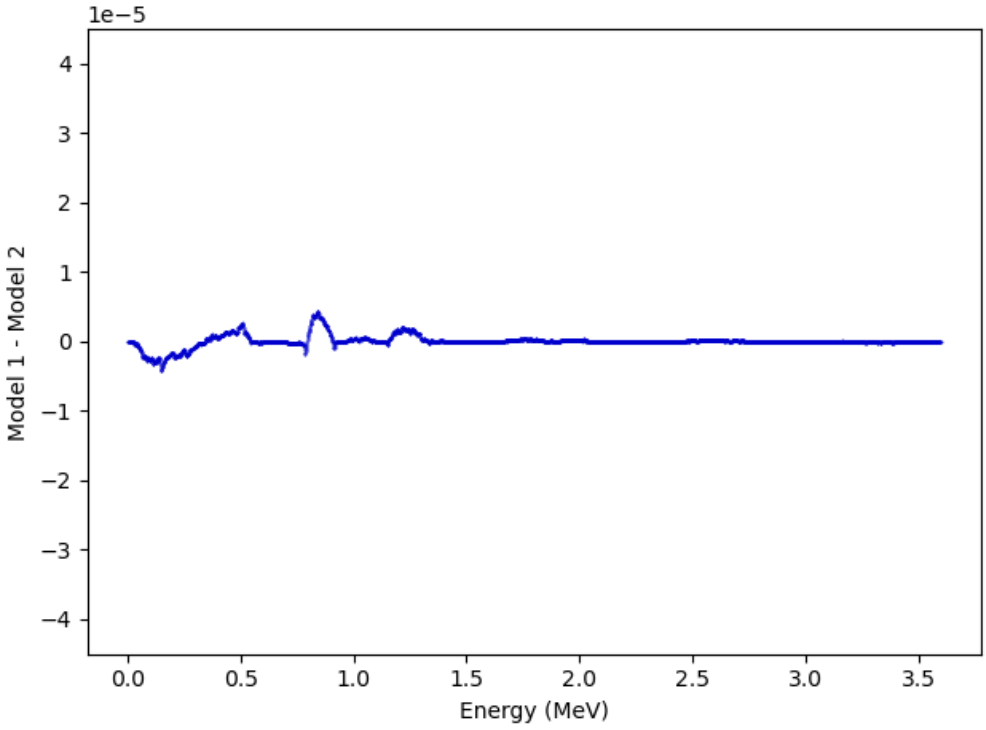

(B)

FIGURE 2.18: (A) Spectrum from day 70 of T4. In red we show the spectrum made with our 3D simulation and in black the spectrum made with 1D simulation by Gomez-Gomar et al. (1998) (B) Subtraction of red spectrum (Model 2) to black spectrum (Model 1).

2.3.3 Parallelization

The 3D code of this work have been parallelized due to high time demanding jobs. As mentioned in Section 2.1, Monte Carlo's techniques make the output results subject to statistical noise. This disadvantage can be easily overcome by sampling bigger size of gamma-packets. To do so, we divide the total energy of the simulation in a bigger amount of gamma packets. This results in gamma-packets with a smaller amount of packet energy. To do so, we simply create more decaying pellets at the beginning of the simulation. The increment of test particles turns out in simulations that take too much time to end. However, the total amount of gamma-packets can be divided on different processors. This is due that gamma-packets can be treated as a pool of test particles from the same experiment. By doing so we parallelize the simulation and speed up the computation. This is possible due to the bosonic character of the photons. They do not interact between each other, so we do not need to update the parameters during simulation. Therefore, the simulation can be divided in different processors that work independently.

We have tested different kind of parallelizations during the project. In the first one we tried, we just parallelized the part of the simulation where the gamma-packets propagate (green loop in Figure 2.1). At the beginning of this project, the approach of gamma-packet creation was slightly different from the one shown on Figure 2.1. Initially, we tried to first create all the gamma-packets from all the pellets that would decay on a given time step, once the pool was created this allowed to divide the pool in the amount of processors we parallelized the propagation loop with. This required a constant change to one processors to multiple ones every time the propagation of all the gamma-packets in a same time step was done and another time step began. This process was first achieved using Python library joblib, which has the tool Parallel and allows to parallelize a chosen function between a given number of processors. This initial approach was useful for small desk jobs that did not require a lot of processors. As the test simulations increased in complexity the computations needed more processors and so we used a computer cluster. With the use of a computer cluster we emulated the same parallelization using a Message Passing Interface (MPI). These two similar approaches both used the initial parameters defined at the beginning of the simulation and were shared to all the parallel jobs.

We found an easier way to parallelize the whole computation that avoided the slow down of going through one processor to multiple ones in a same test. We simply parallelized the whole simulation and not just one part of it. This is possible because our simulations just take into account the gamma-ray part of the supernova explosion, we do not need to update the parameters due to thermalization of gamma-packets. Therefore, the multiple processes don't need to exchange information during the whole simulation. The only parameters updated for each time step due to the expansion of the domain are the same for each of the processes and do not depend on the random behaviour of the gamma-packets during their propagation. Therefore, we simulate a desired

amount of processes were each has the same domain and initial parameters. More importantly, they all have the same amount of initial pellets. So the total amount of pellets used in the simulation would be the sum of the initial pellets of each process. The total energy of each gamma-packet in each process will be divided by the amount of processes in which we divide the experiment. That is to say 2.3 becomes $E_{packet} = E_{packet}/N_{process}$. A test of the same simulation using different amount of processors is shown in figure 2.19 to visualize the speedup factor of this method.

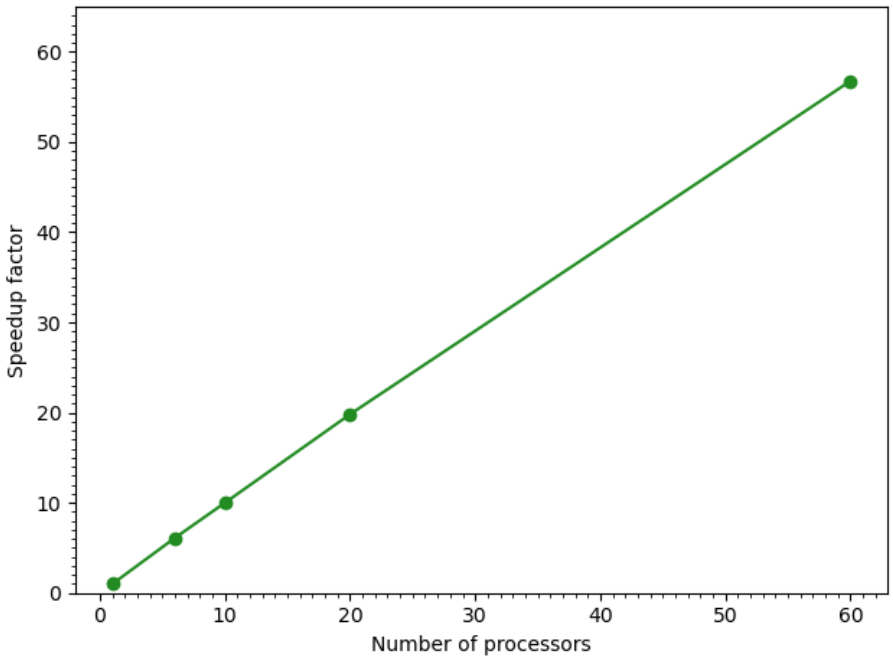

FIGURE 2.19: Speedup factor of our code normalized to 1 processor. The test is done for 1, 6, 10, 20 and 60 processors.

Chapter 3

Application to explosion models

The progenitor system and explosion mechanism of Type Ia supernovae still remain a mystery. As the number of detected SN Ia has been increasing these last years, several subtypes have been discovered. The existence of these subtypes launches a discussion about the uniqueness of the progenitor system and explosion mechanism of the event. Recent studies propose that these subtypes may be explained by SN Ia possibly having more than one kind of progenitor scenarios and explosion mechanisms (Hillebrandt and Niemeyer, 2000; Maoz et al., 2014; Isern et al., 2021). The study of gamma-ray emission of these events few days after the explosion could provide the necessary information to unravel their origin. The gamma radiation coming from SN Ia comes from the decay chain ^{56}Ni $\rightarrow$ ^{56}Co $\rightarrow$ ^{56}Fe. This decay chain releases high energy gamma-ray photons that heat the debris and power the optical and infrared light curves of the event (see Colgate and McKee, 1969). The synthesis of ^{56}Ni is made by the rapid C/O burning. The decay of ^{56}Ni has a mean lifetime of $\sim$8.8 days, while the decay of ^{56}Co has a mean lifetime of $\sim$111 days. The lines created by these decays can be detected when the ejecta is transparent enough for the photons to escape the supernova domain without being thermalized. The intensity and broadening of gamma-ray lines can give clues about the kinematics and morphology of the explosion (Burrows and The, 1990; Gomez-Gomar et al., 1998; Jean et al., 1999; Milne et al., 2004; Isern et al., 2008). ^{56}Co lines are usually detected after the maximum of the optical light curve and the following months. On the other hand, ^{56}Ni gamma-ray lines are not so easy to detect because the supernova ejecta may not be transparent enough by the time in which the photons are created or because the detection of the supernova is made at later days. However, if there are radioactive elements in the outer layers, the photons from ^{56}Ni decay may be able to escape the domain before being thermalized and, if they are detected, give crucial information about the origin of the explosion. The early detection of these events is studied later in this work in Chapter 4.

In this chapter we explore the synthetic observables obtained from different morphologies of explosion and different isotopic composition. They have been obtained using the gamma-ray transfer code explained in the previous chapter. We study the change of luminosity and spectral lines obtained with different placements of ^{56}Ni in the SN Ia models. To do so, we analyse the evolution of the gamma-ray light curve and spectrum along all days of the simulation, focusing on the early stages of the models. The simulations are 3-dimensional and some

of them have asymmetries to resemble real explosions. The introduction of asymmetries allows us to explore the changes of these observables when looking from different lines of sight.

We present three experiments of simulated models that represent different explosion mechanisms. The first experiment shows two spherical toy models with different amounts of ^{56}Ni in their core (Section 3.1). The second experiment is also a spherical toy model but with ^{56}Ni placed in multiple ignition points (Section 3.2). The last experiment shows multiple models based on a spherical delayed detonation (DDT) model but with an attached asymmetry in the outer layers (Section 3.3). All the models are simulated at 3.5 Mpc to mimic the distance of SN 2014J.

3.1 Variable ^{56}Ni mass toy models

In this section we present two toy models and compare them. We have build two simple toy models, instead of using an input model from the outcome of an hydrodynamic code. Toy models are based on some physically motivated assumption. Although their initial composition and kinematics lack complexity, they are useful for testing purposes. The assumptions are good enough to study the physical changes in the synthetic observables due to different compositions.

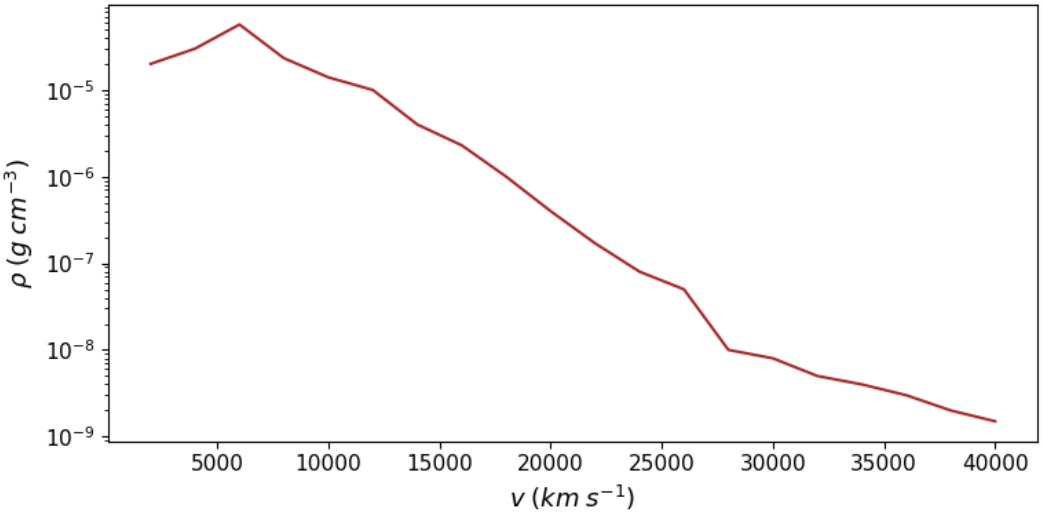

FIGURE 3.1: Density profile of TM1 and TM2 models in units of g cm^{-3} versus the expansion velocity in units of km s^{-1} along all the layers of the model.

Both models are build as a 3D sphere made of 268,096 cubic cells with three sub-domains each one (as it was seen in Chapter 2). The first subdomain is a spherical core made of ^{56}Ni. The second subdomain is a layer of Si surrounding the core. The third subdomain is an outer layer made of C and O surrounding the Si layer. Each model has different amounts of ^{56}Ni to study the variability of the synthetic observables in the gamma-ray energy range. The first model

(named TM1) has ∼0.31 $M_\odot$ of ^{56}Ni, ∼0.83 $M_\odot$ of Si and ∼0.23 $M_\odot$ of C/O (half carbon and oxygen mix). The second model (named TM2) has ∼0.54 $M_\odot$ of ^{56}Ni, ∼0.6 $M_\odot$ of Si and ∼0.23 $M_\odot$ of C/O. The total mass of each model is ∼1.36 $M_\odot$, to simulate that the WD reaches the Chandrasekhar limit.

The composition of TM1 and TM2 is chosen to simulate in a simple manner the elements found in SN Ia (see Filippenko, 1997). We have the main radioactive element from the explosion (^{56}Ni), an intermediate-mass element (Si) and unburnt elements (C and O). The placement of ^{56}Ni in the center of the sphere is a common practice in SN Ia simulations based in the theory that the ignition of the explosion starts in the center of the WD (see Hillebrandt and Niemeyer, 2000). The amount of ^{56}Ni for each model is chosen taking into account that studies suggest 0.3 to 0.9 $M_\odot$ of ^{56}Ni for a normal SN Ia (Stritzinger et al., 2006).

The initial radius of the sphere is $1{\cdot}10^9$ km. The velocity of expansion of the outer layer is $\sim 4{\cdot}10^4$ km s^{-1}. These parameters are taken from the DDT1p4 model from E.Bravo (a previous version to the one tailored to fit SN 2014J in the study Isern et al., 2016). The density profile of DDT1p4 has been modified slightly to simplify the toy model test. The toy model density profile is shown in Figure 3.1.

3.1.1 Gamma-ray light curve of TM1 and TM2

The gamma-ray light curve of TM1 and TM2 from day 5th to 70th after the explosion is shown in Figure 3.2 (TM1 in black and TM2 in red). The light curves have been computed by integrating the output flux of each day of simulation over the energy band from 0 MeV to 3.6 MeV. Both models display an almost identical shape. However, TM1 has less flux than TM2. This is because TM1 has ∼0.3 $M_\odot$ of ^{56}Ni, meanwhile TM2 has ∼0.5 $M_\odot$ of ^{56}Ni. Moreover, the gamma-packets from TM2 may reach the surface more easily because the core of ^{56}Ni in this models is slightly bigger than in TM1.

The early light curves do not display any signs of the decay of ^{56}Ni, which has a mean lifetime of ∼8.8 days. The flux around this day for both models is very low. Due to the placement of ^{56}Ni in the inner core of the sphere, the photons can not escape the domain at the first stages of the explosion. They are thermalized due to high opacities. However, the flux increases when the density of the models drop because of their expansion.

At later days the flux for both models becomes almost constant. This is because the steady decay of ^{56}Co is fuelling the models. ^{56}Co has a mean lifetime of ∼111 days. Around this date the flux of both models will decrease.

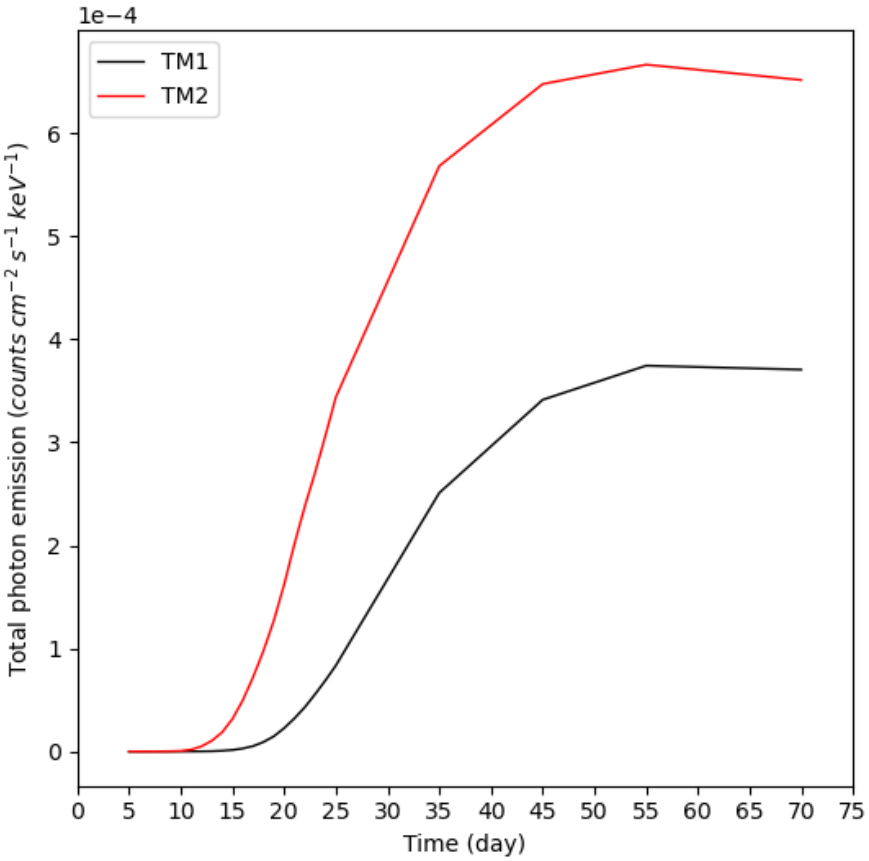

FIGURE 3.2: Gamma-ray light curve integrated over the flux from 0 to 3.6 MeV for model TM1 (black) and TM2 (red) from day 5 to 70 after the explosion.

3.1.2 Gamma-ray spectral evolution of TM1 and TM2

The gamma-ray spectra at days 25 and 70 of TM1 and TM2 are shown in Figures 3.3a and 3.3b. We do not display spectra from earlier days because the flux for both models is too low. At day 25 the spectrum for both models is very similar but TM1 has lower flux than TM2. As seen in the light curves, this is because TM1 has less radioactive material than TM2. We see lines from ^{56}Ni decay (0.480 MeV, 0.750 MeV, 0.812 MeV and 1.562 MeV), and from ^{56}Co decay (0.847 MeV and 1.238 MeV) but not the 0.158 MeV ^{56}Ni decay. This line, despite its high decay probability (see Table 2.2.3), is easily scattered and absorbed as a consequence of its low energy. This is a hint that the origin of ^{56}Ni photons is in the inner layers of the domain. Also, the lines of 0.750 MeV, 0.812 MeV and 0.847 MeV appear defined as narrow lines that are not blended into each other. This suggests that the velocity of the ejecta in which these photons were created is not high enough to mix them by Doppler effect, since the inner layers of the explosion are those with lower expansion velocities. At day 70 the flux has increased, as also seen in the light curves. The spectrum of each model only displays lines from ^{56}Co decay, being the 0.847 MeV and 1.238 MeV dominant. The lines remain as narrow as those of ^{56}Ni displayed at day

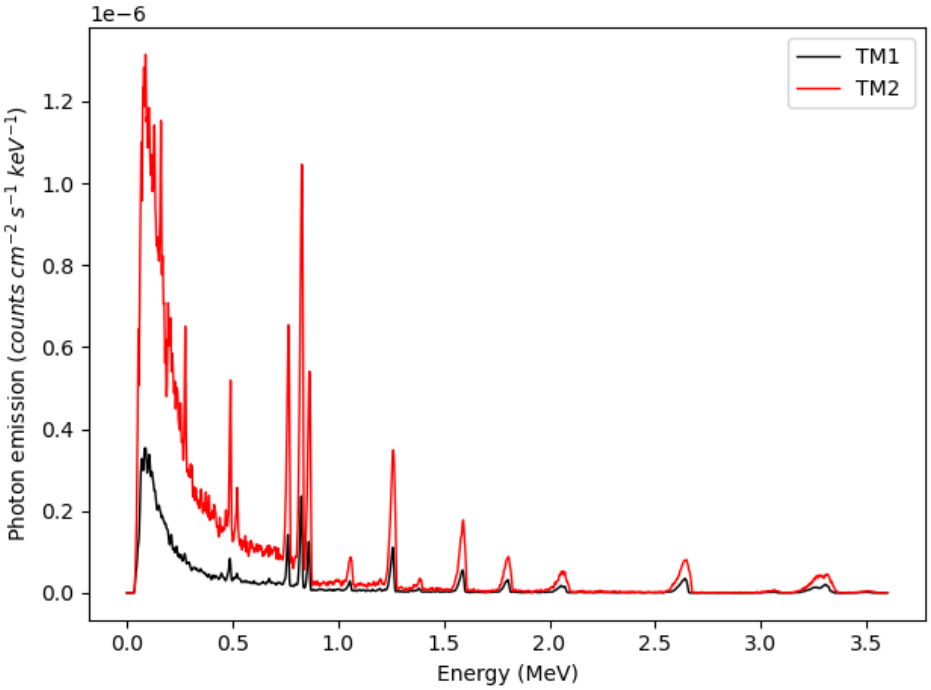

(A)

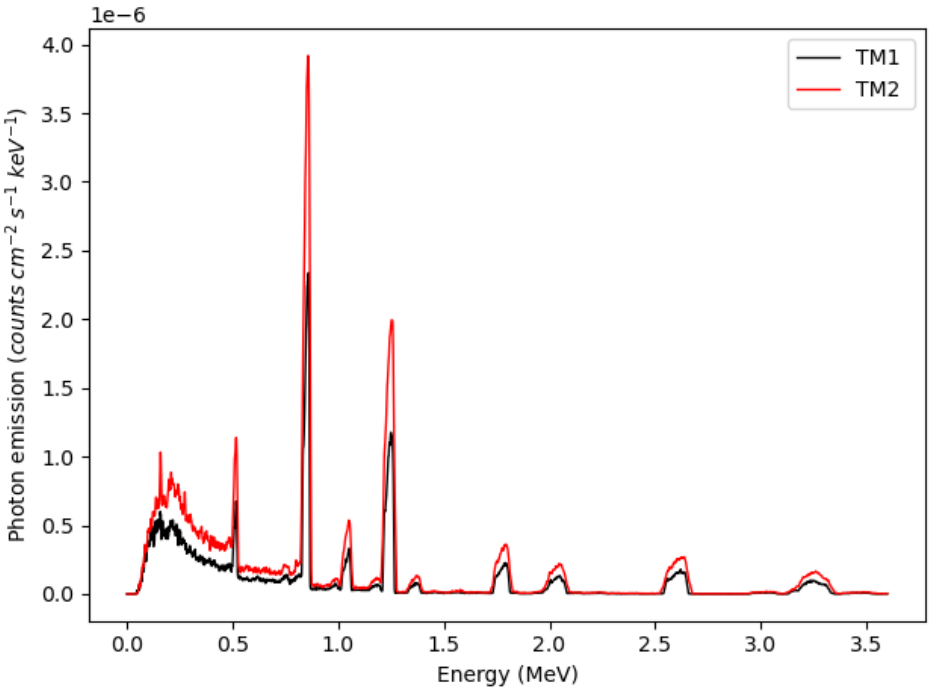

(B)

FIGURE 3.3: (A) Gamma-ray spectra of day 25 for TM1 (in black) and TM2 (in red). (B) As (A) for day 70.

25, in agreement with the placement of the radioactive material in the core of the models.

3.2 Multiple ignition toy model

The beginning of the explosion in a SN Ia may not originate in the core of the WD. It has been suggested that it may be produced by an off-center ignition or by multiple ignition points placed at different locations of the WD (García-Senz and Woosley, 1995; García-Senz and Bravo, 2005; Röpke et al., 2006; Sim, 2007). Given the adequate physical conditions, there could be an ignition of localized spots. The spots, which are subject to fluctuations, could grow to finally trigger the nuclear runaway of the WD.

The multidimensional code described in Chapter 2 allows to reproduce an off-center ignition and multiple ignition spots. These multiple ignition spots originate due to turbulence, buoyancy and drag forces during the burning phase. The experiment is reproduced using a toy model (named TM3). We aim to explore the variances that the synthetic observables in gamma-ray energy band experience in this scenario.

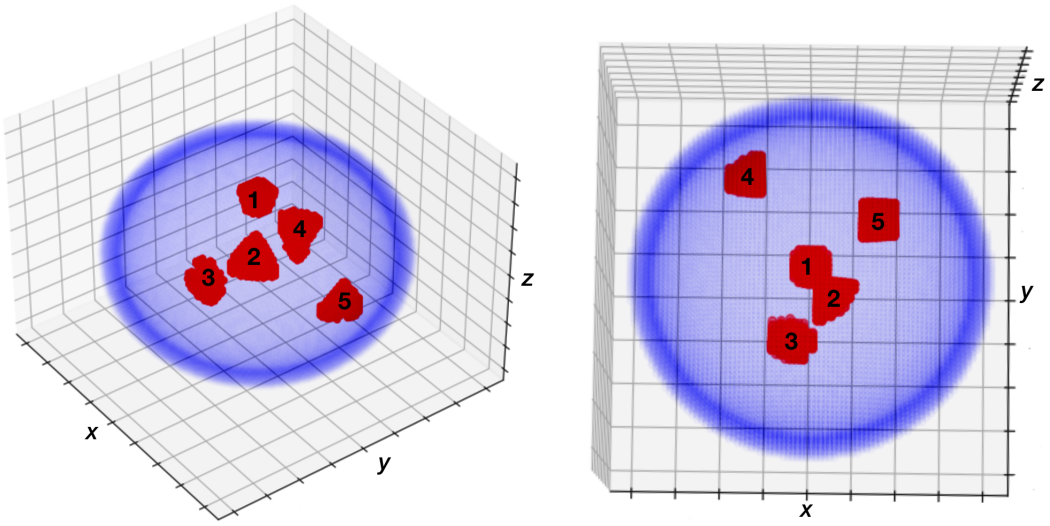

(A) (B)

FIGURE 3.4: Distribution of the multiple ^{56}Ni points in the sphere of model TM3. (A) View from front. (B) View from top.

TM3 is a sphere with an outer layer of C/O and an inner layer of Si. In this sphere we have placed ^{56}Ni in 5 asymmetric sub-domains, which represent the multiple ignition points. ^{56}Ni, Si and C/O represent the main elements found in SN Ia ejecta, as explained in Section 3.1. We display the position of the ignition points inside the sphere in Figure 3.4a and 3.4b. The total mass of the model is 1.36 $M_\odot$, with 0.52 $M_\odot$ of ^{56}Ni, 0.65 $M_\odot$ of Si and 0.19 $M_\odot$ of C/O. The initial radius of the sphere is $1{\cdot}10^9$ km. The outer layer of the model expands at a velocity of $\sim 4{\cdot}10^4$ km s^{-1}. Each sub-domain of ^{56}Ni has an initial density

of $\sim 2.8 \cdot 10^{-5}$ g cm^{-3}. Beside the ^{56}Ni spots, the sphere has a similar density profile to the one shown in Figure 3.1, but with slightly lower density on the inner layers.

3.2.1 Escaping gamma-packets

The different points in which gamma-ray photons are created in the TM3 model may create regions in the ejecta in which the photons escape more easily than in others. To explore this phenomenon we show the position in which the gamma-packets have exited the domain in spherical coordinates. Figure 3.5a shows the density of the gamma-packets depending of the position in which they have exited at days 20 and 70 Figure 3.5a. The gamma-packets are the output of the simulation before they are processed to calculate the gamma-ray flux. Although they are not yet processed, their position is a good indicator of which areas of the model are predominately contributing to the gamma radiation at different stages of the explosion. Further information about the concept of gamma-packets can be found in Chapter 2. The density of gamma-packets is computed using the function *scipy.stats.gaussian_kde*, a Python's library. This function calculates a kernel density estimation of the scatter points in the plot.

Real observations do not provide such information but the modelling of the explosion does and it is interesting to explore. This analysis gives us an idea of how we may miss the asymmetries of a SN Ia explosion due to the limitation that the observer has just one line of view. With the results of this study we also optimize the analysis of the light curve and spectra. It allow us to chose directions of line of view that resemble different scenarios of the explosion.

During the early days of explosion we can observe the appearance of areas in which more gamma-packets escape. A very intense region is seen in the right of the lower hemisphere. This region may be originated by the ignition point number 4 as seen in Figures 3.4a and 3.4b because it is the closest to the surface. There are another two of regions in which the density of gamma-packets is higher than the overall sphere: they are an indicator of the placement of other off-center ignition points. We think that the photons created in the ignition spots closer to the center are absorbed before exiting the domain, otherwise we would observe a higher and diffused emission. At later days the density of gamma-packets is lower and more scattered because there are less decays in that stage and the ejecta has become more transparent.

We define two lines of sight that will be used in the following sections. Direction 1 is the line of sight in which the observer is looking directly to the right lower hemisphere seen in Figures 3.4a and 3.4b. We chose this direction because it presents a high gamma-packet activity. We chose Direction 2 as the line of sight in which the observer is looking at the top of the sphere. The reason we chose Direction 2 is to compare what would happen when observing a region that does not have an obvious presence of gamma-packet activity.

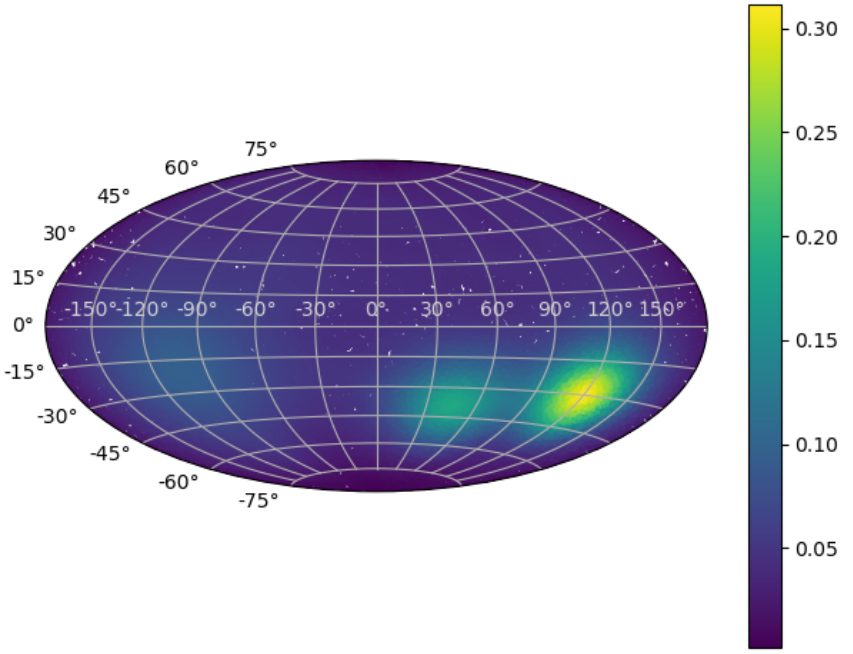

(A)

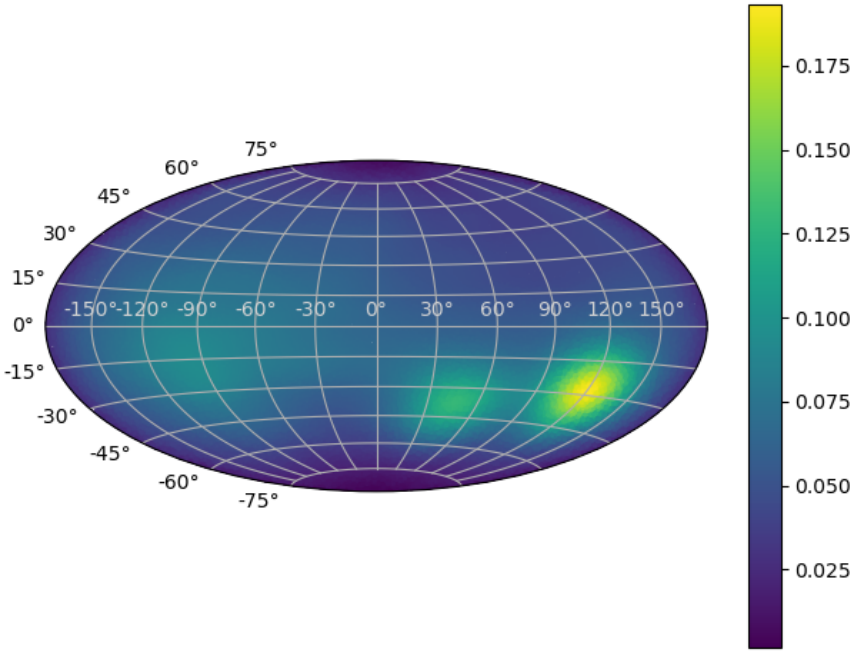

(B)

FIGURE 3.5: (A) Scattering density map plotted over 'aitoff' projection of gamma-packets that escape the simulation of the TM3 at day 20. (B) As (A) but at day 70.

3.2.2 Light curve of TM3

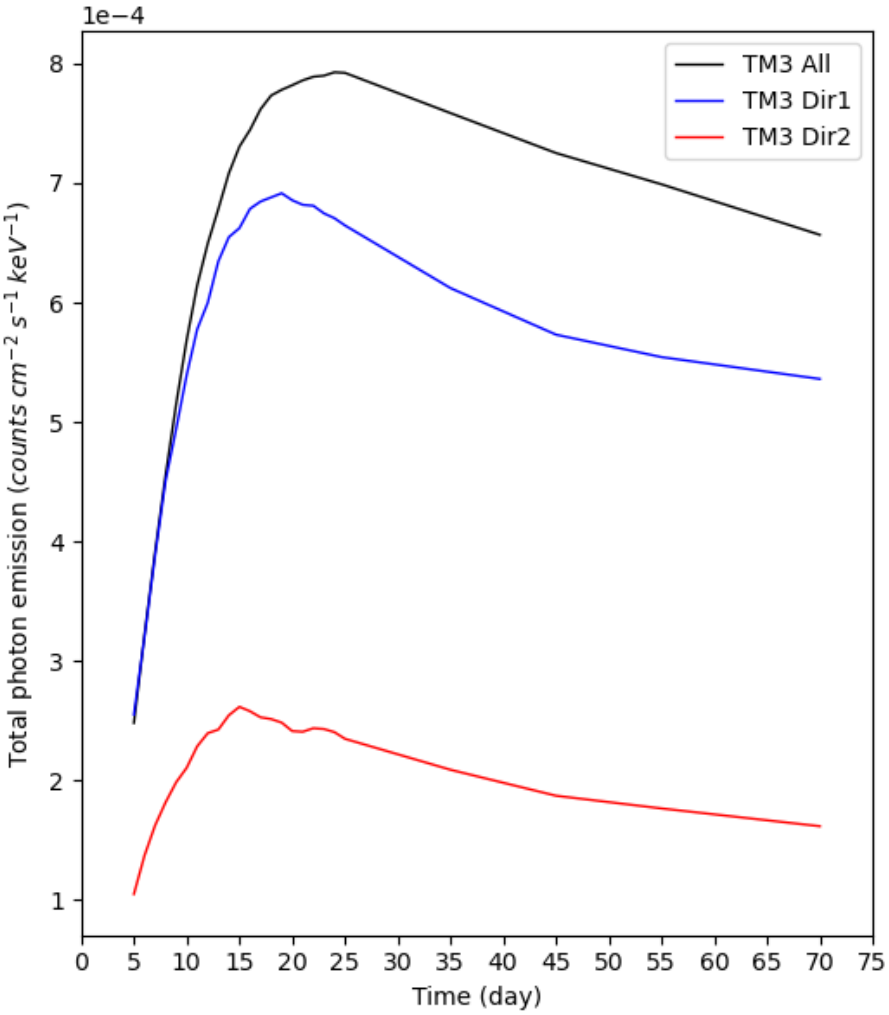

FIGURE 3.6: Gamma-ray light curve integrated over the flux from 0 to 3.6 MeV for model TM3 in all directions (black), for Direction 1 (blue) and Direction 2 (red) from day 5 to 70 after the explosion.

We show the gamma-ray light curve of model TM3 in Figure 3.6 from days 5 to 70 after the explosion. The light curve for all escaping directions is shown in black (TM3 All), for Direction 1 (TM3 Dir1) is shown in blue and for Direction 2 (TM3 Dir2) is shown in red. The choice of directions is explained in section 3.2.1. Once again, they have been computed by integrating the flux over the energy range of 0 MeV to 3.6 MeV. The flux at Direction 1 is higher than Direction 2. They all have a similar rising slope from day 5 to $\sim$ 15. The lower flux from Direction 2 creates more noise in the data and that is why it displays some irregular bumps. Both directions show a maximum around days 10 to 20. This phenomenon is not seen in models with central ignition TM1 and TM2 from section 3.1. Also, TM3 displays a higher flux on early days compared to the models TM1 and TM2. Therefore, the placement of the off-center ignition

in TM3 allows the photons to escape more easily than the central ignition models. The maximum observed is an indicator of off-center ignition to look for in real observations. Moreover, it can be seen from different line of views, even if not looking at the asymmetries directly. This allows to acknowledge the explosion mechanism independently of the direction of observation, in case the early detection is made.

3.2.3 Spectral evolution of TM3

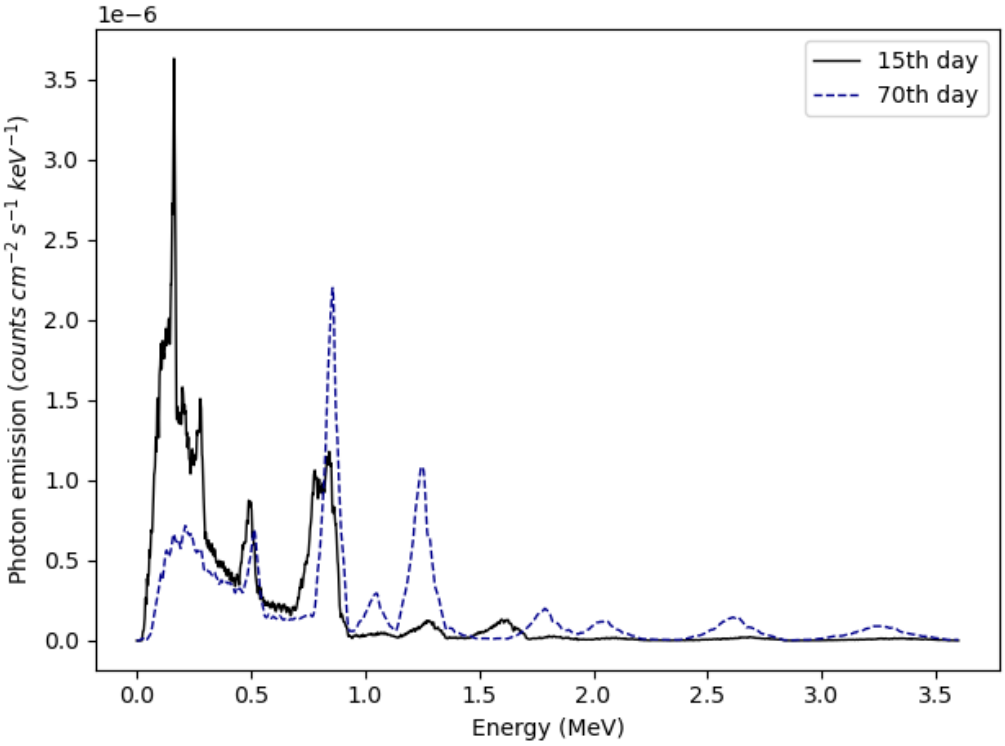

FIGURE 3.7: Gamma-ray spectra at days 15 and 70 after the explosion for all the output directions. 15th in a black line and 70 th day in a dark blue dashed line.

We show the spectral evolution of the flux generated by photons escaping from all directions in Figure 3.7. We show the spectrum at day 15th in a black line and the spectrum at day 70th in a dashed blue line. At day 15th all the lines from ^{56}Ni decay (as seen in Table 2.2.3) are displayed and broadened. The broadening blends lines 0.78 MeV and 0.82 MeV. The broad lines and appearance of line 0.158 MeV at day 15th suggest that the origin of the photons is in places where the ejecta is more transparent and closer to the surface. At day 70th all the lines from ^{56}Co decay can be seen.

We proceed to make the analysis of the spectrum for different lines of sight. Figure 3.8a shows the spectrum at day 15 for Direction 1 in blue (Dir1) and for Direction 2 in red (Dir2). Dir1 considers the observer looking at the line of sight of the right low hemisphere of the explosion (as seen in Figures 3.5a

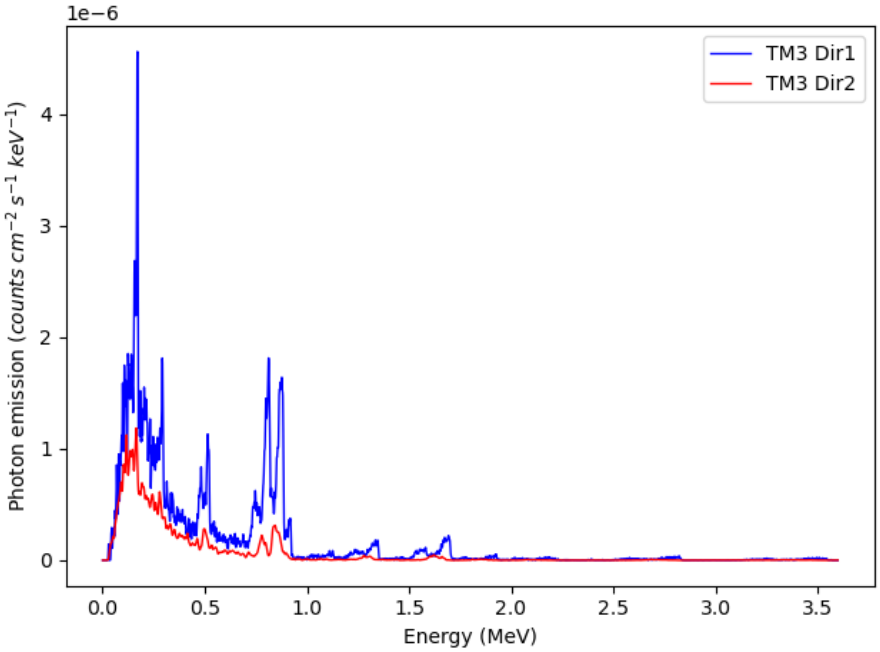

(A)

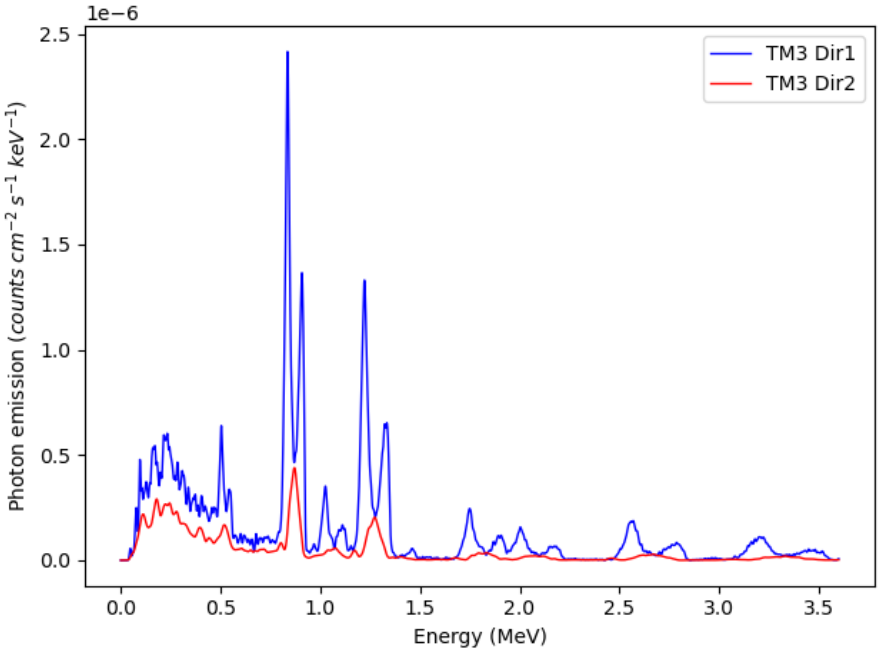

(B)

FIGURE 3.8: (A) Gamma-ray spectra of day 15 for TM3 model for Direction 1 (in blue) and Direction 2 (in red). (B) As (A) for day 70.

and 3.5b). Dir2 considers the observer looking at the line of sight of the top of the sphere. We can see that more photons escape from Dir1 than Dir2. Dir1 displays all ^{56}Ni decay lines at very early days after the explosion. Moreover, the lines are split, which suggests that we see the photons from material moving away from us and towards us. These two signatures are an indicator of an off-center ignition close to the surface layers that allow photons to escape at high velocities. On the other hand, the observer looking at Dir2 does not have this privileged line of sight and would be unaware of the asymmetry of the explosion.

Figure 3.8b shows the spectrum at day 70 for Dir1 in blue and Dir2 in red. Both models show the lines from ^{56}Co decay. However, the split lines behaviour seen in Dir1 at day 15 is even more noticeable. Contrary to day 15, the split lines at day 70 show more red-shifted than blue-shifted photons. This is because the ejecta is more transparent and photons from other ignitions points are visible too, hence the change of tendency. Similarly to day 15, Dir2 at day 70 does not show any signature of multiple ignition points or off-center ignition.

3.3 DDT 3D model with plume asymmetry

We present the results of multiple models with a geometry beyond the regular sphere used in the majority of studies. These simulations are a deeper exploration of the models used in the study of gamma-ray emission of SN 2014J near optical maximum by Isern et al. (2016). In this paper a DDT model with a plume containing ^{56}Ni attached to the surroundings of the spherical model was introduced to explain the ^{56}Ni emission detected from SN 2014J. In this section, we present the synthetic observations that this plume geometry generates in comparison to the regular spherical DDT model. By doing so, we aim to study any possible distinct behaviour in the synthetic observables that may improve our understanding of the explosion mechanism or progenitor system of type Ia SNe.

The isotope ^{48}Cr is synthesized in important amounts during explosive helium burning. This process could provide a favourable scenario for detecting its decaying lines if it occurs in the outer layers of a WD. This isotope has a half-life of $\sim$1.29 days, a time too short to expect a detection. However, ^{48}Cr decays into ^{48}V, which has a half-life is $\sim$23 days, and could be detectable around the optical maximum of the supernova. For further details on ^{48}Cr decay see Appendix A.1.

The main features of the models are explained in 3.3.1. The gamma-ray light curve for each of the models is analysed in section 3.3.2 and the spectra for different days of the explosion is shown in section 3.3.3. Then we explore in detail the variability of the asymmetries by choosing different directions of line of sight in section 3.3.4. In section 3.15 we study the light curves created by the plume models at each of these directions. Finally, we study the spectra from different directions for the plume models in section 3.3.6.

3.3.1 Models

We present the main features of the models used in this study with names: DDT, Plume1, Plume2 and Plume3. The DDT model is a delayed detonation model based on the model named DDT1p4 in Isern et al. (2016). We have adapted this model to the 3D Cartesian grid geometry of our code. We have built a sphere of 1.35 $M_\odot$ that is made of 3,706,160 cubic cells. This composition of the sphere is discretized into 65 subdomains shaped as layers. The original model DDT1p4 has 115 layers but we have scaled them to 65 subdomains in order to reduce the total amount of cells in the simulation, and avoiding an unaffordable computational effort. The DDT1p4 model was initially intended for a 1D code. It allowed 115 subdomains without an extreme computational load due to avoiding the use of a 3D Cartesian grid, thus we needed to adapt it. The density profile of the model is shown in Figure 3.9, where the density of the layers is plotted with their corresponding expansion velocity. The outer layer of DDT model moves with an expansion velocity of $\sim 24,000$ km s^{-1}.

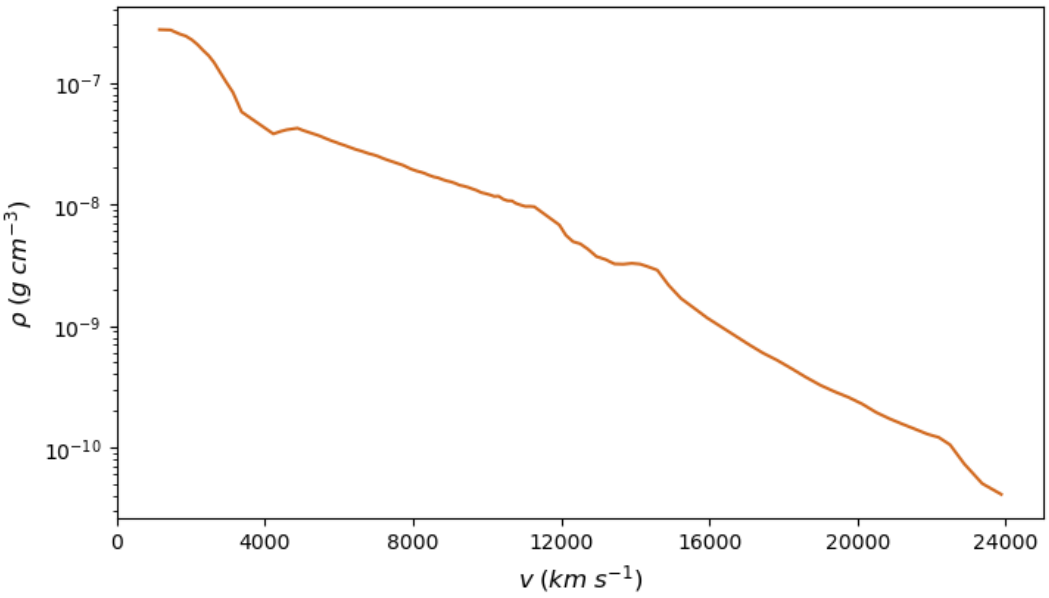

FIGURE 3.9: Density profile of the DDT model in units of g cm^{-3} versus the velocity of expansion in units of km s^{-1} along all the layers of the model.

The Plume1 model is built with the same spherical geometry and composition as the DDT model but with a plume attached to the outer layer of the sphere. This plume has a geometry similar to a ring, as seen in red in Figure 3.10a. The angular thickness of the plume is $\Delta\theta \sim$12 deg and is placed from $\theta = 66$ deg to $\theta = 78$ deg from the z axis of the sphere. A 2D diagram of the position of the plume respect the sphere and the angular position θ and $\Delta\theta$ is shown in Figure 3.10b. The outer layer of the sphere expands at a velocity of $\sim 24,000$ km s^{-1} (as for the DDT) and the outer parts of the plume expand at $\sim 34,000$ km s^{-1}. The inclusion of a plume adds 679, 220 cells to the initial 3, 706, 160 cells of the

DDT model, increasing the computational time of the simulation. The plume in Plume1 model is solely composed of ^{56}Ni with a total mass of 0.07 $M_\odot$.

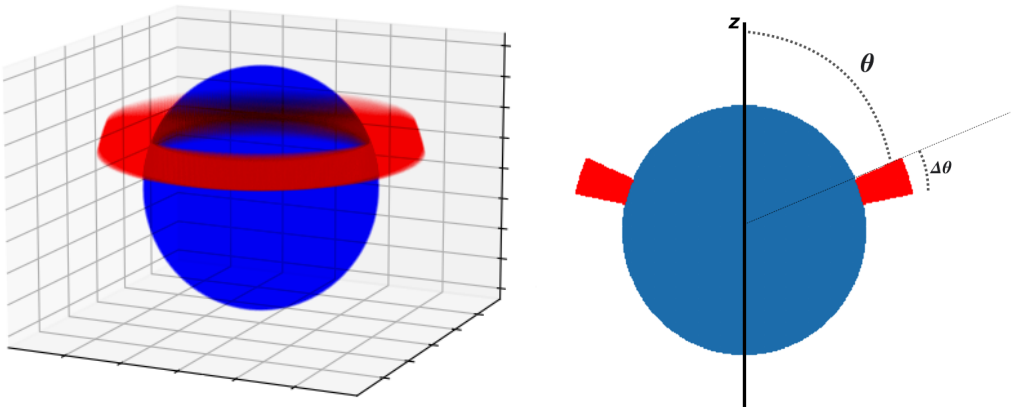

(A) (B)

FIGURE 3.10: (a) 3D plot of the geometry of the models with an attached plume (in red). (b) 2D middle section diagram of (a) model showing the semiaperture angle θ where the plume is placed and the angular thickness $\Delta\theta$ of it.

The other two models, Plume2 and Plume3, have the same features as Plume1 but with different compositions. The plume composition in Plume2 is 0.035 $M_\odot$ of ^{56}Ni and 0.035 $M_\odot$ of ^{48}Cr. The plume of Plume3 is made solely of 0.07 $M_\odot$ of ^{48}Cr. Such amounts of ^{48}Cr are unlikely to be synthesized in real explosions, but in this study we want to highlight its behaviour. All the main features of the four models can be found in Table 3.1.

The synthetic observables for all the models have been computed assuming a distance to the explosion model of 3.5 Mpc, the same distance as SN 2014J.

Model	Plume	v_{max} (km/s)	M_{total} ($M_\odot$)	M_{plume} ($M_\odot$)	^{56}Ni ($M_\odot$)	^{48}Cr ($M_\odot$)
DDT	No	∼24000	1.35	-	0.65	-
Plume1	Yes	∼34000	1.42	0.07	0.65+0.07	-
Plume2	Yes	∼34000	1.42	0.07	0.65+0.035	0.035
Plume3	Yes	∼34000	1.42	0.07	0.65+0.0	0.07

TABLE 3.1: Main features of models DDT, Plume1, Plume2 and Plume3.

3.3.2 Gamma-band light curve

To start our discussion of the four different models we compare the gamma-ray light curve from day 5th to day 70th after the explosion, see Figure 3.11. Each

light curve has been computed by integrating the flux in the energy band of 0 MeV to 3.6 MeV. We have computed the flux as in equation 2.48 for all the gamma-packets escaping in all directions of the domain. Actually, we would not be able to observe the photons that escape from all directions of the ejecta, that is why synthetic observations for different directions have been done in sections 3.3.4, 3.3.5 and 3.3.6. However, we first study the photons that escape from all directions because it provides a general view of the model and allow us to understand better the observables from different lines of sights.

In Figure 3.11 we can the light curve of the DDT model plotted in black. The early light curve of DDT has almost no flux, around day 10 it starts to rise until it reaches its maximum at day ∼35. Although the mean time of the decay of ^{56}Ni is ∼8.8 days we do not see any signature in the spectra around this day. This is because the DDT model has ^{56}Ni just in the core of the domain and the photons created at early days are absorbed before being able to escape. It is not until later days, when the density has dropped due to the expansion, that gamma photons can escape and induce a rise in the gamma-ray light curve. After the 35th day we observe a slow drop of flux. In this stages the photon emission comes from the decay of ^{56}Co. This decay has a mean lifetime of ∼111. Its released energy will power the gamma-ray emission for the rest of the SN Ia.

We can see the other models have a very different light curve profile as compared with the DDT model. First, in red, the Plume1 model has already a high flux at day 5, that rapidly increases until day ∼ 9, when it reaches its maximum, close to mean decay time of ^{56}Ni. The photons generated from ^{56}Ni in the plume of Plume1 model can easily escape and generate the early light curve of the model. After day 9 we see a drop of flux that stops after a few days due to two things: photons created in the inner layers have finally reached the outer layers before being absorbed and early decays of ^{56}Co are happening in the plume. After day 25 the flux drops slowly and is powered by the decay of ^{56}Co as in the DDT model. The flux at day 5 of Plume2 and Plume3 (green and blue lines respectively) is higher than for Plume1. This is because the decay mean time of ^{48}Cr is ∼1.29 days, consequently a higher number of photons are being created in these two models at day 5. Therefore, Plume3 has the highest flux at early days because is the model with highest amount of ^{48}Cr. Plume2 shares signatures with Plume1 and Plume3, because it has a mix of ^{56}Ni and ^{48}Cr. We can appreciate an initial well defined peak around day 9 for Plume2 model, as in Plume1 but softer. Both Plume2 and Plume3 models have its maximum flux around day 25, which is powered by the decay of ^{48}V. Plume3 has the fastest drop of flux of the four models. The fast decrease of flux of Plume3 is due to being the model with higher amount of ^{48}Cr. This radioactive isotope powers the light curve at the early stages of the explosion, allowing to have higher flux than the other models, however once the decay chain is over the flux drops and around day 60 the flux of Plume3 is even lower than Plume2. This rapid decrease of flux may explain some subtypes of SN Ia introduced by Perets et al. (2010), as suggested in Panther et al. (2021). In a real observation this decrease due to ^{48}Cr may not be so exaggerated. This is because, as explained in Section 3.3.1, 0.07 $M_\odot$ of ^{48}Cr is a very high amount of this isotope for a SN

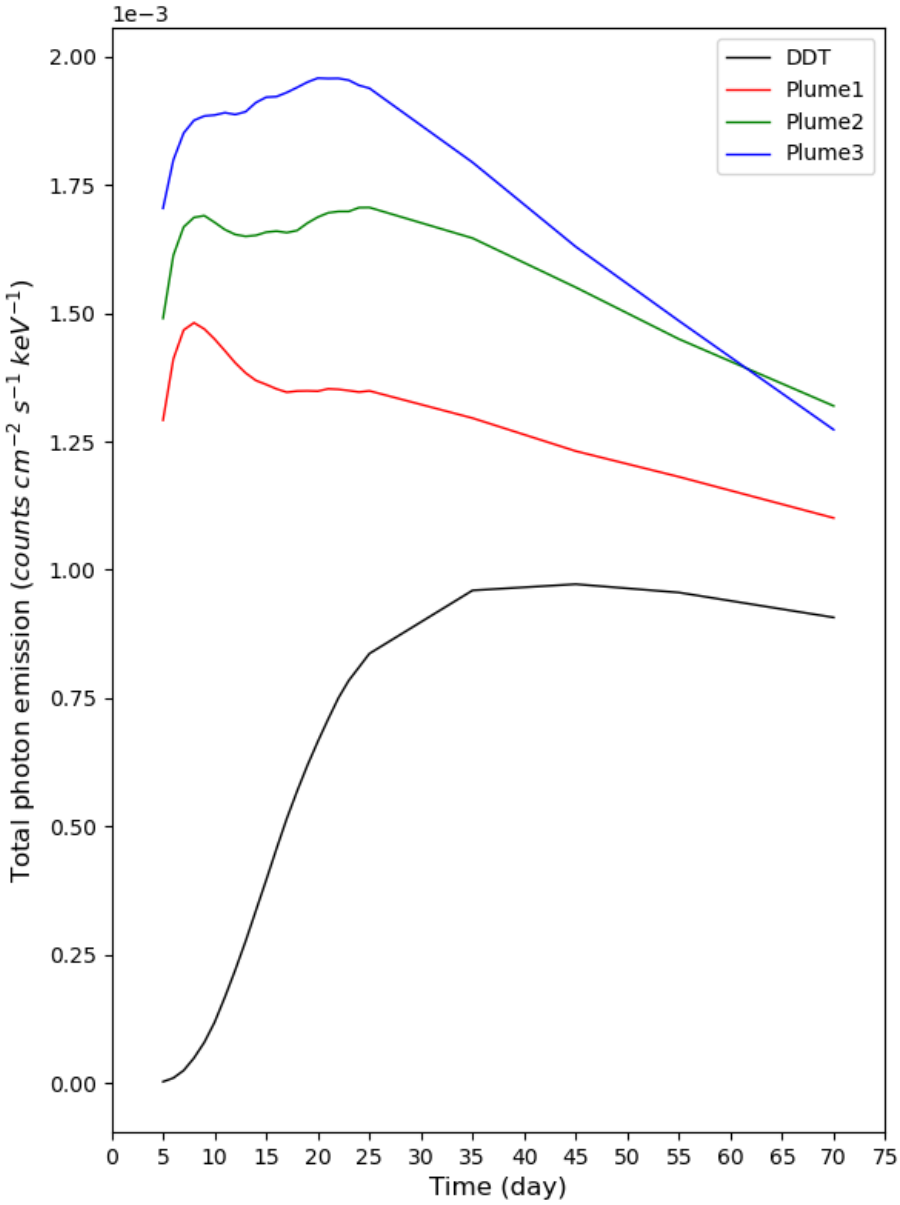

FIGURE 3.11: Gamma-ray light curve integrated over the flux from 0 to 3.6 MeV for model DDT (black), Plume1 (red), Plume1 (green) and Plume2 (blue) from days 5 to 70 after the explosion.

Ia. However, this amount is useful to highlight its behaviour for our study.

Plume1, Plume2 and Plume3 display higher flux compared to DDT. This is because they have higher amount of radioactive material. The placement of the radioactive material in the outer layers also explains the rapid rise of flux in the early stages. The different light curve profiles of each model is explained by the different isotopes composing the plume of each model. Each model has distinctive signatures that allow to differentiate the compositions. They give us information about the kind of progenitor system or explosion model. However, we may miss these signatures in real observation due to not having a favourable

line of sight. This extent is explored in Section 3.3.5. Moreover, some of these signatures are dependent on the early detection of the explosion.

3.3.3 Spectral evolution

We compare the spectral evolution at four epochs: day 10, day 20, day 35 and day 55. These days were chosen to complement the study of the temporal evolution of the flux seen in Figure 3.11. The spectra show the emission of photons that escape the explosion from all directions, which allows to study the behaviour of the models in a general manner. For further details on the dependence on the line of sight see section 3.3.6.

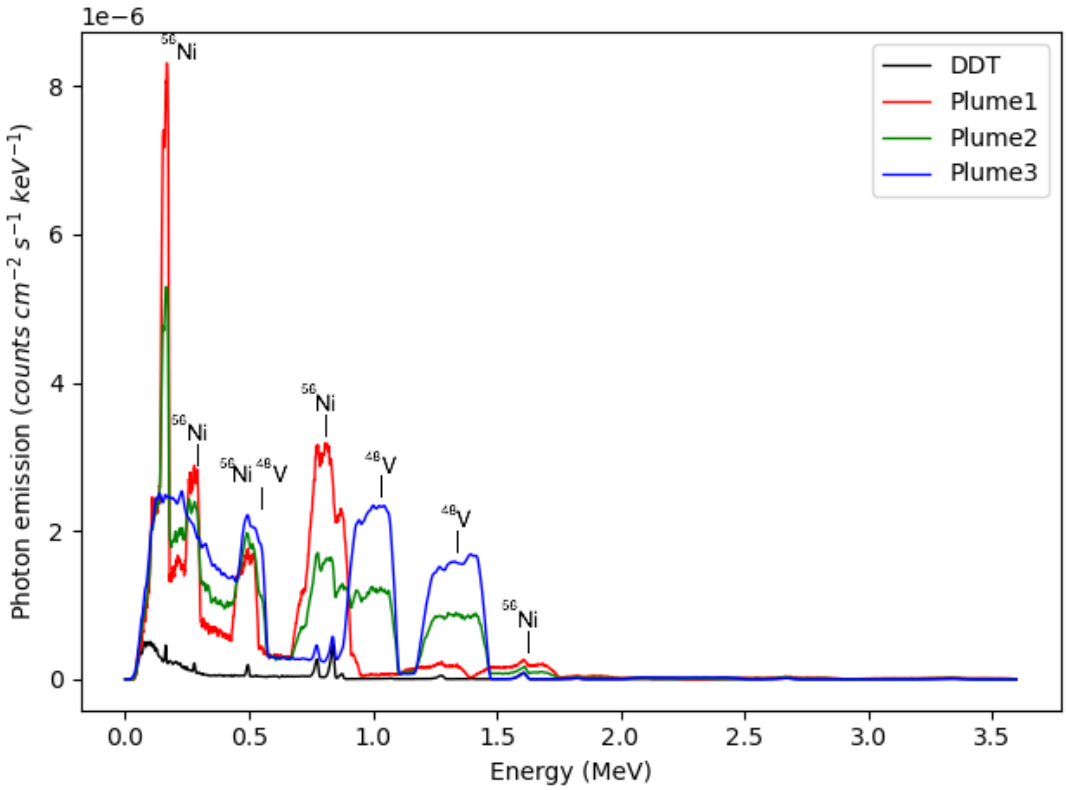

FIGURE 3.12: Gamma-ray spectra at day 10 after the explosion for all the output directions. We display the models DDT (black), Plume1 (red), Plume2 (green) and Plume3 (blue). The isotopes of the most prominent lines are written in the top of each of them.

Figure 3.12 displays the spectra obtained from the escaping gamma-packets at day 10. Real observations of SNe at such early stages are just possible if the explosion is rapidly detected and this has only been recently possible (see Ni et al., 2022). In Figure 3.12, we see in black the spectra of the DDT model, which has a significant lower flux than the other three models. This was also observed in their light curve in Figure 3.11. The other three models show very broad lines. This is an indicator of photons originating at zones with high expansion

velocities. The fact that they are present on the spectra on early days indicates that the photons originate in the plume, as seen on Plume1, Plume2 and Plume 3 models. These photons are able to escape from the domain at early days and therefore the spectra of these models has a higher flux compared to DDT.

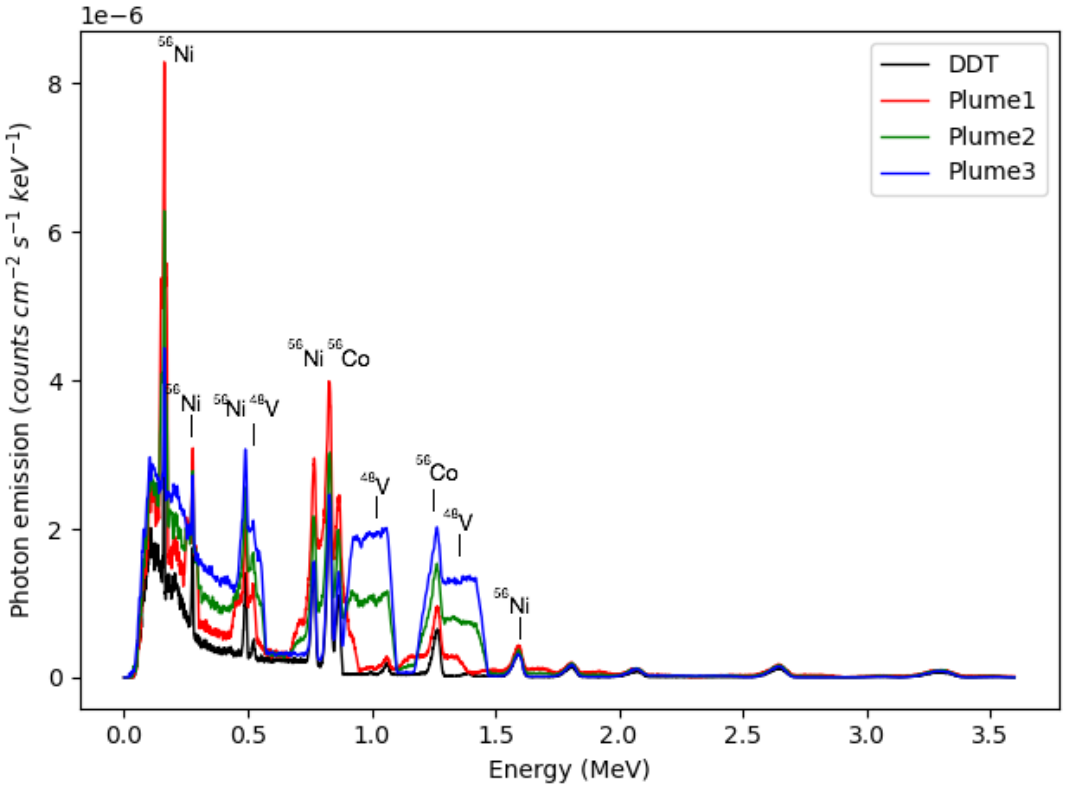

FIGURE 3.13: Gamma-ray spectra at day 20 after the explosion for all the output directions. We display the models DDT (black), Plume1 (red), Plume2 (green) and Plume3 (blue). The isotopes of the most prominent lines are written in the top of each of them.

The names of the isotopes that produce the more prominent lines in the spectra are written on top of them. At day 10th ^{56}Ni lines are dominant on Plume1. For this model, the line of 0.158 MeV is the most prominent and narrow as compared with the other lines. The DDT model shows a continuum at low energies but does not show the 0.158 MeV line because the photons created in the inner core have been absorbed. On the other hand, the 0.158 MeV line on Plume1 has a higher intensity compared to the continuum. This indicates a presence of ^{56}Ni in the outer layers because the photons from 0.158 MeV have not been thermalized or scattered as the ones that create the continuum. Lines 0.270 MeV and 0.480 Mev are seen broadened for models Plume1 and Plume3. We are not able to differentiate ^{56}Ni lines of 0.750 MeV, 0.812 MeV and 0.870 MeV as they are all blended in one broad line. Moreover, in Plume2, these lines overlap a with the 0.983 MeV ^{48}V line. A signature not seen in Plume1 but seen in Plume2 and Plume3 is the broad 1.312 MeV ^{48}V line.

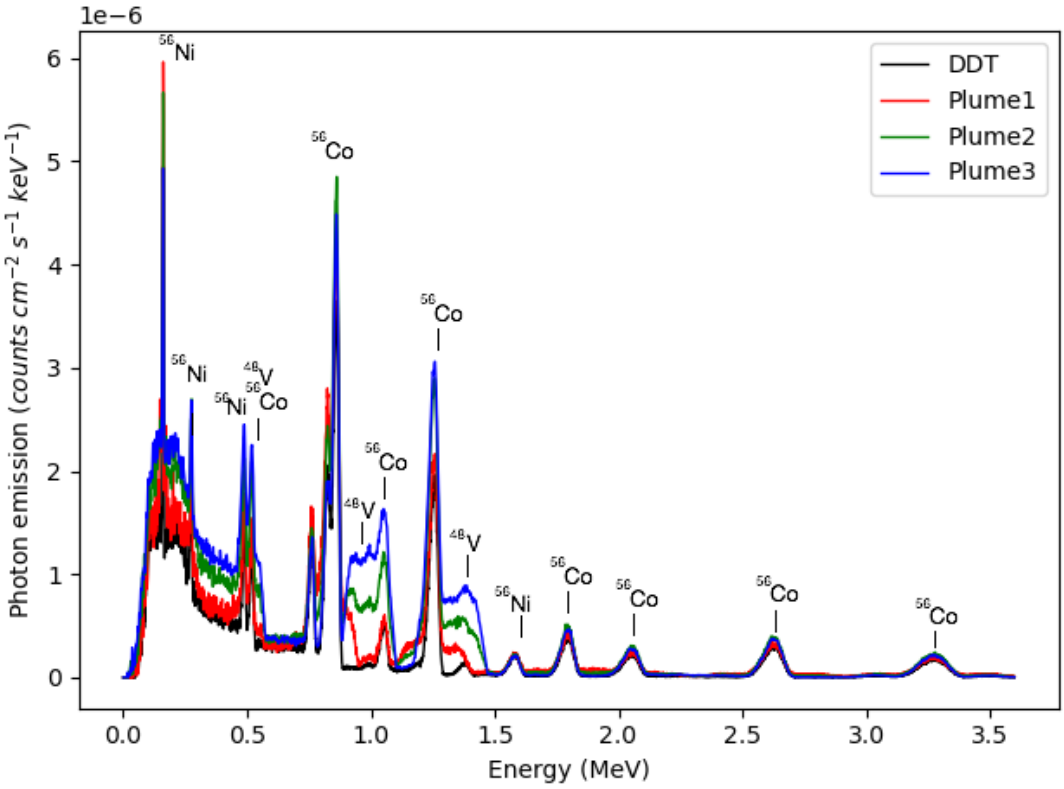

FIGURE 3.14: Gamma-ray spectra at day 35 after the explosion for all the output directions. We display the models DDT (black), Plume1 (red), Plume2 (green) and Plume3 (blue). The isotopes of the most prominent lines are written in the top of each of them.

The spectra at the 20th day after the explosion is shown in Figure 3.13. The DDT spectrum at this stage has increased its flux and displays prominent ^{56}Ni lines and some ^{56}Co lines as the photons in the inner layers are able to escape from the domain. Their narrow shape indicates that photons were emitted by matter moving at low velocity, i.e. from inner zones. This inner photon emission is also seen on the spectra of Plume1, Plume2 and Plume3, which all share the same internal composition as the DDT model. Nonetheless, in this stage of the spectra we still observe strong signatures of photon emission in the plume for all three plume models, similar to the 10th day.

Figure 3.14 shows the 35th day after of explosion. We observe a reduction of the flux in broadened lines generated by the plume for models Plume1, Plume2 and Plume3. DDT model displays a general increase of flux and multiple ^{56}Co lines, such as 0.847 MeV, 1.038 MeV, 1.238 MeV, 1.772 MeV, 2.035 MeV, 2.598 Mev and 3.254 MeV, as displayed in the spectra. For models Plume2 and Plume3 the broad lines 0.983 MeV and 1.312 MeV of ^{48}V are still recognisable in the spectra but they are now blended with the ^{56}Co lines of 1.038 MeV and 1.238 MeV, respectively. Plume1 and Plume2 show almost no sign of the outer layer emission of the decay chain of ^{56}Ni. Finally, in Figure 3.15, we show the 55th

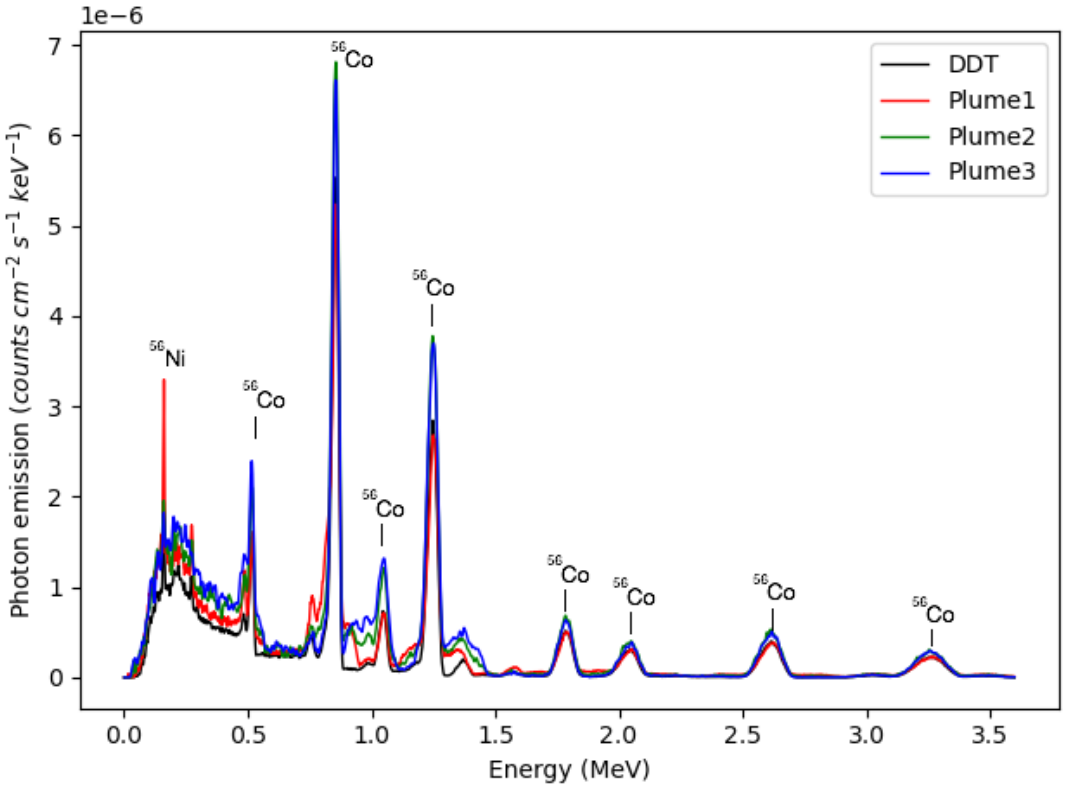

FIGURE 3.15: Gamma-ray spectra at day 55 after the explosion for all the output directions. We display the models DDT (black), Plume1 (red), Plume2 (green) and Plume3 (blue). The isotopes of the most prominent lines are written in the top of each of them.

day of explosion, where the signs of broad lines of ^{56}Ni and ^{48}V have disappeared and all the models resemble the DDT model.

3.3.4 Asymmetries

The previous sections have shown the synthetic observables of the processed gamma-packets that escape the domain from all directions. This approach gives us a general knowledge of how the chemical composition and distribution of the model produces variabilities in the all-direction gamma-ray light curve and spectra. We could consider that the study of these observables would be enough for experiments with 1D models or models that do not have any asymmetry on their geometries. However, our code was designed to be able to simulate explosion in a 3D fashion, which allows to study the variability on synthetic observables caused by the line of sight. Therefore, we continue to analyse the synthetic observables taking into account the asymmetries of our models. To do so, we first want to show the position of the gamma-packets that escape the ejecta at days 20 and 70 to explain the choice of the directions we use in later sections.

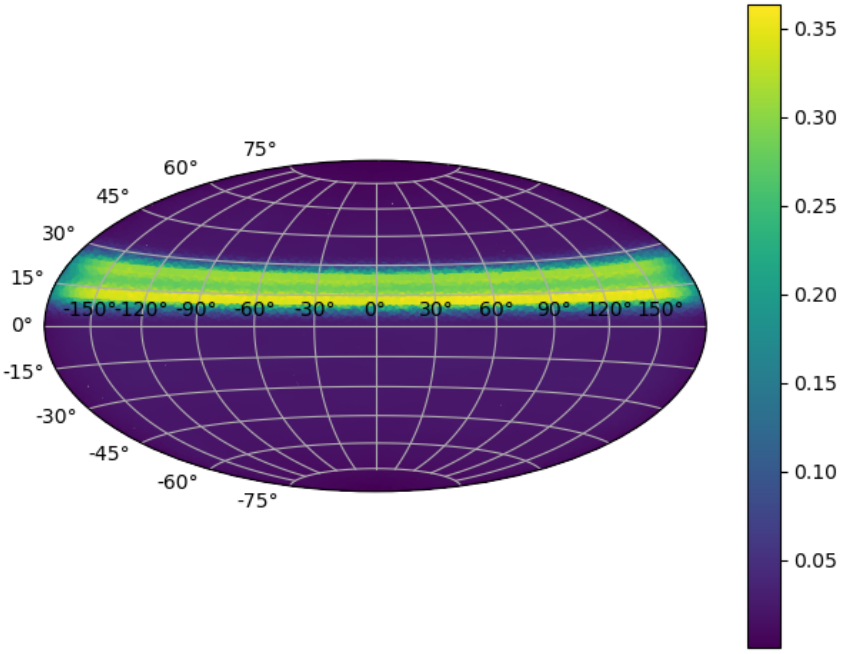

(A)

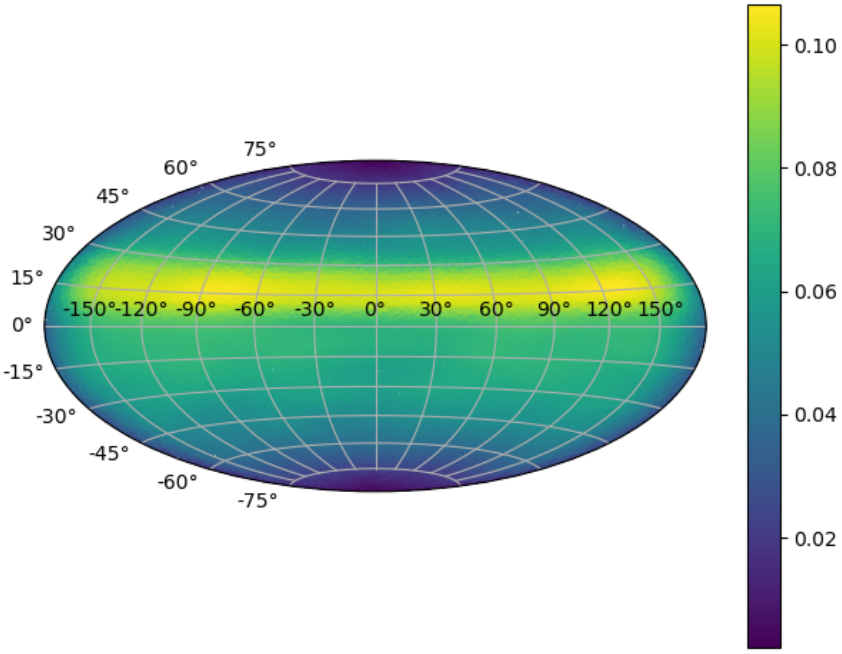

(B)

FIGURE 3.16: (A) Scattering density map plotted over 'aitoff' projection of gamma-packets that escape the simulation of a plume model at day 20. (B) As (A) but at day 70.

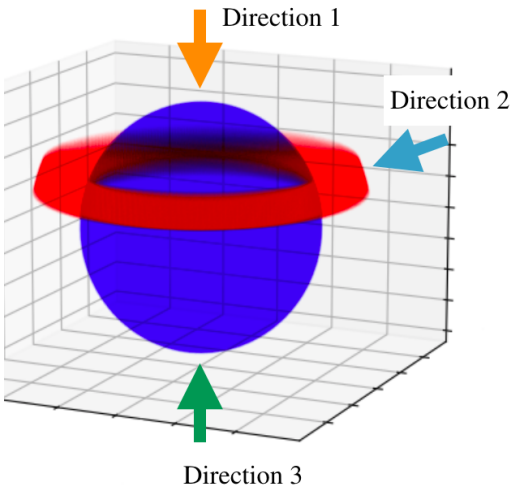

(A)

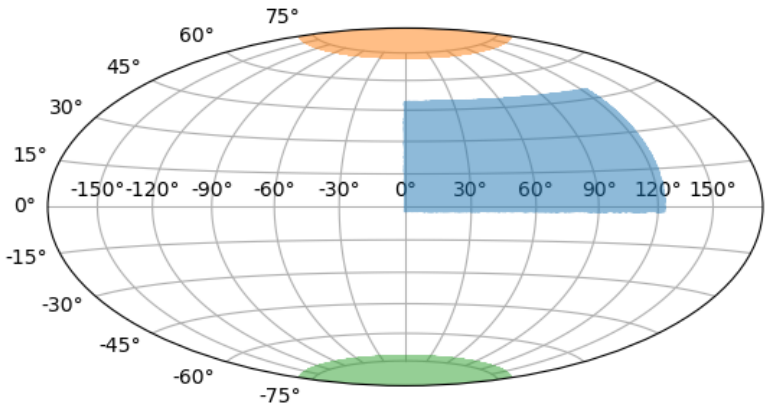

(B)

FIGURE 3.17: (a) 3D plot of plume model that shows the directions of observation used in this work. Direction 1 looks at the the top of the model, Direction 2 at the plume and Direction 3 at the bottom. (b) Map of the solid angle areas for Direction 1 (orange), Direction 2 (blue) and Direction 3 (green).

The position of the gamma-packets that escape the Plume3 model at day 20 is shown in Figure 3.16a and at day 70 in Figure 3.16b. Both plots show the density of gamma-packets in an 'aitoff' projection with spherical coordinates. The density of gamma-packets is computed using the function *scipy.stats.gaussian_kde*, a Python's library. This function calculates a kernel density estimation of the scatter points in the plot.

The choice of model Plume3 above model Plume1 and Plume2 is redundant for the purpose of this figure. The three models have the same geometry and total amount of radioactive material. We do not show the gamma-packets that escape the DDT model as it does not have any asymmetry.

Figures 3.16a and 3.16b do not show the real photon emission. The plots are build using the gamma-packets that escape the ejecta, before they are processed to calculate the gamma-ray flux. Although they are not yet processed, Figure

3.16a and 3.16b are a good indicator of which areas contribute to gamma radiation at different stages of the explosion. We can see in Figure 3.16a that the plume is the main area where gamma-packets escape at the 20th day of the explosion. For later stages of the explosion the gamma-packets that escape are more distributed along all the domain. We can see in Figure 3.16b that the plume is still noticeable at day 70 but has less density than at day 20. These results are complementary to the results shown in sections 3.3.2 and 3.3.3.

The directions that we will use in the following sections to study the light curve and spectra of the asymmetric models (Plume1, Plume2 and Plume3) are chosen in order to display different kinds of behaviours given the possible field of view of the observer. Given the density distribution shown on Figures 3.16a and 3.16b we have chosen three lines of view. The first direction (Direction 1) is set to observe the explosion from top of axis z, as if the observer would be looking at the north pole of the sphere. The second direction (Direction 2) aims to observe the explosion as if the observer line of view is on the bisection axis of the plume, this is to say we observe the asymmetry of the explosion from the front. Finally, we chose a third direction (Direction 3) that points to the furthest point from the plume and it is opposite to the first direction. These directions are shown in Figures 3.17b and 3.17a.

3.3.5 Gamma band light curve from different directions

Once we have chosen different directions in which we can observe the explosion, we proceed to analyse the light curves made by the models Plume1, Plume2 and Plume3. We aim to study how the direction of observation may impact the discovery of the asymmetries of the explosion. The light curves go from days 5 to 35 for each model. The reason we have selected these days is because we do not expect a detection earlier than 5th day and, as seen in sections 3.3.2 and 3.3.3, not many signatures induced by the asymmetries are expected to be seen later than the 35th day. The results displayed in Figure 3.18 show side to side the comparison of the light curve for each direction. A thing to notice on these results is that the amount of noise to the data is highest than for the overall light curves displayed in Figure 3.11. This is because by reducing the area of view we process less gamma-packets for the results, therefore the noise in the data increases.

We observe a lower flux in Direction 1 and Direction 3 than in Direction 2. This is due to Direction 1 and 3 being further from the plume and so less photons escape in these directions in the first weeks (see Figure 3.16a). We can even observe that Direction 1 has a slightly higher flux than Direction 3 for each of the models. This is due to Direction 1 being closer to the plume than Direction 3. Direction 2 has the highest flux because is looking at the plume directly, which is the highest area of emission of photons (see Figure 3.16a and 3.16b).

At Direction 2 we observe that there is a rapid increase of flux from the very beginning for all three models. In a real observation this would be a hint of radioactive material placed in the outer layers, as they can escape the ejecta easily.

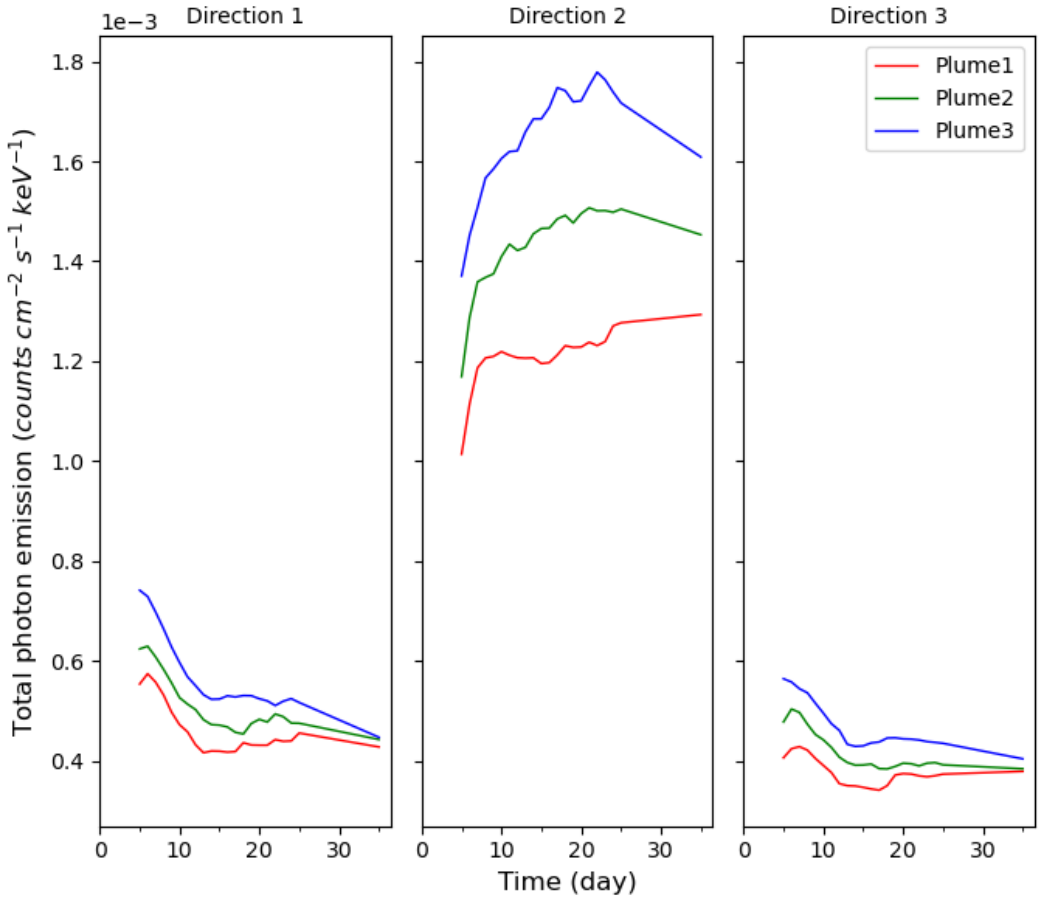

FIGURE 3.18: Gamma-ray light curve for three directions of field of view for model DDT (black), Plume1 (red), Plume2 (green) and Plume3 (blue) from days 5 to 70 after the explosion.

Comparing the three models in this direction, we can observe that Plume1 has a rapid rise until day ∼9, and after that the rising is slower. On the other hand, Plume2 and Plume3 have a rapid rise until day ∼22. That is an indicator of which are the isotopes creating the light curve. ^{48}Cr and ^{48}V have a decay mean lifetime of 1.296 days and 23.045 days, respectively. This explain the rise of flux of Plume2 and Plume3 at the first days. Plume1 just has ^{56}Ni as radioactive material. If we are able to observe at early days the way in which the light curve rises, then we could determine the presence of radioactive material in the outer layers of the explosion and the kind of isotope causing the emission.

Although, the overall flux for all the models in Direction 1 and Direction 3 is lower than for Direction 2, there are still some hints of the asymmetries and isotope composition of the models. All the models show a rapid decrease of flux that later slows down. This is a consequence of the high photon emission during the very early days, a phenomenon not seen in models that just have radioactive material in the inner layers (see DDT model in Figure 3.11). Another detail to take into account, as it can be seen in Figure 3.18, the light curve of Plume1 displays a maximum of flux after three days, while for Plume3 we are not able to record this maximum, and for Plume2 is debatable if we missed it or not. This

behaviour is consequence of the decay mean lifetimes of ^{56}Ni and ^{48}Cr. However, it is rare to detect a SN before the 10th day of explosion and so the observer looking at Direction 1 or Direction 3 would have missed the signatures generated by photons emitted at the outer layers. A recent study (Ni et al., 2022) has been able to observe SN 2018aoz in the $B - V$ band from the first day after the explosion, as they estimate. This study has found an excess of radioactive material in the outer layers of the ejecta, which endorse the motivation of our work. Therefore, it is of great interest to detect the very early gamma emission of a Type Ia supernova because it could provide a deep insight on the explosion mechanism and nature of the progenitor system. The early detection of gamma ray has not been yet possible as a consequence of the expected low luminosity and the distance at which all SN Ia have occurred. As it is of great interest to improve the early detection of these event, we have analysed the possibility of an early detection of a galactic SN Ia in Chapter 4.

3.3.6 Spectra from different directions

The synthetic spectrum for the three plume models at different directions provides complementary information to the light curves seen in section 3.3.5. We proceed to show the spectra of models Plume1, Plume2 and Plume3 for each of the chosen directions. The spectra are plotted for days 15th and 35th after the explosion. We show the spectra in the energy range of 0.6 MeV to 1.6 MeV. This range allow us to focus on the main features of ^{48}V that we have seen in section 3.3.3, where the lines 0.983 MeV and 1.312 MeV are seen as a big broad line. This energy range also has prominent lines of ^{56}Ni, such as 0.750 MeV, 0.812 MeV and ^{56}Co, like 0.847 MeV and 1.238 MeV.

The spectra for Direction 1 (see Section 3.3.4 to know about the chosen directions) is shown for day 15 in Figure 3.19a and for day 35 in Figure 3.19b. At day 15 the Plume1 model displays the lines of 0.750 MeV, 0.812 MeV with a clear blueshift. We can see how the 0.812 MeV ^{56}Co line blends with the 0.847 MeV ^{56}Co line. We also see how the 1.238 MeV ^{56}Co line starts to appear. For model Plume3 at day 15, ^{56}Ni lines are very weak. The dominant lines are from ^{48}Cr decay in its plume, which only contains this isotope. Plume2 displays a mix of ^{56}Ni and ^{48}Cr lines. These are shown independently in the other two models but in Plume2 we observe all of them with a smaller flux. Once the simulation reaches day 35 the lines of 0.847 MeV and 1.238 MeV of ^{56}Co are seen in all the models. Their late appearance and the fact that they are not blueshifted, is an indicator that they come from the inner layers.

If we move our line of sight to Direction 2, the spectra for days 15 and 35 of the three plume models are displayed in Figures 3.20a and 3.20b. All three models display broad lines at day 15 compared to Direction 1 and Direction 3. Plume1 shows lines of ^{56}Ni and ^{56}Co blended in the energy range of $\sim$0.7 MeV to $\sim$0.9 MeV. If we move to day 35 we can see that the lines created in the core of the explosion become dominant over the broad lines created in the plume.

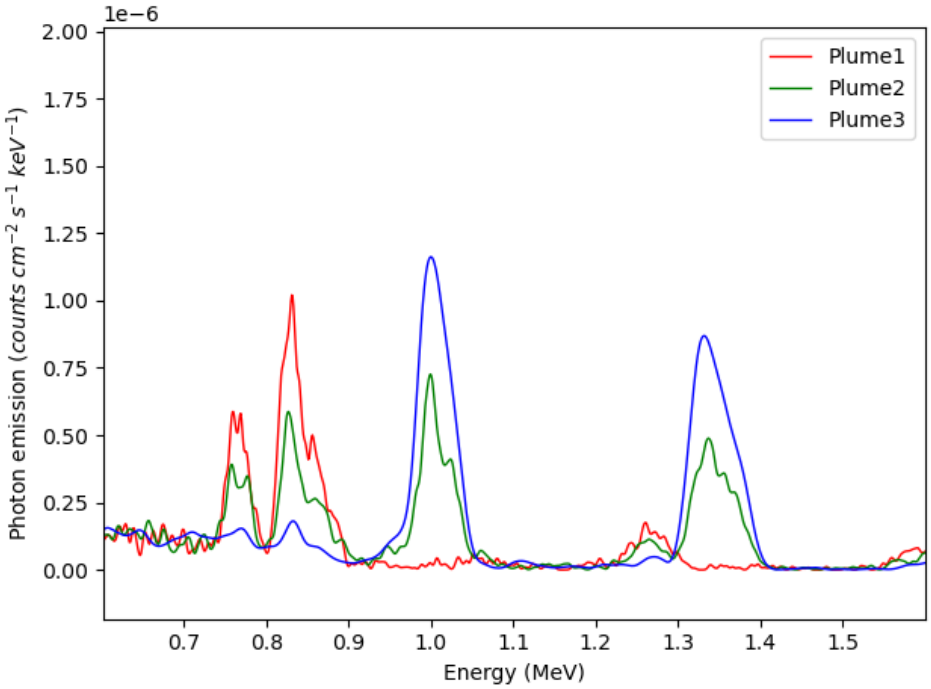

(A)

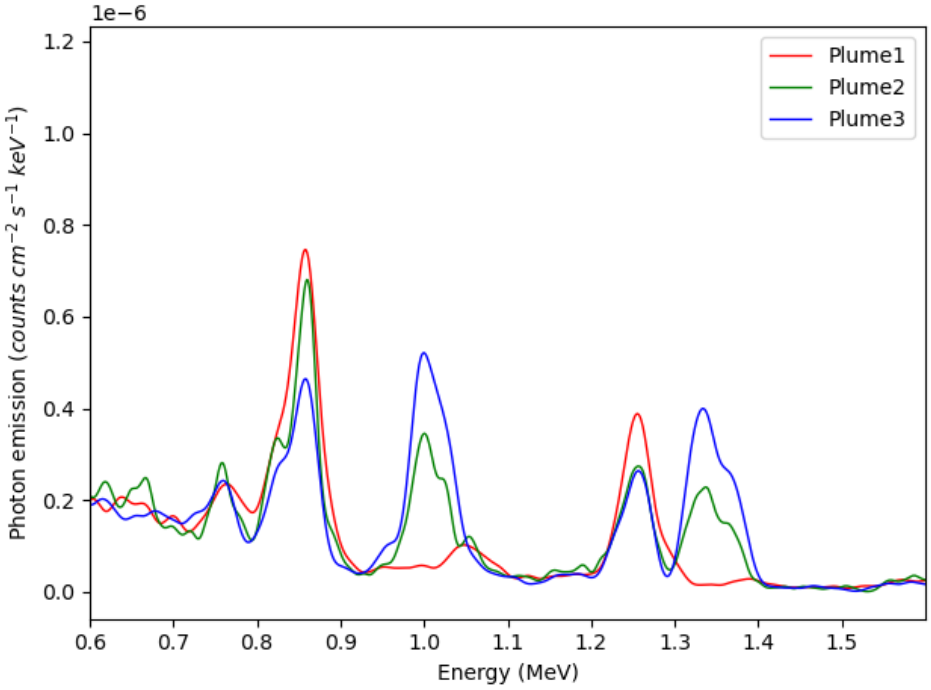

(B)

FIGURE 3.19: (A) Gamma-ray spectra of day 15 for Direction 1 as line of view. We display the energy range from 0.6 MeV to 1.5 MeV for Plume1 (red), Plume2 (green) and Plume3 (blue) (B) As (A) for day 35.

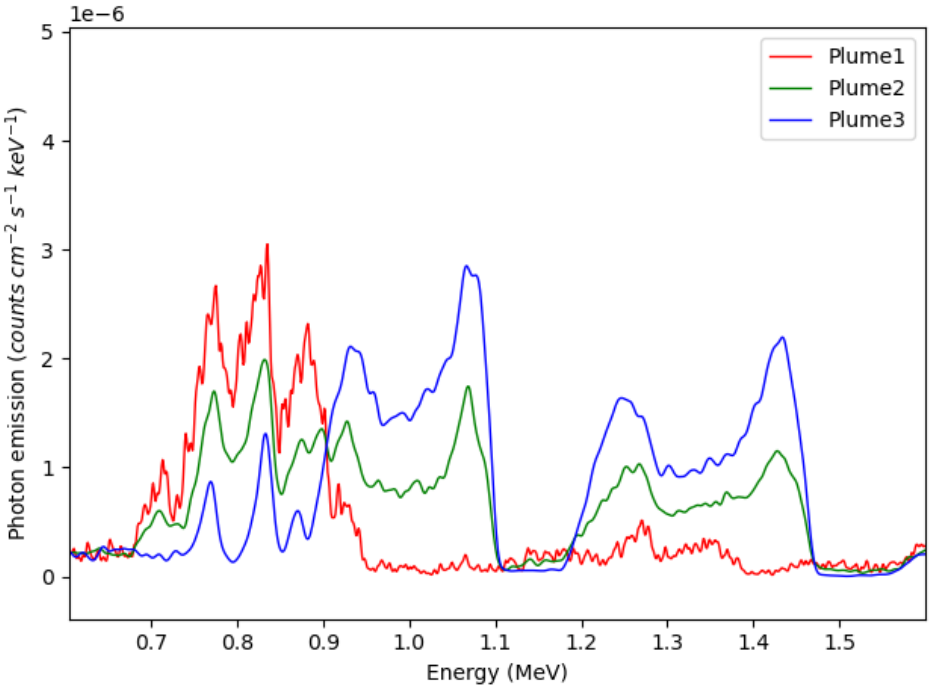

(A)

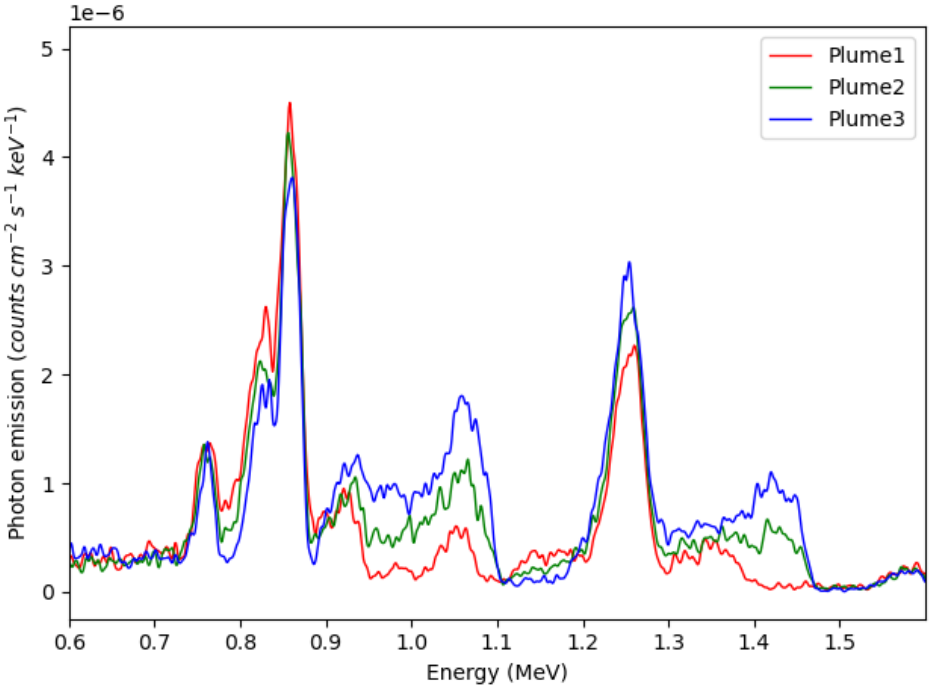

(B)

FIGURE 3.20: (A) Gamma-ray spectra of day 15 for Direction 2 as line of view. We display the energy range from 0.6 MeV to 1.5 MeV for Plume1 (red), Plume2 (green) and Plume3 (blue) (B) As (A) for day 35.

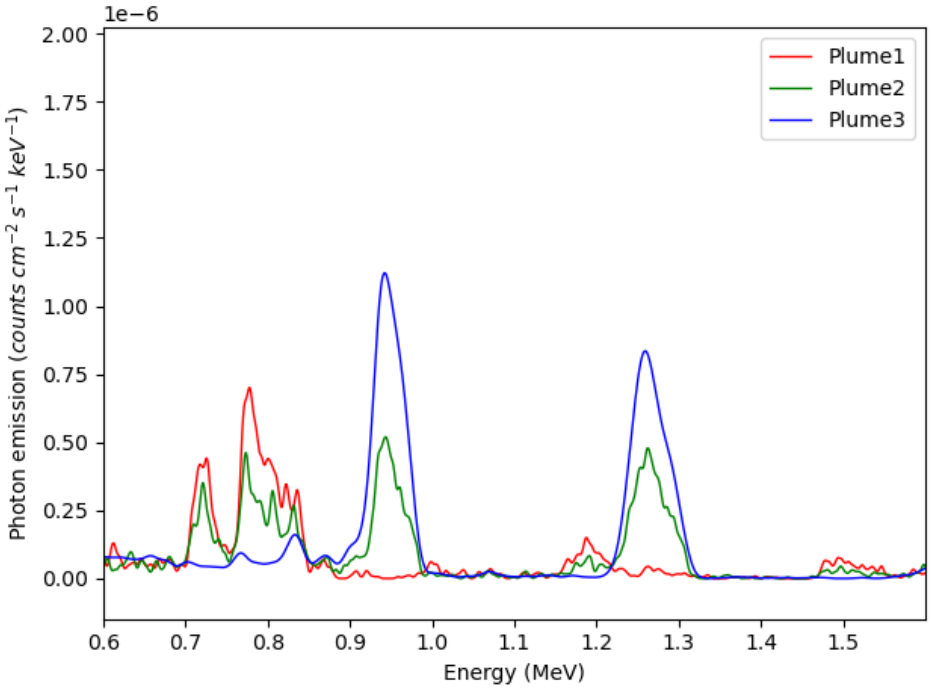

(A)

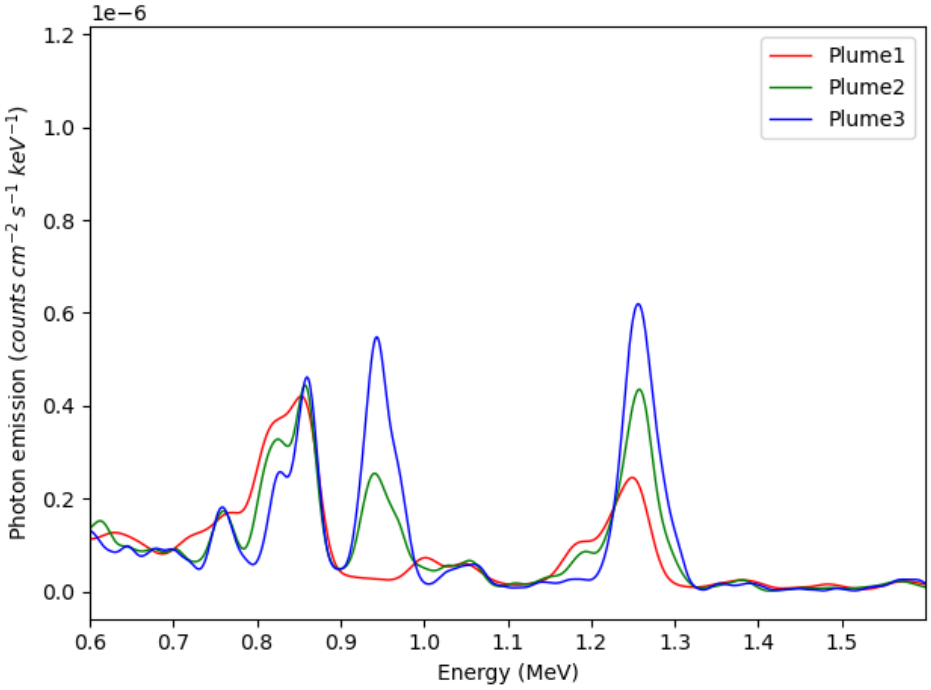

(B)

FIGURE 3.21: (A) Gamma-ray spectra of day 15 for Direction 1 as line of view. We display the energy range from 0.6 MeV to 1.5 MeV for Plume1 (red), Plume2 (green) and Plume3 (blue) (B) As (A) for day 35.

Finally, looking at the spectra in the line of sight of Direction 3 (Figures 3.21a and 3.21b) we have a similar profile as in Direction 1. However, at day 15 the lines from Direction 1 are blueshifted and the same lines from Direction 3 are redshifted. This is due to the relative position of Direction 1 and Direction 3 to the plume (see Figure 3.17a). If in a real observation we were able to identify which lines originate from ^{56}Ni decay and ^{48}V decay we could obtain a hint about the position of the source of the gamma emission. At day 35 we see the display of lines created in the inner layers of the domain, which are narrower and not shifted. Direction 3 shows a peculiar behaviour that we find important to comment. We see how the line of 1.2 MeV from ^{56}Co decay appears at the same energy that the redshifted line of 1.312 Mev of ^{48}V decay. This could lead to wrong conclusions about the origin of the line. The line of 0.983 Mev of ^{48}V decay seems more helpful in order to detect this material in the observations although its closeness to lines of ^{56}Ni and ^{56}Co decay may appear blended in the spectra and be missed. Specially if the quantity of ^{48}Cr is low.

3.3.7 Did SN 2014J have ^{48}V emission lines?

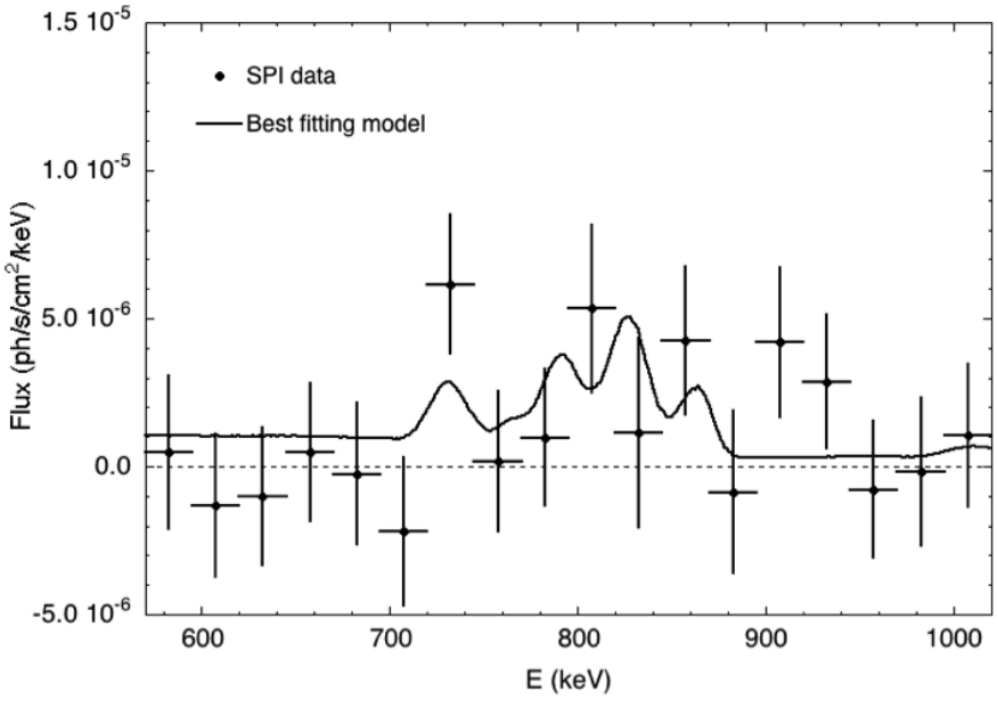

FIGURE 3.22: From Isern et al. (2016), gamma-ray spectrum of SN 2014J (16.5 - 35.2 days after the explosion).

We want to conclude this chapter by making a small observation and maybe opening future lines of study. In this study we have shown the consequences of the presence of radioactive material in the outer layers of SN Ia. As we see in Figure 3.22, borrowed from Isern et al. (2016) , the SPI data shows emission at usual places of the spectra in which lines of ^{56}Ni and ^{56}Co dominate. The best fitting model is in our study the equivalent of Plume1, which only had ^{56}Ni

in the plume. However, we wonder if the data points in the range ∼0.9-0.94 MeV, in which the best fitting model seems to not have emission lines, may be a missed detection of ^{48}V lines. Plume2 and Plume3 models have displayed gamma-ray emission on this range of energy. However, observations with better sensitivity are needed in order to deepen into such assumption.

Chapter 4

Sensitivity of the anticoincidence system of SPI for detecting a galactic supernova

The detection of the very early gamma emission of a Type Ia supernova could provide a deep insight on the explosion mechanism and nature of the progenitor system. However, this early detection has not been yet possible as a consequence of the expected low luminosity and the distance at which all the events have occurred up to now. The closer SN Ia ever detected in gamma-rays is SN2014J. It was discovered by Fossey et al. (2014). It was found in M82 at a distance of 3.5 Mpc. SPI instrument on board of INTEGRAL collected gamma rays from day 16.3 to 164 after the explosion. The detection of ^{56}Ni and ^{56}Co lines of this nearby event allowed to prove the usefulness of gamma detection to diagnose the dynamics and composition of the ejecta (Churazov et al., 2014; Diehl et al., 2014; Isern et al., 2014; Churazov et al., 2015; Isern et al., 2016).The analysis of these observations not only confirmed the hypothesis that the light curve was powered by the disintegration of the ^{56}Ni radioactive chain but also allowed to compute in a direct way the total amount of ^{56}Ni synthesized during the event. Furthermore they showed, unexpectedly, that ~ 0.05 M$_\odot$ of ^{56}Ni was present in the outer layers forming a non spherical structure. The non spherical structure was indicated by the display of redshifted and high intensity lines of ^{56}Ni in the early spectrum.

A Galactic supernova would be ideal for more detailed studies, specially if detected during the rising epoch of the light curve. The expected rate is estimated to be $1.4^{+1.4}_{-0.8}$ events per century (Adams et al., 2013) in the case of SN Ia. The optical flux would probably be so attenuated by interstellar extinction that would prevent triggering the observations with gamma-spectrometers at the due time. However, it is important to realize that the Galactic plane is transparent to gamma rays for which reason events severely obscured by dust can be detected in gamma. Therefore, taking into account that INTEGRAL has been operating during $\sim$ 20 years the probability that such an event has occurred during this period is not negligible.

In this chapter we analyse the possibility of using the anticoincidence system (ACS) of the spectrometer SPI on board of the INTEGRAL (INTErnational

Gamma-RAy Laboratory) space observatory for detecting the early gamma-ray emission of a SN Ia as a function of the explosion model and distance as well as of pointing direction. The anticoincidence system of SPI (ACS) is used not only to reduce the background of SPI but also to monitor the sky for possible sources thanks to its large field of view and its spectroscopic capabilities (Vedrenne et al., 2003a). Jean et al. (1999) proposed the use of the SPI-ACS to search for Galactic classical novae, Von Kienlin et al. (2001) to locate Gamma-Ray Bursts (GRBs), and Rodríguez-Gasén et al. (2014) to study solar flares.

The chapter is organized as follows. We make a brief introduction of INTEGRAL in section 4.1. We explain what the ACS is in Section 4.2 , this section also describes the ACS data used for this study. We present the supernova models used to simulate the detection by the ACS in section 4.3. The simulation method and the results of the analyses to estimate the sensitivity of the ACS are presented in section 4.4. In addition, to scrutinize the presence of SN Ia signature in the already recorded ACS data in Section 4.5. Finally, in section 4.6 we present the discussion of the results.

4.1 Overview of INTEGRAL

The INTErnational Gamma-Ray Astrophysics Laboratory (INTEGRAL) is an European Space Agency (ESA) mission that was launched in 2002. INTEGRAL is a hard X-ray and soft gamma-ray observatory that covers the 3 keV to 10 MeV energy band. The goal of the mission is to explore fundamental problems in physics and astrophysics that gamma-ray astronomy exhibits. The observatory is able to cover a wide range of gamma-ray phenomena such like compact objects (White Dwarfs, Neutron Stars, Black Hole Candidates, High Energy Transients), explosive nucleosynthesis (Novae and SNe), gamma-ray bursts, cosmic-ray interactions, the interstellar medium, among others.

This wide range of gamma-ray astronomy observation is achieved thanks to the two main instruments on board: IBIS and SPI. They are designed to complement each other. IBIS is the INTEGRAL imager and allows for source localisation (for a deeper view of IBIS see Ubertini et al., 2003). SPI is a gamma-ray spectrometer for lines of celestial sources in the energy range of 20 keV to 8 MeV (for a deeper view of IBIS see Vedrenne et al., 2003b). SPI is designed for high resolution spectroscopy of gamma-ray emission lines but it has a low spatial resolution compared to IBIS, which is dedicated to imaging of point sources with a larger spatial resolution but lower spectral resolution. Besides these two instruments, there are two monitor intruments that provide complementary observations in the X-ray (JJEM-X) and optical energy bands (OMC). An image of INTEGRAL with its components is shown in Figure 4.1.

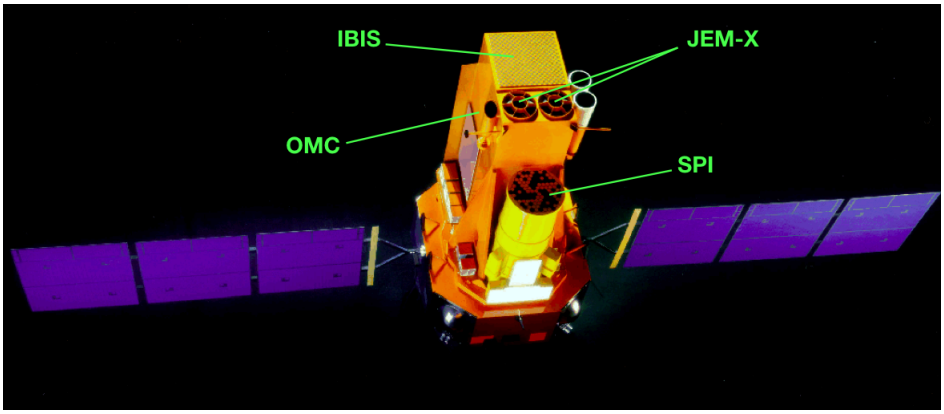

FIGURE 4.1: Image of the INTErnational Gamma-Ray Astrophysics Laboratory (INTEGRAL) with its main instruments pointed out. Source: esa website.

4.2 The anticoincidence system (ACS) of SPI

The anticoincidence system (ACS) of SPI aims first to reduce the instrumental background in the germanium detectors due to charged particles and gamma rays coming from outside the spectrometer's field of view. It is composed of an active shield made with 91 scintillator blocks[1] in bismuth germanate (BGO) and a plastic scintillator, optically coupled to photomultiplier tubes (see Von Kienlin et al., 2001, for a detailed description of the SPI ACS). When a particle releases energy in a scintillator block, a veto signal is generated and transmitted to the on-board digital acquisition system. By this way, the active shield allows to remove events produced in coincidence by particles that deposit energy in the shield and in the germanium detectors. The ACS veto rate is recorded with a sampling period of 50 ms and is sensitive to photons releasing energy 80 keV in a scintillator block. In Figure 4.2 we show a scheme of SPI where ACS is displayed together with its other main components.

The ACS of SPI is also used to monitor astrophysical sources. For instance, its large detection area allows the detection of gamma-ray bursts and it is part of the INTEGRAL burst alert system providing the gamma-ray burst location in the sky by triangulations with other space-borne gamma-ray burst monitors (Von Kienlin et al., 2001; Von Kienlin et al., 2003; Savchenko et al., 2017). A giant outburst from the soft gamma-ray repeater SGR 1806-20 was discovered in 2004 by the analysis of the ACS rate (Borkowski et al., 2004; Mereghetti et al., 2005). Rodríguez-Gasén et al. (2014) and Gros et al. (2004) explored the capabilities of the SPI ACS to study solar flares. Jean et al. (1999) proposed to use SPI ACS to search for the hard X-ray and gamma-ray emission from classical novae in our Galaxy (see also Siegert et al., 2018). For this purpose, they computed the effective area of the SPI ACS with GEANT 3 for energies ranging from 80 keV to 500 keV and a rough angular binning.

[1] Only 89 blocks are active (see Savchenko et al., 2012)

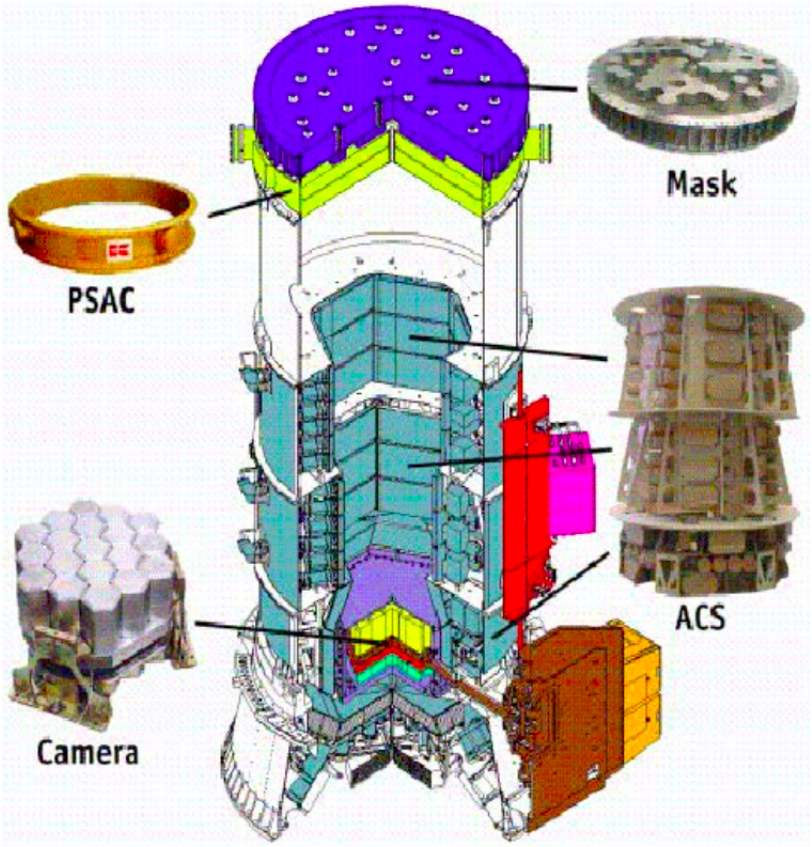

FIGURE 4.2: Scheme of SPI (INTEGRAL gamma-ray spectrometer) showing its main components. Source: Diehl et al., 2018.

For the present study, we re-calculated the response of the SPI ACS with GEANT 4, using the same INTEGRAL mass model, for energies ranging from 80 keV to 3.5 MeV and with a binning of 10 degrees for the zenithal and azimuthal angles (see Fig. 4.6). The values of the effective area obtained in this way are in agreement with the ones calculated by Rodríguez-Gasén et al. (2014) (e.g. differences are less than 5%).

The anticoincidence system of SPI provides also the saturating event rate, defined as the rate of events released in the BGO blocks with energy 150 MeV. The ACS saturating event rate, unlike the ACS rate, is not affected by low energy particles from the radiation belt, from solar flares or from gamma-ray sources that emit mainly in the low energy gamma-ray range (i.e. $E < 100$ MeV). Consequently, that makes it a good tracer for monitoring the cosmic-ray intensity at the spacecraft level. When the spacecraft is not affected by these low energy events, the temporal behaviour of the ACS saturating rate is concordant with the total ACS rate. Figure 4.3 shows the average ACS rates and the average ACS saturating rates for some revolutions since the launch of INTEGRAL. In order to avoid the effects of radiation belts, the rates shown are the rates averaged over the first to the third quarter of each revolution. Figure 4.3 shows that the total and saturating rates follow a linear relation, although the linear coefficients may slightly change due to slight changes of the high energy

particle spectrum impinging the ACS. The saturating rate can be therefore used to trace the variation of the ACS rate without source contribution and be used as background model to our study (see section 4.4.2).

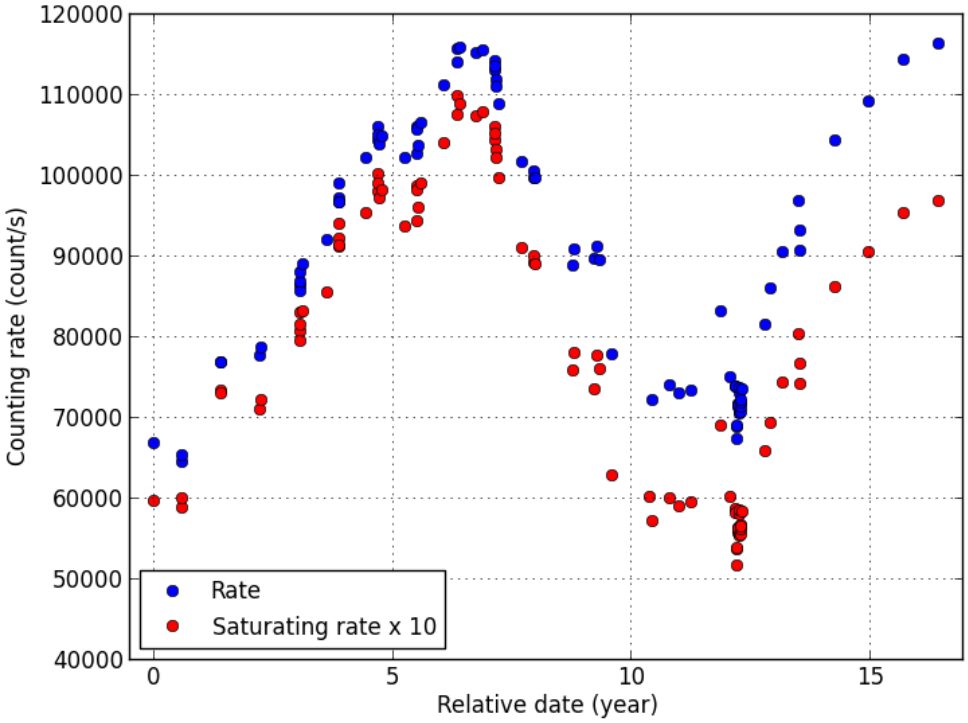

FIGURE 4.3: Total and saturating event rates of the anticoincidence system of SPI averaged for some revolutions since the launch of INTEGRAL.

4.3 Supernova models

Two models, DDTe and W7, of SN Ia have been used for testing the possibility of detection by ACS/SPI. The spectra as a function of time of these models were obtained with 1D simulations as in Gomez-Gomar et al. (1998). These models were compared with those obtained from SN 2011fe and SN 2014J by the instruments on board of INTEGRAL (Isern et al., 2013; Isern et al., 2014). Both are compatible with the upper limits deduced for SN 2011fe but the SN 2014J case demands further considerations since the early spectra presented some features that were better interpreted introducing non-spherical structures.

The DDTe is a sub-luminous SN Ia model. It describes a situation in which the burning front starts as a deflagration that turns out into a detonation when reaches a critical density. As a result, material is processed into Fe-group and into intermediate-mass elements. This model ejects 0.51 $M_\odot$ of ^{56}Ni with a kinetic energy of 1.09 $\times$ 10^{51} ergs. The W7 model is a normal luminous SN Ia model (Nomoto et al., 1984). In this model a flame ignited near the center

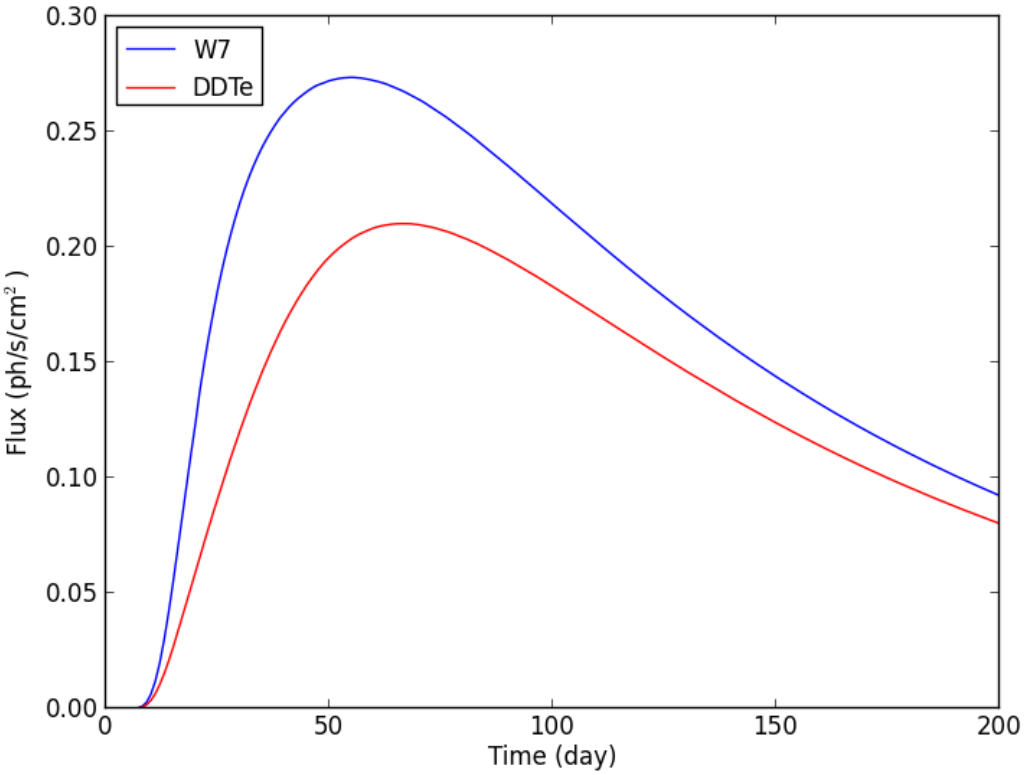

FIGURE 4.4: Gamma-ray flux variation for model W7 (blue) and DDTe (red) at a distance of 8 kpc from day 5th to 200th after the explosion.

propagates subsonically, thus allowing the expansion of the star and leaving some unburnt material. The W7 model, in particular, is characterized by a small portion of unburnt C-O and a large mass of burnt intermediate-mass elements. This model ejects 0.56 $M_\odot$ of ^{56}Ni with a kinetic energy of 1.24 $\times$ 10^{51} ergs. Figure 4.4 displays the light curve of both models for SN Ia at 8 kpc. They have been obtained by integrating the spectrum models from 6 keV to 3684 keV for a SN Ia at 8 kpc.

Figure 4.5 displays the gamma-ray spectra of both models in a logarithmic scale during the 9th day after the explosion. Even at such early stages the 750 keV and 812 keV ^{56}Ni lines decay are visible including several features from the ^{56}Co decay.

The slow rising signal of the DDTe model as compared to that of W7 is a convenient property for exploring if the differences in luminosity have an impact on the detection sensitivity. In order to analyse the detection sensitivity as a function of SN Ia distance, models were placed at distances in a range of 4 kpc to 16 kpc. For each model the output flux is provided with an energy resolution of 0.5 keV, in the interval 6 keV to 3684 keV. The spectra were calculated with a frequency of one day from days 5 to 200 after the explosion, although just the spectra derived for the first days were used and interpolated, as the main goal

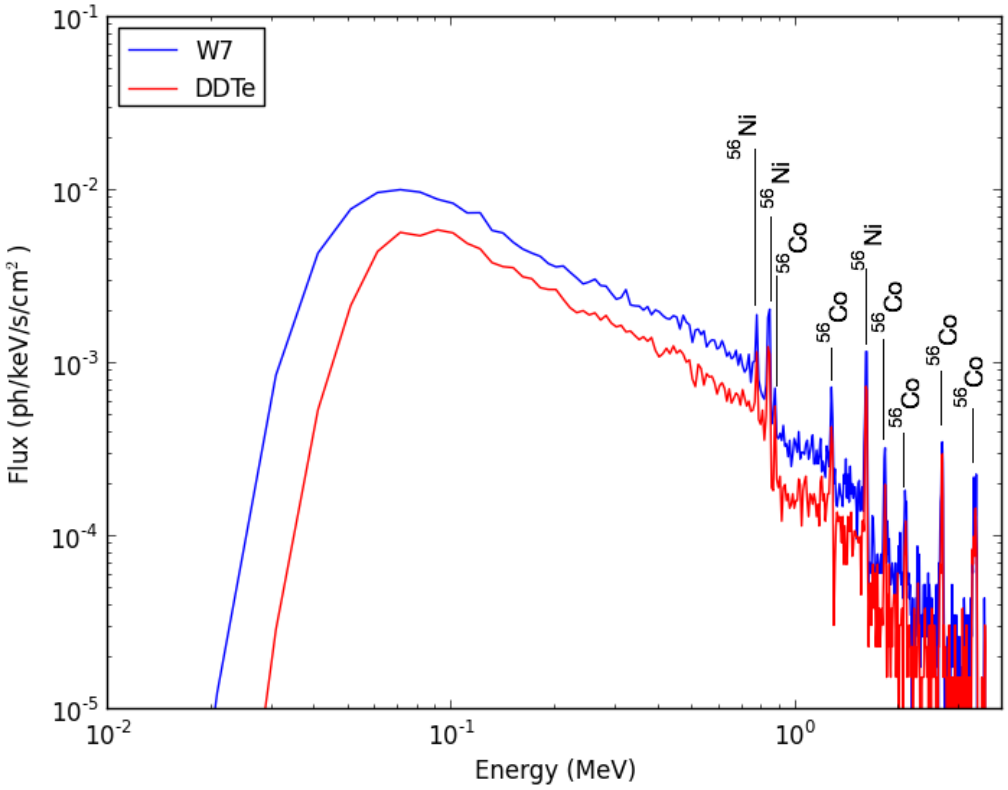

FIGURE 4.5: Gamma-ray spectra for day 9th of the models, W7 (blue) and DDTe (red) at 8 kpc. A label on top of each line is added to indicate if they are from ^{56}Ni or ^{56}Co decay.

is to study the detection of the rising signal as soon as possible. For further details about the models data preparation see section 4.4.

4.4 Simulations and analyses

4.4.1 Simulated count rate

The count rate (CR), counts per second, from a source located at a zenithal and azimuthal angles θ and φ in the SPI frame at the instant t can be defined as:

$$R_{\rm sn}(t) = \sum_{E_i} F(E_i, t) \cdot S_{eff}[E_i, \theta(t), \varphi(t)] \cdot \Delta E \tag{4.1}$$

where $F(E_i, t)$ (counts/cm^2/s/keV) is the flux for a given energy and time, $S_{eff}[E_i, \theta(t), \varphi(t)]$ is the effective area (cm^2 – i.e. the response matrix) of the ACS and ΔE is the size of the energy bin (keV) of the spectrum. Overall it provides the rate in counts/s, $R_{\rm sn}$, that would be produced by a SN model. Two SN Ia models (see section 4.3) have been simulated, the W7 model and a delayed detonation model (DDTe), with an energy binning of 0.5 keV and a

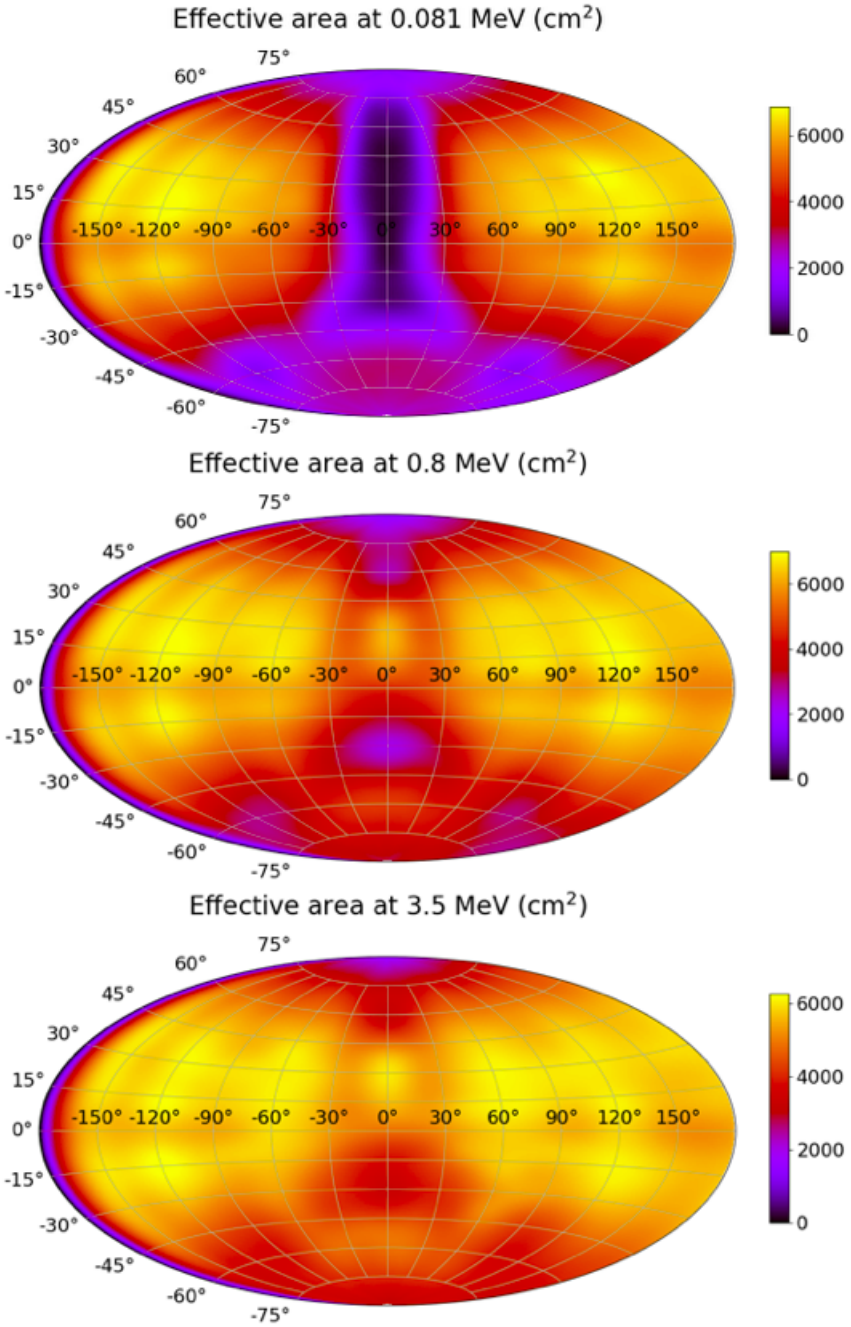

FIGURE 4.6: Effective area (cm^2) of SPI for energies of 0.081, 0.8 and 3.5 MeV for all pointing directions in the sky. The effective area is lower for regions where $z = 0°$ and the energies are low, this is due to SPI being masked by IBIS.

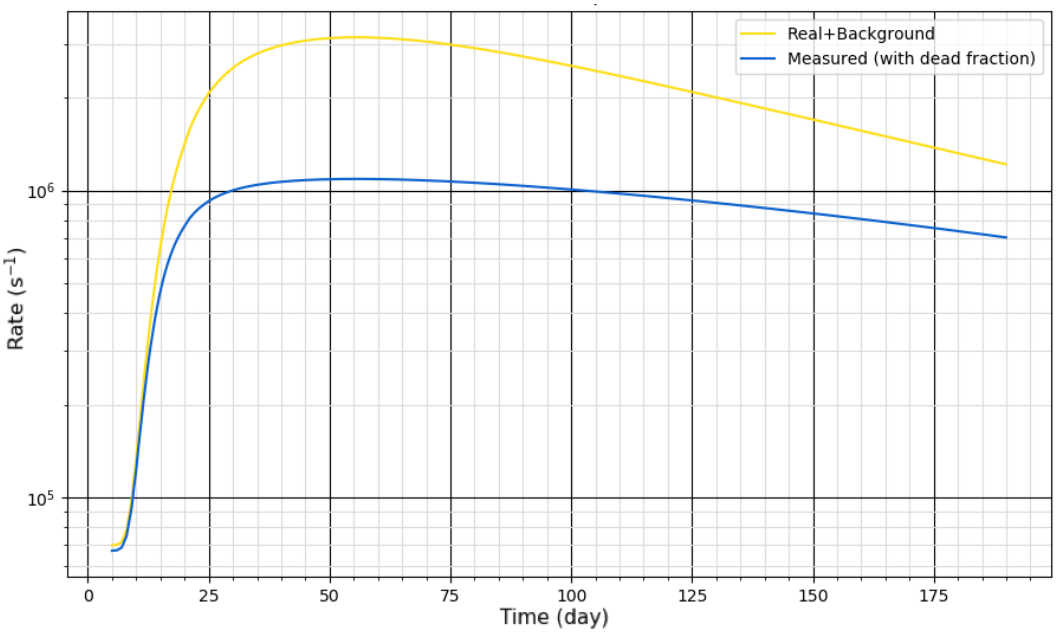

FIGURE 4.7: Count rate for model DDTe at 6.4 kpc before (yellow) and after (blue) taking into account the dead time of the ACS.

time binning of 80 s to provide enough resolution. Furthermore, the models have been scaled to Galactic distances: 4, 6, 8, 10, 12, 14 and 16 kpc.

The response matrix has been computed by Monte Carlo simulations (see Section 4.2). It gives the effective area for energies in the range of 81 keV to 3.5 MeV, with an azimuthal resolution of 20° and a zenithal resolution of 10°.

An interpolation of the response matrix is used to take into account the influence of the pointing variation during each revolution on the effective area for each energy event reaching the satellite. INTEGRAL provides for each revolution the right ascension (RA) and declination (Dec) of the x axis of the instrument and the RA and Dec of the z axis. For running the tests we fix the RA and Dec of the simulated source and we take into account the angular evolution of the source with respect to the x and z axis of the instrument to obtain the local coordinates and finally the effective area.

INTEGRAL provides the ACS data along the lifetime of the satellite for each orbital revolution. The ACS rate from a chosen revolution is added as a background to the SN model to make the simulated count rate realistic. Each revolution has a duration between 2 to 3 days and the time of each revolution (and the SN model) is binned in intervals of 80 s. Before adding the ACS rate to the SN model rate, the first one needs to be converted from measured rate to true rate by taking into account the dead time δt of 0.6 μs (Savchenko et al., 2012):

$$R_{\mathrm{bck}} = \frac{R_{\mathrm{m}}}{R_{\mathrm{m}} \cdot \delta t - 1} \tag{4.2}$$

where $R_{\rm bck}$ is the true background rate and $R_{\rm m}$ the measured rate extracted from the data. The rate $R_{\rm sn}$ produced by the SN Ia, computed with equation (4.1), is added to the true background rate to yield to the total rate $R_{\rm tot}$. The final simulated rate $R_{\rm sim}$ is obtained with:

$$R_{\rm sim} = \frac{R_{\rm tot}}{1 + R_{\rm tot} \cdot \delta t} \tag{4.3}$$

to take into account the dead time of the ACS.

4.4.2 Detection of the supernova signal

Once the ACS rate produced by the supernova is simulated, we aim to study the sensitivity of the SPI ACS to detect the earliest gamma-ray signature of our SN models within a galactic distance. Two methods have been tested.

ON/OFF method (rejected)

The first method consist of an 'ON/OFF'. It analyses a previous window (or interval) in the data, called the 'off' window which represents a null hypothesis, and the subsequent window with the same size, the 'on' window that represents an hypothetical source (Li and Ma, 1983). The method is illustrated in Figure 4.8.

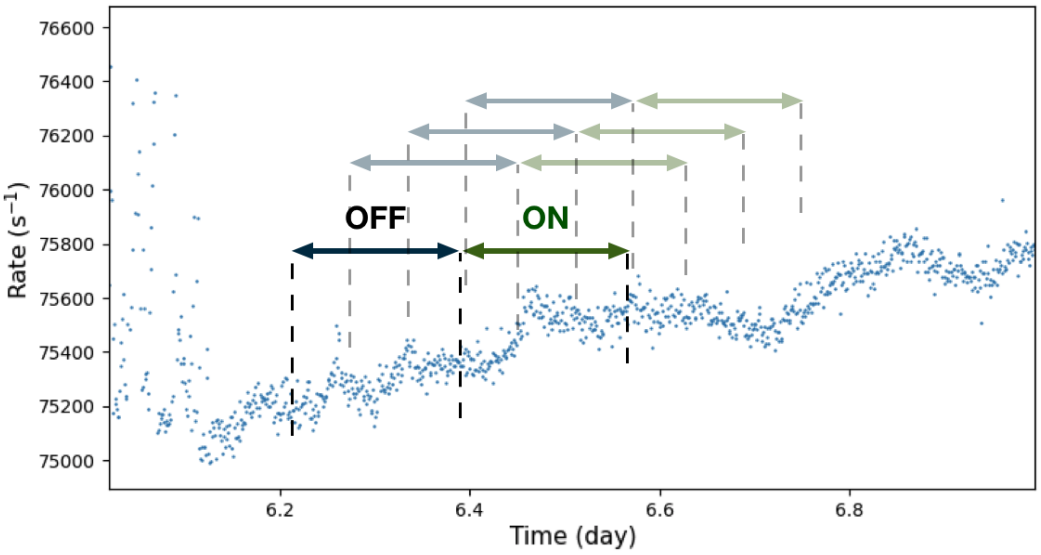

FIGURE 4.8: Illustration of the ON/OFF method.

A rising of significance is expected when the "on" window have a rapid increase of flux compared to the previous "off" window. The significance s is computed as:

$$s = \frac{\bar{r}_{on} - \bar{r}_{off}}{\sqrt{\sigma_{on}^2 + \sigma_{off}^2}} \tag{4.4}$$

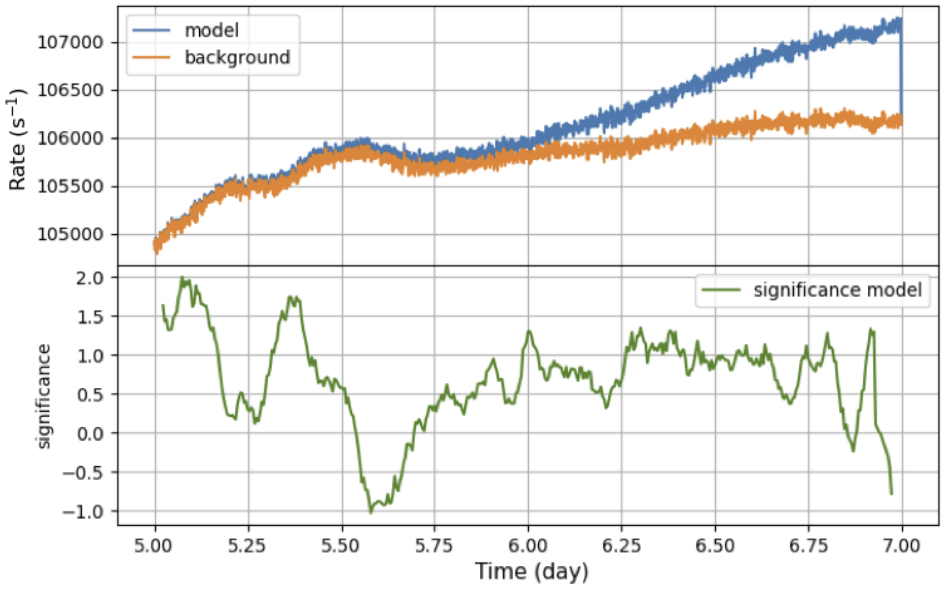

(A)

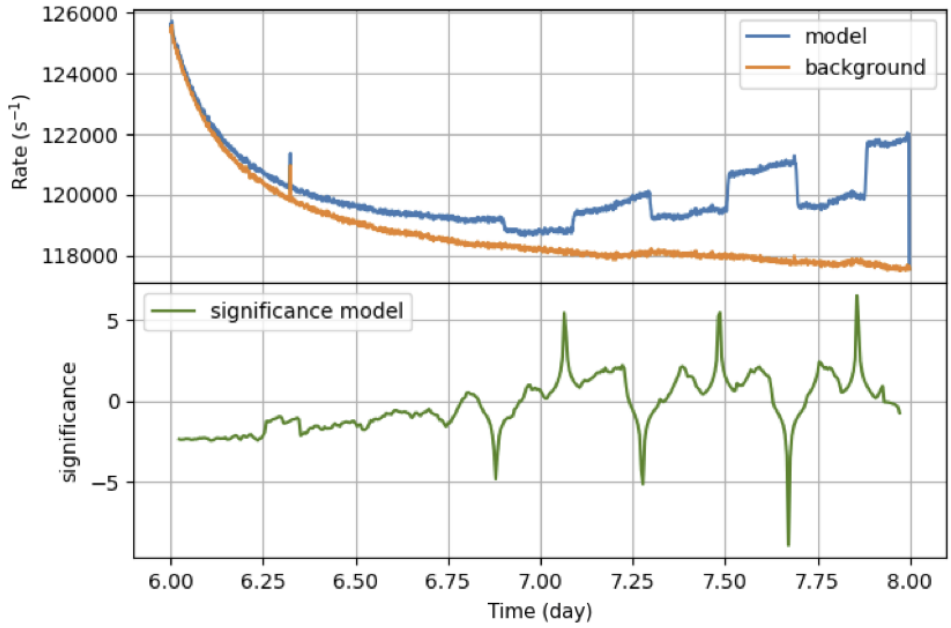

(B)

FIGURE 4.9: (a) On top we show the count rate for the SN model (in blue) and the background (in orange) for revolution 600 from day 5 to 7. In the bottom we show the significance of each on/off window (in green). (b) Same as (a) for revolution 2150 from day 6 to 8.

where $\bar{r}_{on}$ and $\bar{r}_{off}$ are the mean rate values of the on and off windows and σ_{on} and σ_{off} their standard deviations.

The process is made along all the count rate data in a given revolution and it has the goal to detect the very first rising of the flux of the supernova. Some examples using this method are shown in Figure 4.9a and 4.9b using revolution number 0600 and number 2150, respectively, with the DDT model with background at 6.4 kpc as supernova model. Figure 4.9a shows day 5th to 7th of the supernova model (blue line), the measured count rate of the satellite for the given revolution (orange line) and the significance of the count rate of the supernova model (green line). Figure 4.9b shows the same but for day 6th to 8th for revolution number 2150. Although the measured background rate line (in orange) is not used for the calculation of the significance shown in this figures, it is left on the plots to show where the supernova stars to rise and if our method is able to find it. The ON/OFF method has been applied considering the off and on window of the same size, using 50 data points of count rate data each (the binning of the count rate data is of 80 seconds, making a window of 50 data points equivalent to 67 minutes). We apply the off and on window every 5 data points along all the count rate data. From those plots we can observe that for revolutions such as number 600, where the count rate plot is smooth, the method has a hard time to find the early rise of model. In the other hand, in revolution 2150, this method seems to be subject to high spikes of significances when the satellite makes a sudden change of orientation, which produces a different amount of count rate, but it is not able to detect the rising of the supernova model.

Finally, we have computed the significance of the background of each revolution, besides the significance of the supernova model, to make a comparison of the values of maximum significances of each test for the model count rate and for the background count rate. As seen in Figure 4.10 there is not an outstanding difference of significance between the supernova model (blue dots) and background (red dots). Therefore, we conclude this method is not valid for our study.

Selected method

The second method estimates the detection of the rising signal of the supernova by fitting the intensity of the supernova rate and the parameters of a background rate model to the SPI/ACS data. This method takes into account two assumptions. The first one considers that the background rate model (r_{bck}) is a linear function of the ACS saturating (R_{sat}) event rate :

$$r_{\mathrm{bck}} = \frac{R_{\mathrm{sat}} - c}{f} \tag{4.5}$$

with c and f as free parameters. The saturating event rate (rate ACS saturating) is the rate of events with energy released in the BGO blocks with energies 150 MeV (see section 4.2). The second assumption is that the rate produced

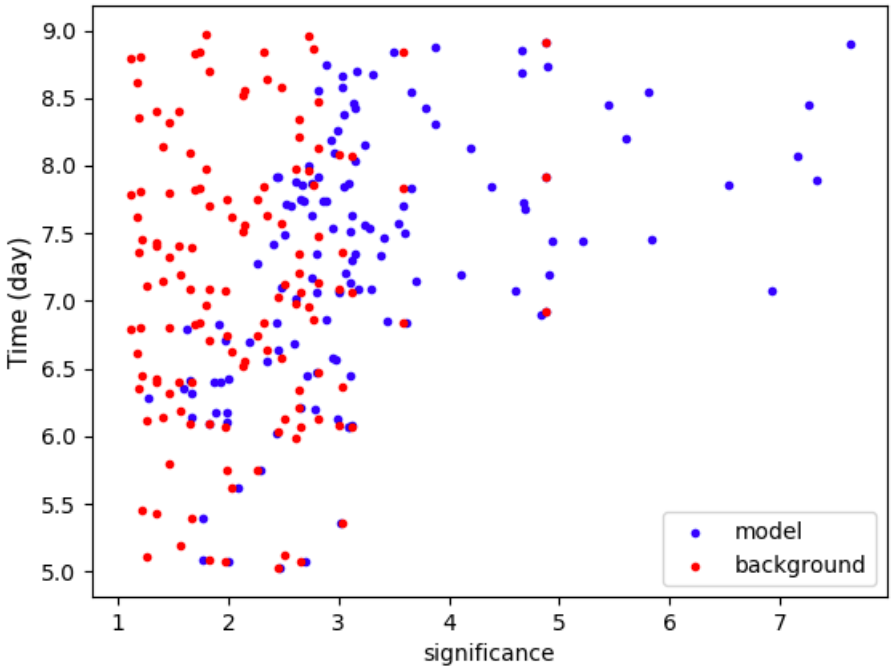

FIGURE 4.10: Mean significance, using the ON/OFF method, of the discovery date for multiple SN models (blue) versus the mean significance for each of the backgrounds for these models (red).

by the rising gamma-ray flux of the supernova can be described as the following power law:

$$r_{\mathrm{sn}} = I \cdot (t/5)^{\beta} \tag{4.6}$$

Where I is the intensity and t is the time of the model. Both are free parameters. The power law model is justified by the shape of the gamma-ray light curves when the emission is rising (see Fig.4.4). The slope of the power law β is equal to 18.9 for the W7 model and 14 for the DDTe one, see Figures 4.11a and 4.11b. These two different values of the slope does not impact very much on the results.

With these two assumptions we obtain a total model $r_{\mathrm{mod}} = r_{\mathrm{bck}} + r_{\mathrm{sn}}$, where r_{bck} is the background model (see Eq. 4.5) and r_{sn} is the supernova signal model (see Eq. 4.6). The best fitting parameters (I, c and f) are the ones that minimize the chi square calculated as:

$$\chi^2 = \sum \left(\frac{R_{\mathrm{sim}} - r_{\mathrm{mod}}(I, c, f)}{\sigma_{\mathrm{acs}}} \right)^2 + 10\,(f - f_0)^2 + \left(\frac{c}{2000} \right)^2 \tag{4.7}$$

where R_{sim} is the simulated ACS rate (see Eq. 4.3) and σ_{acs} the standard deviation of the model and the ACS data. The second and third terms in the sum are penalty functions that avoid wrong best fitting values of the parameters f and c. Without those penalty functions, the minimization process could converge toward local chi square minimum yielding to abnormal values of the parameters of the background model, f and c. It sometimes occurs when the

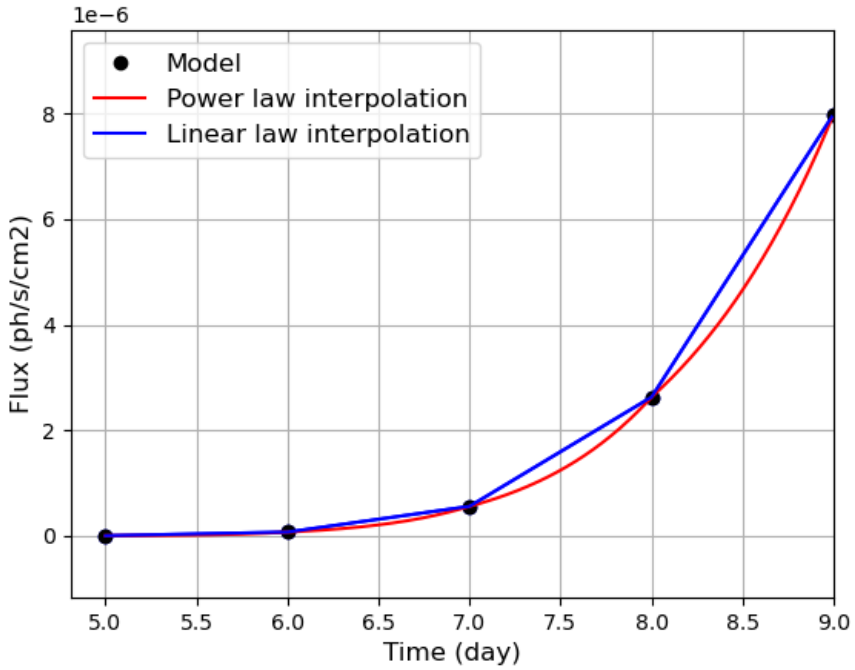

(A)

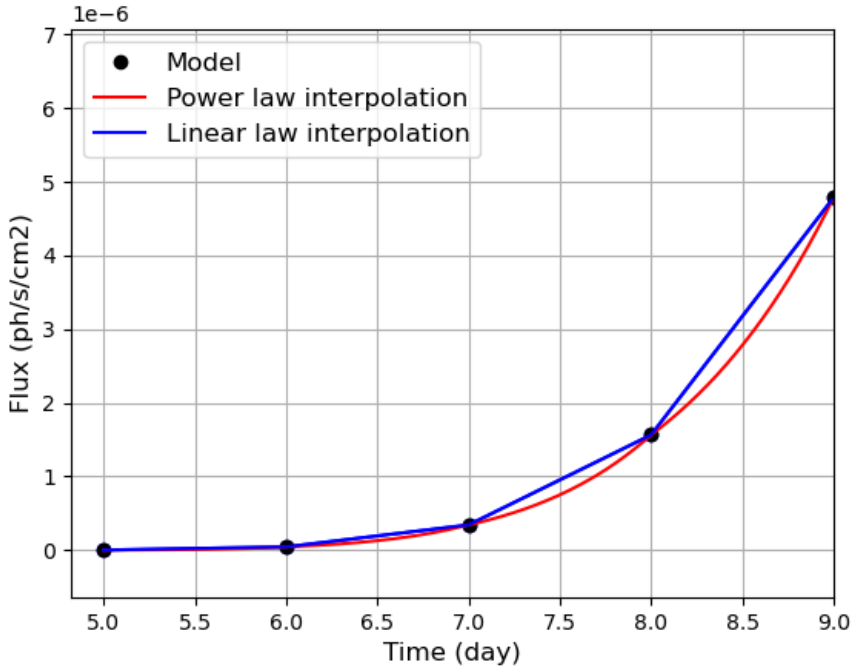

(B)

FIGURE 4.11: (A) Power law (in red) with a slope of 18.9 fitting the data points of the first days of W7 SN model (black dots), For comparison we show the linear interpolation of the data points (in blue). (B) As in (A) but for DDTe SN model.

signal of the supernova is strong. The parameter f_0 in Eq. 4.7 is an estimated mean value of the factor that scales the ACS total rate with the ACS saturated rate (see Fig. 4.3 and section 4.2).

From these results we can estimate the detection date. To do so, we estimate first the quality of the background model (r_{bck}) computing a residual (δ):

$$\delta = \frac{R_{\mathrm{sim}} - r_{\mathrm{bck}}}{\sigma_{\mathrm{acs}}} \tag{4.8}$$

Then, this residual is smoothed to avoid a false detection due to a single short time scale spike in the data.

We consider that the supernova signal is detected when the following conditions are satisfied: 1) $\mathrm{t_{acs}} > \mathrm{t_{start}} + 0.5$ day; 2) $\delta > 3$. Where $\mathrm{t_{acs}}$ is the time of the data, the sigma level is set to 3, and $\mathrm{t_{start}}$ is the date at which the ACS data starts to be recorded at the beginning of an orbital revolution of INTEGRAL. The addition of half a day in the first condition aims to remove significant count rate excess induced by high energy particles when INTEGRAL goes out of the radiation belts, after its perigee.

This procedure is done to test the DDTe SN model and the W7 SN model over 275 revolutions. These revolutions have been taken along the lifetime of INTEGRAL to find the earliest time of detection. Each of them have the following available data: ACS rate, ACS saturating rate, rate time, right ascension and declination of the INTEGRAL X-axis, right ascension and declination of the INTEGRAL Z-axis. The ACS rate is used as simulated background to the models, as mentioned in section 4.4.1. The ACS saturating event rate is used on this analysis to estimate the background ACS rate and detect the supernova signal, as mentioned previously in this section. Each revolution has a length of 2 to 3 days that we fixed to ≈2 days as we cut the initial hours of data because most of them still contain some noise from the radiation belt phase[2]. A same length of the supernova model is cut in order to compute the simulated count rate. The initial time of the computed count rate equals to a time ranging from day 4th to 6th of the SN Ia model, for earlier days the flux's model is not high enough to make a contribution to the ACS rate. This initial time, from 4th to 6th, is chosen randomly to give more realistic circumstances to the analysis.

When the count rate with a length of 2 days is analyzed two things may happen: a supernova signal detection is found or not. If a detection is found in the count rate then the revolution number, the time detection and its significance are saved. In case it is not, we proceed to analyze the consecutive 2 days of the computed count rate, which would account for the 2 following days of the SN Ia model and using the subsequent revolution as its background. This procedure is repeated until a detection is found or until we reach an initial time of the count rate higher than the 10th of the SN Ia model. When this point is reached, we start again the process with an initial count rate time ranging from 4th to 6th but with a different revolution as background and so on. An example output of

[2]SPI is switched off between revolutions

this method is shown in Figure 4.12, where the count rate is computed using the DDTe model with revolution number 1752. The computed discovery date is at 6.73 day with $\approx 67\sigma$, which is coherent if we make a visual evaluation of the count rate data.

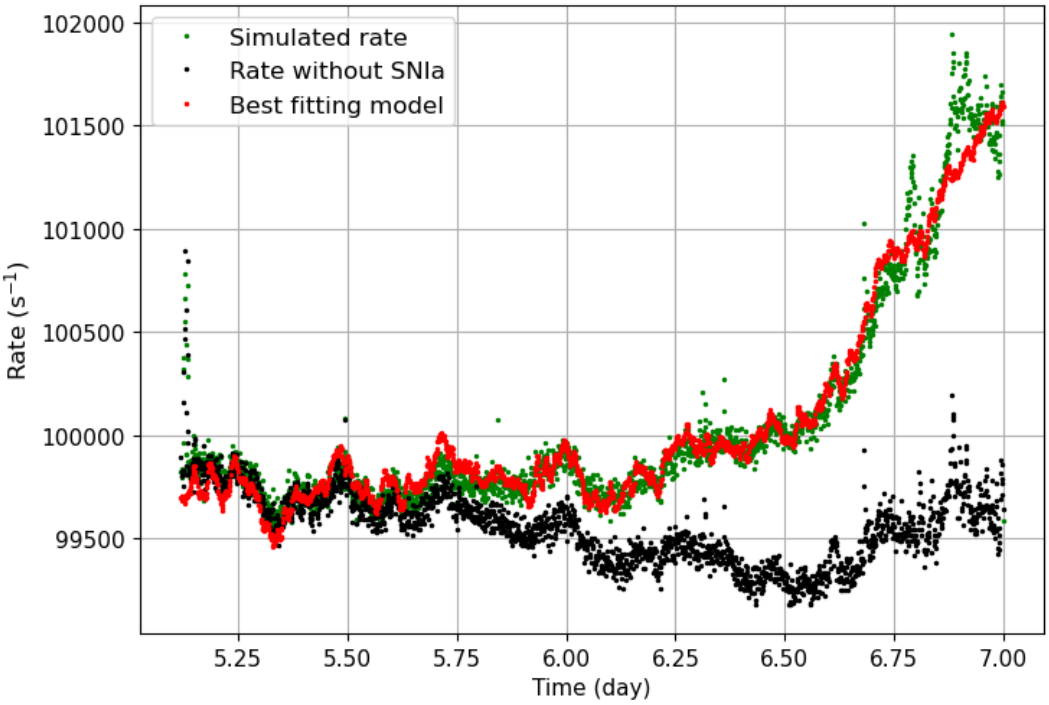

FIGURE 4.12: Display of the SN model rate with revolution number 1752 added as background in green. The background rate, without the SN signal, is shown in black. The best fitting model to the SN with background rate is shown in red. For this example, the rising of the SN rate is appreciated and allows the detection time to be at 6.73 day.

In some cases, due to high background or too many changes on pointing direction in the same revolution, the rising of the SN model goes undetected but on the following revolution, as the SN model flux is higher with time, the flux is too high to find a good fit. In these cases an inspection of the data makes clear that there is a high rising signal and the satellite would recognize it as such. We want to count these cases as late detections, therefore a condition is created where, if the maximum of the SN Ia signal is larger than 8.5% of the mean ACS rate, the detection time is saved even if the fit is not good enough.

The analysis of the count rate has been performed for each of the models (DDTe and W7) for distances of 4, 6, 8, 10, 12, 14 and 16 kpc. For each distance and model several pointing directions have been tested to reproduce different galactic areas backgrounds and to check the variability of the detection on different positions in the Galaxy. The pointing directions, in galactic coordinates of longitude (l) and latitude (b), are l = 0, 45, 90 and 180 deg for b = 0 deg. All the position have a same value of latitude of b = 0 deg. The reason for this fixed

latitude is that the location for these events in our galaxy would be in regions of old population stars, which are in the old disk and in a spheroid centered to the galactic center. Therefore, they would likely occur at ± 15 deg from the galactic plane. As seen in Figure 4.6, the response of the ACS does not change significantly with the direction of the source (except for low energies). Hence, simplifying the latitude to b = 0 deg is good enough for our study.

4.4.3 Results

Following the methodology explained on the "Selected Method" in Section 4.4.2, the time detection for the W7 and DDTe models placed at distances of 4, 6, 8, 10, 12, 14 and 16 kpc and at positions l = 0, 45, 90 and 180 deg with b = 0 deg has been computed.

We show an example of the distribution of discovery dates for models W7 and DDTe in Figure 4.13, top and bottom respectively. The distributions are for distances of 4 kpc (in red) and 16 kpc (in black) to show the difference between the closest and furthest distance. They are set to direction l = 0 deg and b = 0 deg. For both models we can see that the number of detections for higher distances is lower due to the lower flux.

From the discovery date distribution, we compute their mean value for all distances and pointing directions. See Figure 4.14 for the W7 model and Figure 4.15 for the DDT model. We show the relation between the discovery date and each distance in the top plots of Figure 4.14 and 4.15. The time of the early signal detection for each distance is coherent with the flux $\propto$ distance^{-2} relation, as for further distances the detections are later due to lower flux. The W7 model has a slightly earlier detection for each case because its flux rises faster than compared to the DDTe one.

In the bottom plots of Figure 4.14 and 4.15 we show the relation between the discovery date and the direction. We can see how the position of the source is not relevant for the early detection of the model, as it does not change for each longitude tested. These results are due to the fact that INTEGRAL observatory has been pointing in various directions during the $\sim$15 years of observation and that the equivalent field of view of the ACS/SPI is very large, therefore the position of a SN Ia in the sky does not show any effect.

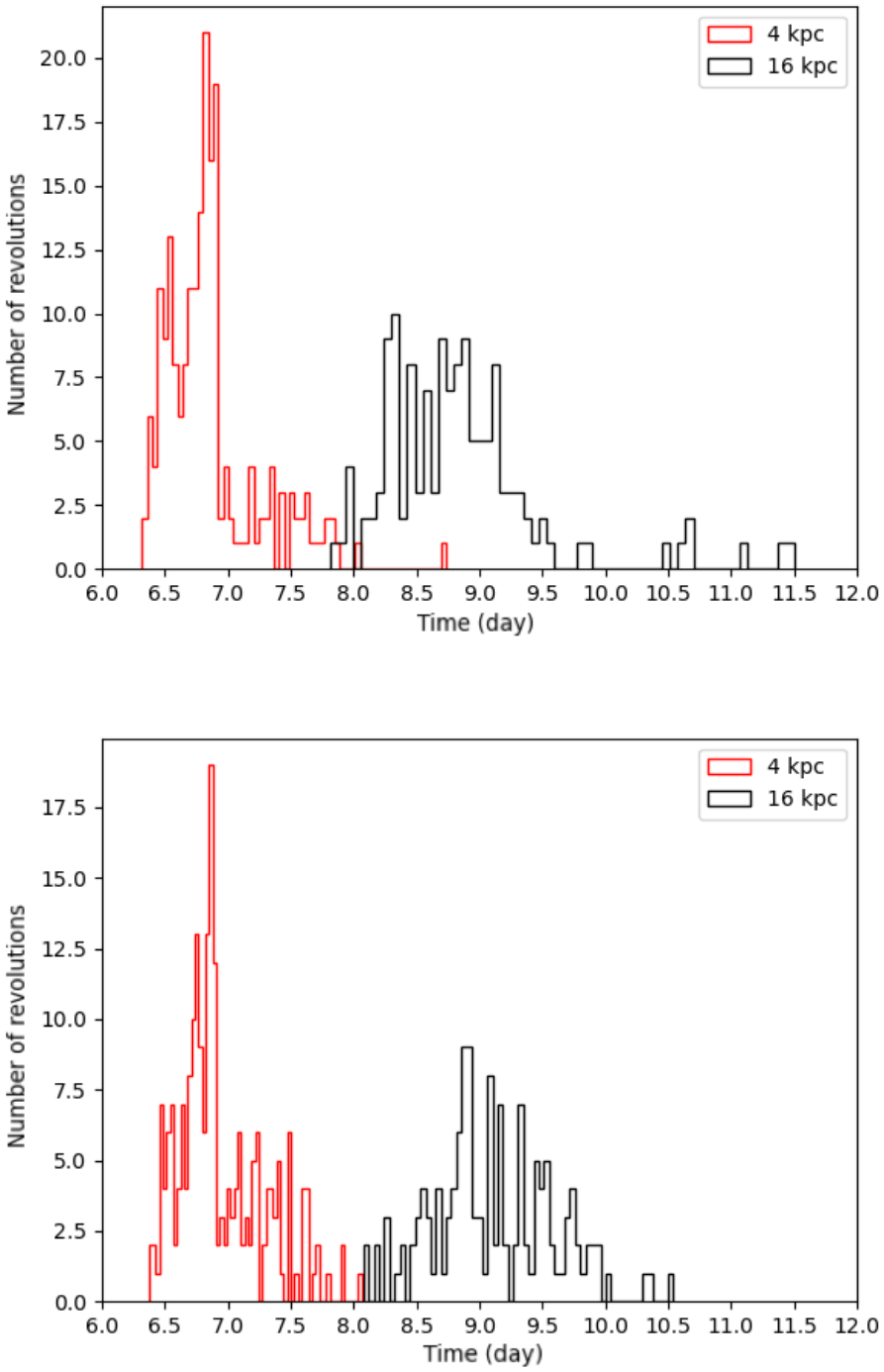

FIGURE 4.13: Top panel shows the distribution of the discovery dates for the W7 model at l = 0 deg and b = 0 deg for distances of 4 kpc (red) and 16 kpc (black). Bottom panel displays the same for the DDTe model.

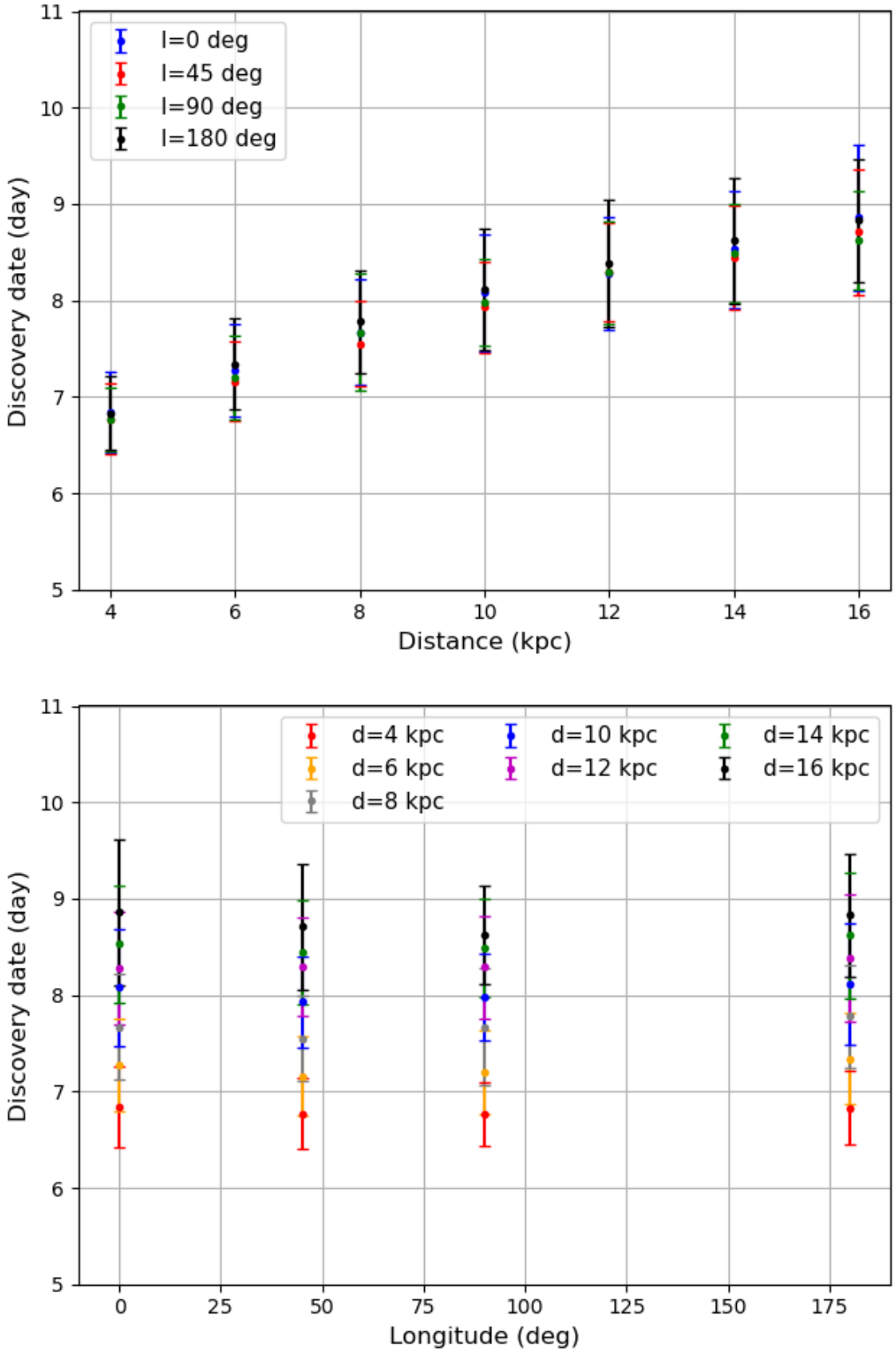

FIGURE 4.14: Mean discovery dates versus distance for model W7 (top panel) and longitude (bottom panel).

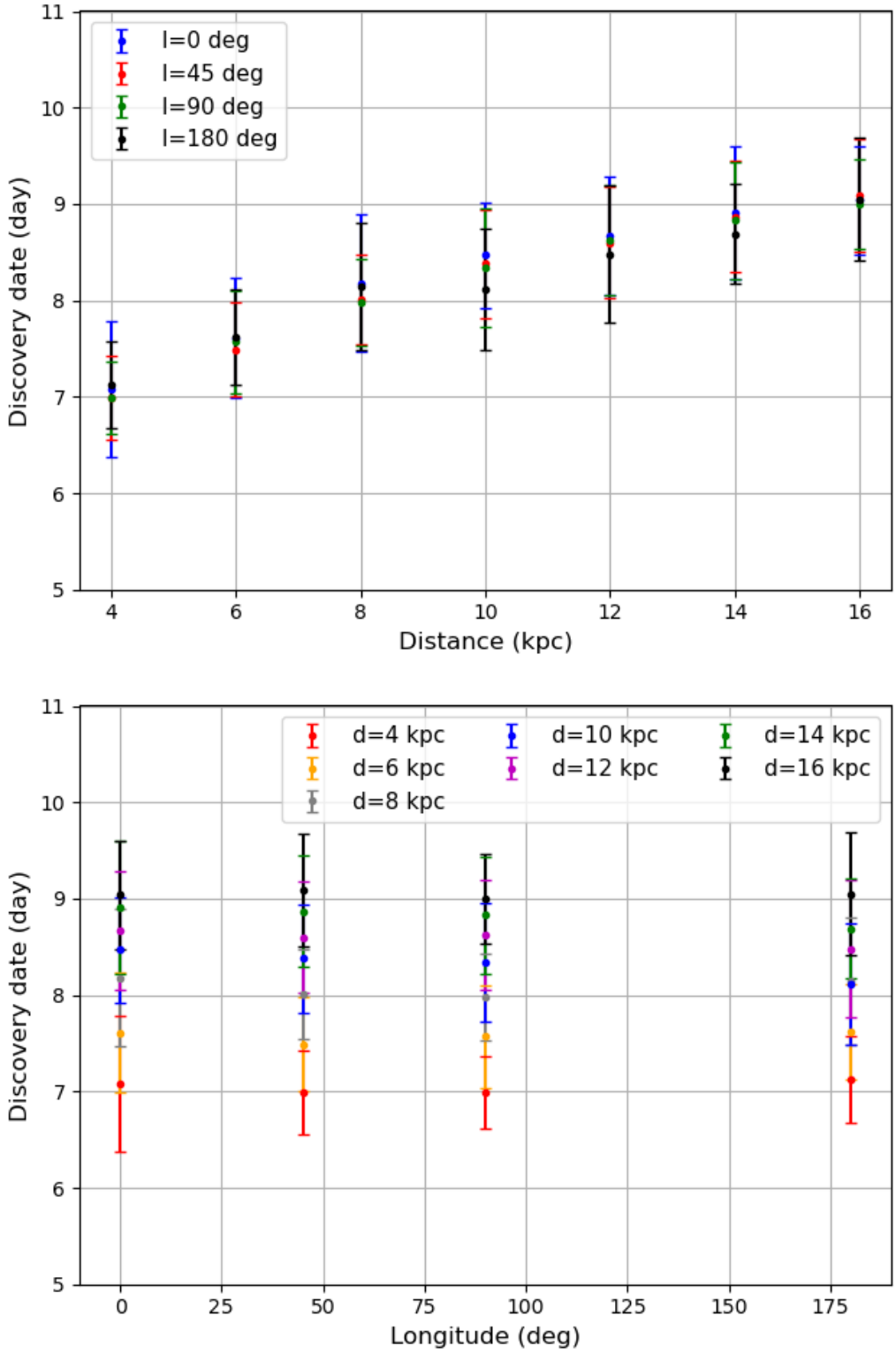

FIGURE 4.15: Mean discovery dates versus distance for model DDTe (top panel) and longitude (bottom panel).

4.5 Search of SN Ia signature in the SPI/ACS data

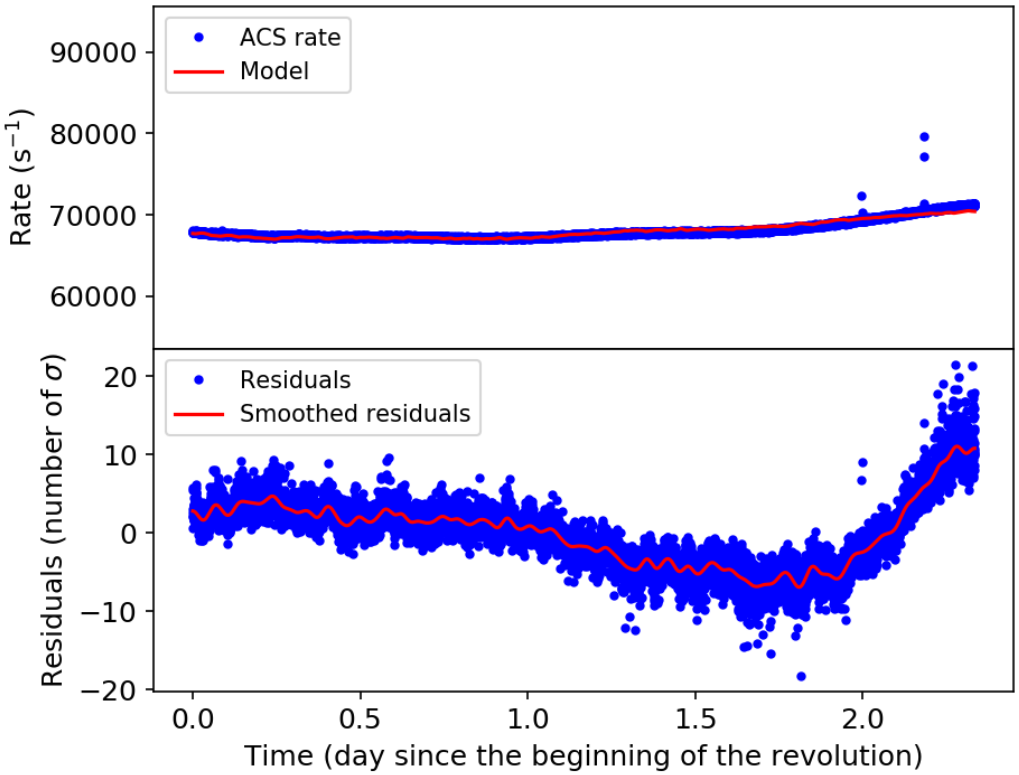

FIGURE 4.16: Example of measured and modelled ACS rates (top) and the residuals (bottom) for the revolution 1342. The imperfect modeling of the ACS rate at the end of the revolution, when INTEGRAL enters into radiation belts, produces a smoothed residual excess larger than 5σ.

We performed a systematic search for a SN Ia signature in the ACS rate with the data available at the date of the analysis: 1868 revolutions from revolution 26 to revolution 2063. The analyses were made for each revolution using ACS data rebinned with a sampling period of 18 s. The detection of a SN Ia signature is triggered when the smoothed residuals[3] obtained after subtraction of the background model (see section 4.2), are larger than 5σ up to the end of the analyzed revolution. This criterion, which was chosen for its simplicity, allows the detection of a flux rising with a long timescale as to the one expected from a SN Ia (e.g. see Fig. 4.12). A first analysis of all data yielded to a lot of detection due to background variations, which spans up to the end of a revolution, that were not well modeled with the ACS saturating event rate. Those background variations are due to low energy particles of the radiation belt or from solar events. The signature of such particles are clearly seen in the data of the INTEGRAL Radiation Environment Monitor (IREM), which measures the flux

[3]The residuals were smoothed with a hanning window of 1.5 h to reduce the number of detection due to gamma-ray bursts and false detection due to statistical fluctuations.

of particles with energy > 0.5 MeV for electron and 10 MeV for proton (Hajdas et al., 2003). The counter TC3 of the IREM reproduces well the variations of ACS rate produced by low energy charged particles of radiation belts. In order to reduce the number of detections due to low energy particles, we added the rate of the TC3 counter in the background model for this specific analysis.

With such a detection method, we counted 58 revolutions with SN Ia signature. However, all of them are detected at dates larger than ~ 2.2 days after the beginning of the revolution. These excesses are explained by an imperfect modelling of the enhancement of the rate produced by low energy particles impinging on the scintillators of the ACS when INTEGRAL enters into the radiation belt at the end of its orbital revolutions (e.g. see Figure 4.16).

4.6 Discussion

This study demonstrates the capability of the ACS/SPI to detect a galactic supernova during its early stages. Two theoretical SN Ia models with different luminosities rising times, W7 and DDTe, have been used in order to evaluate the influence on the time of the detection. For such purpose we have developed a method to detect the signature of the rising flux emitted by a supernova and to derive a detection date as quickly as possible. Using simulations of the count rate produced by the source models and the measured background ACS rates of 275 orbital revolutions of INTEGRAL, we have found that our method allows to discover a galactic SN as soon as 6 days up to 12 days after explosion, depending of the distance and model.

The simulated sources have been placed at several distances (from 4 to 16 kpc), several galactic longitudes and zero latitude. The discovery date increases with the distance, as the flux of the modelled sources is smaller. This result follows the distance flux relationship. On the other hand, the galactic longitude of the source has no influence on the discovery date, which is logical taking into account the large field of view of the ACS/SPI.

As the discovery date depends on the flux, we have found there is a slightly different range of discovery dates for the two models. The DDTe model is a sub-luminous SN Ia model and the W7 a normal luminous one. The lower luminosity of the DDTe resulted in a detection range of approximately half-day later than the W7. Using our detection method we have analyzed all the available ACS/SPI data from the beginning of the INTEGRAL mission to now and we have not found any signature of a galactic SN Ia, suggesting no event has been missed.

This method is not able to provide a position of a source but it can provide an early alert to activate other in orbit or ground-based observatories to quickly browse the sky in search for it. In any case, the collected data would provide very important information about the early development of the supernova outburst no matter if the event is detectable in any other energy range. INTEGRAL is on its last stages of life and the results obtained here suggest that future

missions should consider the possibility of using the ACS as an all sky detector by improving as much as possible its sensitivity. The new space telescope COSI, which is expected to launch in 2025, will observe the gamma-ray sky in the 200 keV - 5 MeV range (Tomsick and COSI Collaboration, 2022). It will be equipped of a compact Compton telescope made with germanium detectors and of an anticoincidence system made with BGO scintillators as for SPI. With its large field of view ($\sim$ 25% of the sky) and its pointing strategy, COSI will monitor the entire sky within a day. Both the Compton telescope and the anticoincidence system will be sensitive to the gamma-ray emission of a galactic SN Ia.

Conclusions

Throughout this thesis we have shown the importance of gamma-ray emission as a diagnostic tool of the explosion mechanism associated with thermonuclear supernovae. This has been demonstrated through a 3D gamma-ray transfer code for modelling SNe Ia based on the Monte-Carlo method technique and following the approach by Lucy of indivisible energy packets (Lucy, 2005). The code allows us to synthesise gamma-ray light curves and spectra of SNe Ia by simulating the behaviour and evolution of gamma photons within the domain of the supernova under study. Additionally, the capability to consider the 3D geometry of the event, allows us to analyse how the mentioned observables are dependent of the observation angle.

The proposed code has been tested to check its functionality with the objective of reproducing, in later sections, the synthetic observables of supernova models. It has been demonstrated that the outcome is in good agreement with current models and observables. Moreover, the code has been also compared with the 1D code from Gomez-Gomar et al. (1998), achieving a successful result. During this initial testing phase, the impact of using slightly different values of mean lifetime decay of the ^{56}Ni chain has been observed. It has been shown that values from different sources in the literature, mostly for ^{56}Co, produce small changes in the outcome flux and can impact both the comparison of codes and the conclusions extracted from the simulated observables.

It must be mentioned that the statistical nature of the simulation, due to the use of Monte Carlo's method, makes the output results subject to statistical noise. This issue leads to a trade-off between noise and performance: statistical noise can be reduced using a bigger pool of gamma-packets, but in turn leads to hugely demanding computational jobs. This trade-off has been tackled by parallelizing the code by considering the bosonic nature of the photons.

Moreover, a 3D code is more computationally demanding than a 1D code mainly due to the need to simulate a bigger size of gamma-packets because the results are aimed to be explored from different directions. Observing from a single direction reduces the quantity of analysed test particles and therefore the resolution of the synthetic observables. However, the 3D code is of great use to explore the early stages up to 70 days after the explosion. It provides a platform to study the asymmetries of the models that cannot be represented in simpler 1D approaches. Nonetheless, the late epoch spectra and light curves of 3D models do not strongly differ from those from 1D models. At this epoch of the model the number of decays have decreased and therefore observables have less resolution. Achieving high resolution at these late epoch would require

increasing the amount of initial gamma-packets but would translate into an enormous computational time for the early stages of the simulation. Therefore, we conclude that 1D codes are good enough for models that just aim to study gamma observables at late epochs.

In Chapter 3 we have applied the code to simulate different scenarios. We inspected the variabilities of the synthetic observables for different amounts of ^{56}Ni in a simple placement of this isotope in the inner core of a sphere model. The placement of ^{56}Ni in the center of the sphere translates in a low gamma-ray flux in the early days that increases meanwhile the ejecta becomes more transparent and the lines of ^{56}Co decay appear in the spectra. These results agree with other studies and observations.

After simulating simple ^{56}Ni cores, we simulated a scenario with multiple ignition points to test the hypothesis of SNe Ia having an off-center ignition and possibly at different spots due to turbulence, buoyancy and drag forces during the burning phase. The outcome showed the appearance of ^{56}Ni lines at early days ($\sim$15th day) but dependent of the observer's line of sight. The light curve of this model displayed a maximum peak of flux that was not observed in the center ignition models. The light curve flux was dependent on the line of sight but its shape was less dependent on it.

The last explosion scenario, we tested the geometry of the model used to explain the early gamma-ray emission of SN 2014J (Isern et al., 2016). The model has a 0.07 $M_\odot$ plume of ^{56}Ni that surrounds the outer layer of the ejecta. It displays lines of ^{56}Ni in the early spectra, in particular we can observe the appearance of line 0.158 MeV. This line was not observed in the early spectra of the multiple ignition points model, in which ^{56}Ni was placed close to the outer layers of the model but not on the surface. Therefore, the observation of this line can tell us if ^{56}Ni is on the surface of the ejecta. This could help differentiate between explosion mechanisms. Moreover, the light curve of the model displayed a peak around day $\sim$9, close to the mean lifetime of the ^{56}Ni decay.

Additionally, we used the same geometry to test a plume composition of ^{48}Cr and a composition of a mix of ^{56}Ni and ^{48}Cr. The goal of these configurations has been to study the signatures that can be observed from the ^{48}Cr synthesised in the explosive burning of the WD's surface. The spectral lines from ^{48}Cr are not displayed in the spectra due to its fast mean lifetime. However, we found out that the decay lines 0.983 MeV and 1.312 MeV from ^{48}V can be differentiated from the rest of spectral lines of the ^{56}Ni decay for some line of sights. The light curves of the models with ^{48}Cr have a faster rising and declining that the models with just ^{56}Ni. Nonetheless, the amounts of ^{48}Cr synthesised in real events is possibly lower than the values used in our models. For future lines of work we suggest more detailed studies that simulate the composition in a more realistic way, adjusting the ^{48}Cr to real values.

Finally, Chapter 4 of this thesis has been devoted to an analysis of the capability of ACS/SPI of detecting a galactic supernova and the tests have been conducted using two different SN Ia models (W7 and DDTe) and the background ACS data

from 275 INTEGRAL revolutions. The two models have been chosen for the completeness of the experiment, providing different luminosity rising times.

Using simulated count rates from the models and the background data from ACS, distances ranging from 4 to 16 kpc have been evaluated along with several galactic longitudes. Results have shown that our proposed method is capable of discovering a galactic SN in the range of 6 to 12 days after the explosion, depending on the model and the distance to the source. Moreover, we show that the discovery date increases with the distance, as the flux of the modelled sources is smaller, following the distance flux relationship. Additionally, the galactic longitude of the source has been shown to have no influence on the discovery date. A logical result considering the large field of view of the ACS/SPI. Given the difference in luminosity between DDTe and W7, the detection of the latter would be half day faster. Using the proposed method, our study has analyzed the available ACS/SPI data of the entire INTEGRAL mission and our results suggest that no SN Ia event has been missed.

The obtained results demonstrate that ACS can also act as a very large field of view detector providing early alerts for other observatories of the presence of an SN Ia event at its early stages. A situation that would provide a very valuable data. Therefore, we suggest that future missions could consider improving the ACS sensitivity to fully exploit its role as an all-sky detector.

Appendix A

Appendix

A.1 ^{48}Cr Decay

Radioactive decay chain: ^{48}Cr $\rightarrow^{48}$V $\rightarrow^{48}$Ti

Half-time:
^{48}Cr: $t_{1/2} = 21.56$ hours
^{48}V: $t_{1/2} = 15.97$ days

Mean life-time or e-folding:
^{48}Cr: $t_{1/2} = 1.296$ days
^{48}V: $t_{1/2} = 23.045$ days

Total decay energy:
^{48}Cr: $E_{Cr} = 0.432$ MeV
^{48}V: $E_V = 2.833$ MeV

Gamma-ray line and probabilities list			
Energy (MeV)	f_l	Energy (MeV)	f_l
0.112	0.96	0.511	0.9980
0.308	1.00	0.944	0.0787
0.511	0.32	0.983	0.9998
		1.312	0.9820
		2.240	0.0233

TABLE A.1: Decay energies and its probabilities for ^{48}Cr (left entries) and ^{48}V (right entries). Source: NNDC, Brookhaven National Laboratory.

A.2 Orthopositronium energy distribution

The energy spectrum of photons emitted in the Orthopositronium phase (creation of three photons) as seen in Ore and Powell, 1949 is :

$$f(E) = 2\left[\frac{E(m_e - E)}{(2m_e - E)^2} - \frac{(2m_e)(m_e - E)^2}{(2m_e - E)^3} \cdot ln\left(\frac{m_e - E}{m_e}\right) + \frac{(2m_e - E)}{E} + \frac{(2m_e)(m_e - E)}{E^2} \cdot ln\left(\frac{m_e - E}{m_e}\right)\right] \quad \text{(A.1)}$$

where m_e is the energy of the electron at rest (0.511 MeV).

The energy spectrum $f(E)$ is shown in Figure A.1.

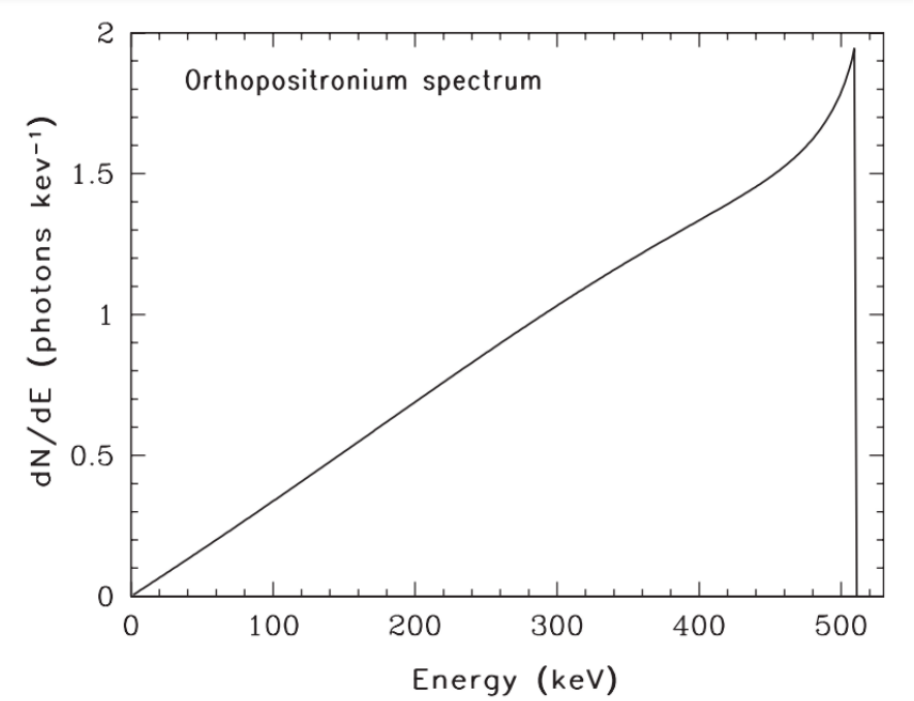

FIGURE A.1: Orthopositronium spectrum as seen in Ore and Powell (1949)

From this expression we use rejection sampling to compute the energy of the orthopositronium photons to follow the correct energy distribution, see Figure A.2.

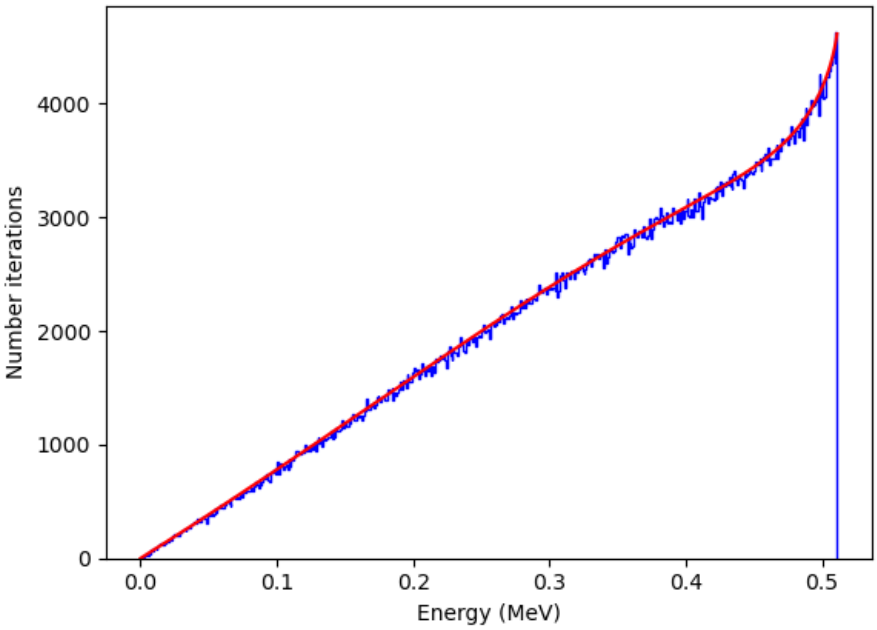

FIGURE A.2: Histogram (in blue) showing the distribution of the energy sampled using rejection method. Orthopositronium energy distribution (in red).

Bibliography

Abbott, D. C. and L. B. Lucy (1985). "Multiline transfer and the dynamics of stellar winds." In: ApJ 288, pp. 679–693. DOI: 10.1086/162834.

Adámek, Karel and Michal Bursa (2014). "Simulating Compton Scattering using Monte Carlo method: COSMOC library". In: *Proceedings of RAGtime 14-16: Workshops on black holes and neutron stars*, pp. 1–10.

Adams, Scott M., C. S. Kochanek, John F. Beacom, Mark R. Vagins, and K. Z. Stanek (2013). "OBSERVING THE NEXT GALACTIC SUPERNOVA". In: *The Astrophysical Journal* 778.2, p. 164. ISSN: 1538-4357. DOI: 10.1088/0004-637x/778/2/164. URL: http://dx.doi.org/10.1088/0004-637X/778/2/164.

Ambwani, Kailash and Peter Sutherland (1988). "Gamma-Ray Spectra and Energy Deposition for Type IA Supernovae". In: ApJ 325, p. 820. DOI: 10.1086/166052.

Arnett, W. D (1969). "A Possible Model of Supernovae: Detonation of ^{12}C". In: Ap&SS 5.2, pp. 180–212. DOI: 10.1007/BF00650291.

Arnett, W. D. (1982). "Type I supernovae. I - Analytic solutions for the early part of the light curve". In: ApJ 253, pp. 785–797. DOI: 10.1086/159681.

Arnett, W. D and R. Chevalier (1996). "Supernovae and Nucleosynthesis: An Investigation of the History of Matter, from the Big Bang to the Present". In: *Physics Today - PHYS TODAY* 49. DOI: 10.1063/1.2807808.

Avery, Lorne W. and Lewis L. House (1968). "An Investigation of Resonance-Line Scattering by the Monte Carlo Technique". In: ApJ 152, p. 493. DOI: 10.1086/149566.

Baade, W. and F. Zwicky (1934). "On Super-Novae". In: *Proceedings of the National Academy of Sciences* 20.5, pp. 254–259. DOI: 10.1073/pnas.20.5.254. eprint: https://www.pnas.org/doi/pdf/10.1073/pnas.20.5.254. URL: https://www.pnas.org/doi/abs/10.1073/pnas.20.5.254.

Barbon, R., F. Ciatti, and L. Rosino (1979). "Photometric properties of type II supernovae." In: A&A 72, pp. 287–292.

Bloom, Joshua S. et al. (2012). "A Compact Degenerate Primary-star Progenitor of SN 2011fe". In: ApJ 744.2, L17, p. L17. DOI: 10.1088/2041-8205/744/2/L17. arXiv: 1111.0966 [astro-ph.HE].

Borkowski, J. et al. (2004). "Giant flare from Sgr 1806-20 detected by INTEGRAL." In: *GRB Coordinates Network* 2920, p. 1.

Branch, David others, Adam Fisher, and Peter Nugent (1993). "On the Relative Frequencies of Spectroscopically Normal and Peculiar Type IA Supernovae". In: AJ 106, p. 2383. DOI: 10.1086/116810.

Branch, D. (1998). "Type IA Supernovae and the Hubble Constant". In: ARA&A 36, pp. 17–56. DOI: 10.1146/annurev.astro.36.1.17. arXiv: astro-ph/9801065 [astro-ph].

Browne, E., R. B. Firestone, and V. S. Shirley (1986). "Table of radioactive isotopes". In: URL: https://www.osti.gov/biblio/6013171.

Burrows, A. and L.-S. The (1990). "X- and gamma-ray signatures of type IA supernovae". In: ApJ 360, pp. 626–638. DOI: 10.1086/169150.

Carter, L. L. and E. Cashwell (1975). *Particle-transport simulation with the Monte Carlo method*. Unknown.

Chugai, N. N. and I. J. Danziger (1994). "SN 1988Z: low-mass ejecta colliding with the clumpy wind?" In: MNRAS 268, pp. 173–180. DOI: 10.1093/mnras/268.1.173.

Churazov, E. et al. (2014). "Cobalt-56 γ-ray emission lines from the type Ia supernova 2014J". In: Nature 512, pp. 406–408. DOI: 10.1038/nature13672. arXiv: 1405.3332 [astro-ph.HE].

Churazov, E. et al. (2015). "Gamma-rays from Type Ia Supernova SN2014J". In: ApJ 812, 62, p. 62. DOI: 10.1088/0004-637X/812/1/62. arXiv: 1502.00255 [astro-ph.HE].

Colgate, Stirling A. and Chester McKee (1969). "Early Supernova Luminosity". In: ApJ 157, p. 623. DOI: 10.1086/150102.

Cowan, G. (1998). *Statistical data analysis*. Oxford University Press, USA.

Diehl, R. et al. (2014). "Early ^{56}Ni decay gamma rays from SN2014J suggest an unusual explosion". In: *Science* 345, pp. 1162–1165. DOI: 10.1126/science.1254738. arXiv: 1407.3061 [astro-ph.HE].

Diehl, Roland et al. (2018). "INTEGRAL/SPI γ-ray line spectroscopy. Response and background characteristics". In: A&A 611, A12, A12. DOI: 10.1051/0004-6361/201731815. arXiv: 1710.10139 [astro-ph.IM].

Filippenko, Alexei V. (1997). "Optical Spectra of Supernovae". In: ARA&A 35, pp. 309–355. DOI: 10.1146/annurev.astro.35.1.309.

Fink, M. others, W. Hillebrandt, and F. K. Röpke (2007). "Double-detonation supernovae of sub-Chandrasekhar mass white dwarfs". In: A&A 476.3, pp. 1133–1143. DOI: 10.1051/0004-6361:20078438. arXiv: 0710.5486 [astro-ph].

Foley, Ryan J. et al. (2013). "Type Iax Supernovae: A New Class of Stellar Explosion". In: ApJ 767.1, 57, p. 57. DOI: 10.1088/0004-637X/767/1/57. arXiv: 1212.2209 [astro-ph.SR].

Fossey, S. J., B. Cooke, G. Pollack, M. Wilde, and T. Wright (2014). "Supernova 2014J in M82 = Psn J09554214+6940260". In: *Central Bureau Electronic Telegrams* 3792, p. 1.

García-Senz, D. and E. Bravo (2005). "Type Ia Supernova models arising from different distributions of igniting points". In: A&A 430, pp. 585–602. DOI: 10.1051/0004-6361:20041628. arXiv: astro-ph/0409480 [astro-ph].

García-Senz, D. and S. E. Woosley (1995). "Type IA Supernovae: The Flame Is Born". In: ApJ 454, p. 895. DOI: 10.1086/176542.

Gehrels, N. others, E. Chipman, and D. A. Kniffen (1993). "The Compton Gamma Ray Observatory." In: A&AS 97, pp. 5–12.

Georgii et al. (2002). "COMPTEL upper limits for the ^{56}Co gamma -ray emission from SN1998bu". In: A&A 394, pp. 517–523. DOI: 10.1051/0004-6361:20021133. arXiv: astro-ph/0208152 [astro-ph].

Gomez-Gomar, Jordi, Jordi Isern, and Pierre Jean (1998). "Prospects for Type Ia supernova explosion mechanism identification with γ-rays". In: *Monthly Notices of the Royal Astronomical Society* 295.1, 1–9. ISSN: 1365-2966. DOI: 10.1046/j.1365-8711.1998.29511115.x. URL: http://dx.doi.org/10.1046/j.1365-8711.1998.29511115.x.

Gros, M. et al. (2004). "INTEGRAL/SPI Observation of the 2003 Oct 28 Solar Flare". In: *5th INTEGRAL Workshop on the INTEGRAL Universe*. Ed. by V. Schoenfelder, G. Lichti, and C. Winkler. Vol. 552. ESA Special Publication, p. 669.

Hajdas, W. et al. (2003). "Radiation environment along the INTEGRAL orbit measured with the IREM monitor". In: A&A 411, pp. L43–L47. DOI: 10.1051/0004-6361:20031251. arXiv: astro-ph/0308269 [astro-ph].

Hamuy, Mario et al. (2003). "An asymptotic-giant-branch star in the progenitor system of a type Ia supernova". In: Nature 424.6949, pp. 651–654. DOI: 10.1038/nature01854. arXiv: astro-ph/0306270 [astro-ph].

Harries, Tim J. (2015). "Radiation-hydrodynamical simulations of massive star formation using Monte Carlo radiative transfer - I. Algorithms and numerical methods". In: MNRAS 448.4, pp. 3156–3166. DOI: 10.1093/mnras/stv158. arXiv: 1501.05754 [astro-ph.SR].

Harries, Tim J., Tom A. Douglas, and Ahmad Ali (2017). "Radiation-hydrodynamical simulations of massive star formation using Monte Carlo radiative transfer – II. The formation of a 25 solar-mass star". In: *Monthly Notices of the Royal Astronomical Society* 471.4, 4111–4120. ISSN: 1365-2966. DOI: 10.1093/mnras/stx1490. URL: http://dx.doi.org/10.1093/mnras/stx1490.

Hillebrandt, W. and Jens C. Niemeyer (2000). "Type Ia Supernova Explosion Models". In: *Annual Review of Astronomy and Astrophysics* 38.1, pp. 191–230. DOI: 10.1146/annurev.astro.38.1.191. eprint: https://doi.org/10.1146/annurev.astro.38.1.191. URL: https://doi.org/10.1146/annurev.astro.38.1.191.

Hillebrandt, W., M. Kromer, F. K. Röpke, and A. J. Ruiter (2013). "Towards an understanding of Type Ia supernovae from a synthesis of theory and observations". In: *Frontiers of Physics* 8.2, pp. 116–143. DOI: 10.1007/s11467-013-0303-2. arXiv: 1302.6420 [astro-ph.CO].

Hoeflich, P., A. Khokhlov, and E. Mueller (1992). "Gamma-ray light curves and spectra for Type IA supernovae". In: A&A 259.2, pp. 549–566.

House, L. L. and L. W. Avery (1968). "The Monte Carlo Technique Applied to Radiative Transfer". In: p. 133.

Hoyle, F. and William A. Fowler (1960). "Nucleosynthesis in Supernovae." In: ApJ 132, p. 565. DOI: 10.1086/146963.

Hungerford, Aimee L., Chris L. Fryer, and Michael S. Warren (2003). "Gamma-Ray Lines from Asymmetric Supernovae". In: ApJ 594.1, pp. 390–403. DOI: 10.1086/376776. arXiv: astro-ph/0301120 [astro-ph].

Iben I., Jr. and A. V. Tutukov (1984). "Supernovae of type I as end products of the evolution of binaries with components of moderate initial mass." In: ApJS 54, pp. 335–372. DOI: 10.1086/190932.

Iben Icko, Jr. and Ronald F. Webbink (1987). "On the formation and properties of close binary white dwarfs". In: *IAU Colloq. 95: Second Conference on Faint Blue Stars*. Ed. by A. G. Davis Philip, D. S. Hayes, and James W. Liebert, pp. 401–412.

Isern, J., E. Bravo, and A. Hirschmann (2008). "Detection and interpretation of γ-ray emission from SNIa". In: *New Astronomy Reviews* 52.7. Astronomy with Radioactivities. VI, pp. 377–380. ISSN: 1387-6473. DOI: https://doi.org/10.1016/j.newar.2008.06.021. URL: https://www.sciencedirect.com/science/article/pii/S1387647308001188.

Isern, J. et al. (2013). "Observation of SN2011fe with INTEGRAL. I. Pre-maximum phase". In: A&A 552, A97, A97. DOI: 10.1051/0004-6361/201220303. arXiv: 1302.3381 [astro-ph.HE].

Isern, J. et al. (2014). "Early gamma–ray emission from SN2014J during the optical maximum as obtained by INTEGRAL". In: *The Astronomer's Telegram* 6099, p. 1.

Isern, J. et al. (2016). "Gamma-ray emission from SN2014J near maximum optical light". English. In: *Astronomy and Astrophysics* 588. ISSN: 0004-6361. DOI: 10.1051/0004-6361/201526941.

Isern, J. et al. (2021). "Synthesis of radioactive elements in novae and supernovae and their use as a diagnostic tool". In: New A Rev. 92, 101606, p. 101606. DOI: 10.1016/j.newar.2020.101606. arXiv: 2101.02738 [astro-ph.HE].

Ivanova, N. et al. (2013). "Common envelope evolution: where we stand and how we can move forward". In: A&A Rev. 21, 59, p. 59. DOI: 10.1007/s00159-013-0059-2. arXiv: 1209.4302 [astro-ph.HE].

Jean et al. (1999). "Possibility of the Detection of Classical Novae with the Shield of the Integral Spectrometer SPI". In: *Astrophysical Letters and Communications* 38, p. 421. arXiv: astro-ph/9903015 [astro-ph].

Kasen, Daniel others, R. C. Thomas, and P. Nugent (2006). "Time-dependent Monte Carlo Radiative Transfer Calculations for Three-dimensional Supernova Spectra, Light Curves, and Polarization". In: ApJ 651.1, pp. 366–380. DOI: 10.1086/506190. arXiv: astro-ph/0606111 [astro-ph].

Kerzendorf, Wolfgang E. and Stuart A. Sim (2014). "A spectral synthesis code for rapid modelling of supernovae". In: MNRAS 440.1, pp. 387–404. DOI: 10.1093/mnras/stu055. arXiv: 1401.5469 [astro-ph.SR].

Khokhlov, A. M. (1991). "Delayed detonation model for type IA supernovae". In: A&A 245.1, pp. 114–128.

Koyama, K. et al. (1995). "Evidence for shock acceleration of high-energy electrons in the supernova remnant SN1006". In: Nature 378.6554, pp. 255–258. DOI: 10.1038/378255a0.

Kromer, M. and S. A. Sim (2009). "Time-dependent three-dimensional spectrum synthesis for Type Ia supernovae". In: MNRAS 398.4, pp. 1809–1826. DOI: 10.1111/j.1365-2966.2009.15256.x. arXiv: 0906.3152 [astro-ph.HE].

Lederer, C. M. and V. S. Shirley (1978). *Table of isotopes. (7th edition)*. John Wiley & amp; Sons, Inc.

Li, T. P. and Y. Q. Ma (1983). "Analysis methods for results in gamma-ray astronomy." In: ApJ 272, pp. 317–324. DOI: 10.1086/161295.

Li, Weidong et al. (2011). "Nearby supernova rates from the Lick Observatory Supernova Search - II. The observed luminosity functions and fractions of supernovae in a complete sample". In: MNRAS 412.3, pp. 1441–1472. DOI: 10.1111/j.1365-2966.2011.18160.x. arXiv: 1006.4612 [astro-ph.SR].

Lichti et al. (1994). "COMPTEL upper limits on gamma-ray line emission from Supernova 1991T." In: A&A 292, p. 569.

Lucy, L. B. (1999a). "Computing radiative equilibria with Monte Carlo techniques". In: A&A 344, pp. 282–288.

– (1999b). "Improved Monte Carlo techniques for the spectral synthesis of supernovae". In: A&A 345, pp. 211–220.

Lucy, L. B. (2002). "Monte Carlo transition probabilities". In: *Astronomy Astrophysics* 384.2, 725–735. ISSN: 1432-0746. DOI: 10.1051/0004-6361:20011756. URL: http://dx.doi.org/10.1051/0004-6361:20011756.

– (2003). "Monte Carlo transition probabilities. II." In: *Astronomy Astrophysics* 403.1, 261–275. ISSN: 1432-0746. DOI: 10.1051/0004-6361:20030357. URL: http://dx.doi.org/10.1051/0004-6361:20030357.

Lucy, L. B. (2005). "Monte Carlo techniques for time-dependent radiative transfer in 3-D supernovae". In: A&A 429, pp. 19–30. DOI: 10.1051/0004-6361:20041656. arXiv: astro-ph/0409249 [astro-ph].

Magee, M. R. et al. (2016). "The type Iax supernova, SN 2015H. A white dwarf deflagration candidate". In: A&A 589, A89, A89. DOI: 10.1051/0004-6361/201528036. arXiv: 1603.04728 [astro-ph.HE].

Maoz, Dan, Filippo Mannucci, and Gijs Nelemans (2014). "Observational Clues to the Progenitors of Type Ia Supernovae". In: ARA&A 52, pp. 107–170. DOI: 10.1146/annurev-astro-082812-141031. arXiv: 1312.0628 [astro-ph.CO].

Marquardt, Kai S. et al. (2015). "Type Ia supernovae from exploding oxygen-neon white dwarfs". In: A&A 580, A118, A118. DOI: 10.1051/0004-6361/201525761. arXiv: 1506.05809 [astro-ph.SR].

Mazzali, Paolo A. others, Friedrich K. Röpke, Stefano Benetti, and Wolfgang Hillebrandt (2007). "A Common Explosion Mechanism for Type Ia Supernovae". In: *Science* 315.5813, p. 825. DOI: 10.1126/science.1136259. arXiv: astro-ph/0702351 [astro-ph].

Mereghetti, S. et al. (2005). "The First Giant Flare from SGR 1806-20: Observations Using the Anticoincidence Shield of the Spectrometer on INTEGRAL". In: ApJ 624.2, pp. L105–L108. DOI: 10.1086/430669. arXiv: astro-ph/0502577 [astro-ph].

Mihalas, D. and B. W. Mihalas (1984). *Foundations of radiation hydrodynamics*.

Milne, P. A. et al. (2004). "Unified One-Dimensional Simulations of Gamma-Ray Line Emission from Type Ia Supernovae". In: ApJ 613.2, pp. 1101–1119. DOI: 10.1086/423235. arXiv: astro-ph/0406173 [astro-ph].

Minkowski, R. (1941). "Spectra of Supernovae". In: PASP 53.314, p. 224. DOI: 10.1086/125315.

Ni, Yuan Qi et al. (2022). "Infant-phase reddening by surface Fe-peak elements in a normal type Ia supernova". In: *Nature Astronomy*. DOI: 10.1038/s41550-022-01603-4. arXiv: 2202.08889 [astro-ph.HE].

Nomoto, K. (1982). "Accreting white dwarf models for type I supernovae. I - Presupernova evolution and triggering mechanisms". In: ApJ 253, pp. 798–810. DOI: 10.1086/159682.

Nomoto, K., F. K. Thielemann, and J. C. Wheeler (1984). "Explosive nucleosynthesis and Type I supernovae". In: ApJ 279, pp. L23–L26. DOI: 10.1086/184247.

Nugent, Peter E. et al. (2011). "Supernova SN 2011fe from an exploding carbon-oxygen white dwarf star". In: Nature 480.7377, pp. 344–347. DOI: 10.1038/nature10644. arXiv: 1110.6201 [astro-ph.CO].

Ore, A. and J. L. Powell (1949). "Three-Photon Annihilation of an Electron-Positron Pair". In: *Phys. Rev.* 75 (11), pp. 1696–1699. DOI: 10.1103/PhysRev.75.1696. URL: https://link.aps.org/doi/10.1103/PhysRev.75.1696.

Panther, Fiona H. et al. (2021). "Prospects of direct detection of ^{48}V gamma-rays from thermonuclear supernovae". In: MNRAS 508.2, pp. 1590–1598. DOI: 10.1093/mnras/stab2701. arXiv: 2103.16840 [astro-ph.HE].

Perets, H. B. et al. (2010). "A faint type of supernova from a white dwarf with a helium-rich companion". In: Nature 465.7296, pp. 322–325. DOI: 10.1038/nature09056. arXiv: 0906.2003 [astro-ph.HE].

Phillips, M. M. (1993). "The Absolute Magnitudes of Type IA Supernovae". In: ApJ 413, p. L105. DOI: 10.1086/186970.

Pozdnyakov, L. A., I. M. Sobol, and R. A. Syunyaev (1983). "Comptonization and the shaping of X-ray source spectra - Monte Carlo calculations". In: Astrophys. Space Phys. Res. 2, pp. 189–331.

Raskin, Cody, F. X. Timmes, Evan Scannapieco, Steven Diehl, and Chris Fryer (2009). "On Type Ia supernovae from the collisions of two white dwarfs". In: MNRAS 399.1, pp. L156–L159. DOI: 10.1111/j.1745-3933.2009.00743.x. arXiv: 0907.3915 [astro-ph.SR].

Rodríguez-Gasén, R. et al. (2014). "Exploring the Capabilities of the Anti-Coincidence Shield of the International Gamma-Ray Astrophysics Laboratory (INTEGRAL) Spectrometer to Study Solar Flares". In: Sol. Phys. 289.5, pp. 1625–1641. DOI: 10.1007/s11207-013-0418-1. arXiv: 1308.3350 [astro-ph.SR].

Röpke, F. K. (2005). "Following multi-dimensional type Ia supernova explosion models to homologous expansion". In: A&A 432.3, pp. 969–983. DOI: 10.1051/0004-6361:20041700. arXiv: astro-ph/0408296 [astro-ph].

Röpke, F. K. and J. C. Niemeyer (2007). "Delayed detonations in full-star models of type Ia supernova explosions". In: A&A 464.2, pp. 683–686. DOI: 10.1051/0004-6361:20066585. arXiv: astro-ph/0703378 [astro-ph].

Röpke, F. K., W. Hillebrandt, J. C. Niemeyer, and S. E. Woosley (2006). "Multi-spot ignition in type Ia supernova models". In: A&A 448.1, pp. 1–14. DOI: 10.1051/0004-6361:20053926. arXiv: astro-ph/0510474 [astro-ph].

Rosswog, S., E. Ramirez-Ruiz, and W. R. Hix (2009). "Tidal Disruption and Ignition of White Dwarfs by Moderately Massive Black Holes". In: ApJ 695.1, pp. 404–419. DOI: 10.1088/0004-637X/695/1/404. arXiv: 0808.2143 [astro-ph].

Savchenko, V., A. Neronov, and T. J. L. Courvoisier (2012). "Timing properties of gamma-ray bursts detected by SPI-ACS detector onboard INTEGRAL".

In: A&A 541, A122, A122. DOI: 10.1051/0004-6361/201218877. arXiv: 1203.1344 [astro-ph.HE].

Savchenko, V. et al. (2017). "INTEGRAL IBIS, SPI, and JEM-X observations of LVT151012". In: A&A 603, A46, A46. DOI: 10.1051/0004-6361/201730572. arXiv: 1704.01633 [astro-ph.HE].

Seitenzahl, Ivo R. et al. (2013). "Three-dimensional delayed-detonation models with nucleosynthesis for Type Ia supernovae". In: MNRAS 429.2, pp. 1156–1172. DOI: 10.1093/mnras/sts402. arXiv: 1211.3015 [astro-ph.SR].

Siegert, Thomas et al. (2018). "Gamma-ray observations of Nova Sgr 2015 No. 2 with INTEGRAL". In: A&A 615, A107, A107. DOI: 10.1051/0004-6361/201732514. arXiv: 1803.06888 [astro-ph.HE].

Sim, S. A. (2005). "Modelling the X-ray spectra of high-velocity outflows from quasars". In: *Monthly Notices of the Royal Astronomical Society* 356.2, 531–544. ISSN: 1365-2966. DOI: 10.1111/j.1365-2966.2004.08471.x. URL: http://dx.doi.org/10.1111/j.1365-2966.2004.08471.x.

– (2007). "Multidimensional simulations of radiative transfer in Type Ia supernovae". In: *Monthly Notices of the Royal Astronomical Society* 375.1, 154–162. ISSN: 1365-2966. DOI: 10.1111/j.1365-2966.2006.11271.x. URL: http://dx.doi.org/10.1111/j.1365-2966.2006.11271.x.

Sim, S. A. and P. A. Mazzali (2008). "On the γ-ray emission of Type Ia supernovae". In: MNRAS 385.4, pp. 1681–1690. DOI: 10.1111/j.1365-2966.2008.12600.x. arXiv: 0710.3313 [astro-ph].

Stritzinger, M., B. Leibundgut, S. Walch, and G. Contardo (2006). "Constraints on the progenitor systems of type Ia supernovae". In: *Astronomy Astrophysics* 450.1, 241–251. ISSN: 1432-0746. DOI: 10.1051/0004-6361:20053652. URL: http://dx.doi.org/10.1051/0004-6361:20053652.

Swartz, Douglas A., Peter G. Sutherland, and Robert P. Harkness (1995). "Gamma-Ray Transfer and Energy Deposition in Supernovae". In: ApJ 446, p. 766. DOI: 10.1086/175834. arXiv: astro-ph/9501005 [astro-ph].

Taubenberger, S. et al. (2008). "The underluminous Type Ia supernova 2005bl and the class of objects similar to SN 1991bg". In: MNRAS 385.1, pp. 75–96. DOI: 10.1111/j.1365-2966.2008.12843.x. arXiv: 0711.4548 [astro-ph].

Taubenberger, Stefan (2017). "The Extremes of Thermonuclear Supernovae". In: ed. by Athem W. Alsabti and Paul Murdin, p. 317. DOI: 10.1007/978-3-319-21846-5_37.

Tomsick, J. and COSI Collaboration (2022). "The Compton Spectrometer and Imager Project for MeV Astronomy". In: *37th International Cosmic Ray Conference. 12-23 July 2021. Berlin*, p. 652. arXiv: 2109.10403 [astro-ph.IM].

Truran, James W., Ami S. Glasner, and Yeunjin Kim (2012). "^{56}Ni, Explosive Nucleosynthesis, and SNe Ia Diversity". In: *Journal of Physics Conference Series*. Vol. 337. Journal of Physics Conference Series, p. 012040. DOI: 10.1088/1742-6596/337/1/012040. arXiv: 1107.1278 [astro-ph.SR].

Turatto, Massimo (2003). "Classification of Supernovae". In: *Supernovae and Gamma-Ray Bursters*. Springer Berlin Heidelberg, pp. 21–36. DOI: 10.1007/3-540-45863-8_3. URL: https://doi.org/10.1007%2F3-540-45863-8_3.

Ubertini, P. et al. (2003). "IBIS: The Imager on-board INTEGRAL". In: A&A 411, pp. L131–L139. DOI: 10.1051/0004-6361:20031224.

Vedrenne, G. et al. (2003a). "SPI: The spectrometer aboard INTEGRAL". In: A&A 411, pp. L63–L70. DOI: 10.1051/0004-6361:20031482.

– (2003b). "SPI: The spectrometer aboard INTEGRAL". In: A&A 411, pp. L63–L70. DOI: 10.1051/0004-6361:20031482.

Veigele, W. J. (1973). "Photon Cross Sections from 0.1 KeV to 1 MeV for Elements Z = 1 to Z = 94". In: *Atomic Data* 5, p. 51. DOI: 10.1016/S0092-640X(73)80015-4.

Vink, Jorick S. et al. (2011). "Wind modelling of very massive stars up to 300 solar masses". In: *Astronomy Astrophysics* 531, A132. ISSN: 1432-0746. DOI: 10.1051/0004-6361/201116614. URL: http://dx.doi.org/10.1051/0004-6361/201116614.

Von Kienlin, A. et al. (2003). "INTEGRAL Spectrometer SPI's GRB detection capabilities. GRBs detected inside SPI's FoV and with the anticoincidence system ACS". In: A&A 411, pp. L299–L305. DOI: 10.1051/0004-6361:20031231. arXiv: astro-ph/0308346 [astro-ph].

Von Kienlin, Andreas, Nikolas Arend, and Giselher G. Lichti (2001). "A GRB Detection System Using the BGO-Shield of the INTEGRAL-Sectrometer SPI". In: *Gamma-ray Bursts in the Afterglow Era*. Ed. by Enrico Costa, Filippo Frontera, and Jens Hjorth, p. 427. DOI: 10.1007/10853853_118. arXiv: astro-ph/0109119 [astro-ph].

Wang, B., S. Justham, and Z. Han (2013). "Producing Type Iax supernovae from a specific class of helium-ignited WD explosions". In: A&A 559, A94, A94. DOI: 10.1051/0004-6361/201322298. arXiv: 1310.2297 [astro-ph.SR].

Webbink, R. F. (1984). "Double white dwarfs as progenitors of R Coronae Borealis stars and type I supernovae." In: ApJ 277, pp. 355–360. DOI: 10.1086/161701.

Whelan, John and Jr. Iben Icko (1973). "Binaries and Supernovae of Type I". In: ApJ 186, pp. 1007–1014. DOI: 10.1086/152565.

Woosley, S. E. others, R. E. Taam, and T. A. Weaver (1986). "Models for Type I Supernova. I. Detonations in White Dwarfs". In: ApJ 301, p. 601. DOI: 10.1086/163926.

Zwicky, F. (1938). "On Collapsed Neutron Stars." In: ApJ 88, pp. 522–525. DOI: 10.1086/144003.